Development of thin films of thermographic phosphors for spatial resolved temperature measurements using sputtering techniques

Jhon Alexander Pareja Restrepo
November 2012

GRUPO DE INVESTIGACIÓN
BIOPROCESOS Y FLUJOS REACTIVOS

Development of thin films of thermographic phosphors for spatial resolved temperature measurements using sputtering techniques

Master-Thesis of Jhon Alexander Pareja Restrepo

1. Advisor: Prof. Alejandro Molina
2. Advisor: Prof. Alejandro Toro

Development of thin films of thermographic phosphors for spatial resolved temperature measurements using sputtering techniques

Jhon Alexander Pareja Restrepo

Thesis presented as a partial requirement to obtain the degree of:
M.Sc. in Chemical Engineering

Advisor:
Alejandro Molina

Co-advisor:
Alejandro Toro

Research group:
Bioprocesos y Flujos reactivos

Universidad Nacional de Colombia - Sede Medellín
Facultad de Minas, Departamento de Procesos y Energía
Medellín, Colombia
2012

Desarrollo de películas delgadas de materiales fosforescentes para mediciones de temperatura superficial utilizando técnicas sputtering

Jhon Alexander Pareja Restrepo

Tesis presentada como requisito parcial para optar al título de:
M.Sc. en Ingeniería Química

Director:
Alejandro Molina

Codirector:
Alejandro Toro

Grupo de Investigación:
Bioprocesos y Flujos reactivos

Universidad Nacional de Colombia - Sede Medellín
Facultad de Minas, Departamento de Procesos y Energía
Medellín, Colombia
2012

A mis padres, Olga y Guillermo, y a mis hermanos, Julián David y Andrés Fernando. Sus enseñanzas, amor, apoyo y sacrificio son los pilares de mi vida.

"*Sì come una giornata bene spesa dà lieto dormire, così una vita bene usata dà lieto morire*".

Leonardo da Vinci

Acknowledgments

I want to thank the following people and institutions that, directly or indirectly, contributed to the accomplishment of this thesis and that somehow were involved in my master's program.

My advisor, Professor Alejandro Molina. It has been an honor working with him. His scientific thoroughness and tireless dedication to his students make him a model to follow. When I was lost, his support and guidance put me always back in the right direction . He always recognized my achievements, but also, never hesitated to invite me to drink a *tinto* (coffee) in the cafeteria every time that I deserved it.

My co-advisor, Professor Alejandro Toro, who with his knowledge and good sense of humor supported me in the materials science topics.

Professor Andreas Dreizler, for giving me the opportunity of staying at the Center of Smart Interfaces of Technische Universität Darmstadt (TU Darmstadt) and for providing me all the necessary resources to carry out this thesis.

Dr. Christian Litterscheid, Matthias Euler and Norman Fuhrmann, for their patience to teach me and their valuable contributions to this work. They were always willing to help me, not only with my research but with my personal issues in Germany.

Professor Barbara Albert, for allowing me using the facilities and resources of her group, at the Eduard-Zintl-Institut für Anorganische und Physikalische Chemie, to prepare the thermographic phosphors and measure the XRD patterns.

PD. Bernhard Kaiser and Jürgen Ziegler, for their assistance during the sputtering experiments.

Universidad Nacional de Colombia, for the complete funding of my master's program, including my stay at TU Darmstadt, through the program "Beca Estudiante Sobresaliente de Posgrado 2011-2012".

Facultad de Minas of Universidad Nacional de Colombia - Sede Medellín and Institut Reaktive Strömungen und Messtechnik of the Center of Smart Interfaces, for the partial funding of my research in Germany.

My colleagues and friends from Universidad Nacional de Colombia - Sede Medellín, almost two years of good times. Particularly, I want to thank Astrid Ramírez and Sebastian López, for their assistance with the time-consuming but necessary paperwork.

My colleagues and new friends from TU Darmstadt, for always trying to facilitate my life in Germany.

Last but not least. My family: my mother, Olga, my father, Guillermo, my brothers, Julius and Andrés; and my friends: Juan Fernando, Oscar, Tobón, Nery, the beautiful Juliana, Laura, Milo, Aleja, Cuevas, Diana Cecilia, Hugo, Andresco, Gaby, Juribo, Ivancho, Mary, Olmos, Astrid, Juanca, Jordant, Henry....Their encouragement, support and presence, even in the distance, make me feel a very lucky person.

Abstract

Two thermographic phosphors materials for surface temperature measurements, praseodymium-doped calcium titanate, $CaTiO_3:Pr^{3+}$, and chromium-doped gadolinium gallium oxide, $Gd_3Ga_5O_{12}:Cr^{3+}$, have been successfully deposited on stainless steel substrates by radio frequency magnetron sputtering. For the sputtering process, phosphor targets were prepared using sol-gel combustion (for $CaTiO_3:Pr^{3+}$) and solid-state reactions (for $Gd_3Ga_5O_{12}:Cr^3$), combined with high temperature sintering. The physical, chemical and luminescence properties of the phosphor films have been evaluated using X-ray diffraction (XRD), X-ray photoelectron spectroscopy (XPS) and laser diagnostics. The results showed that the luminescence features of the thin films were restored by heat treatment after the sputtering deposition. The $CaTiO_3:Pr^{3+}$ film showed low temperature sensitivity of its luminescence lifetime and poor precision of the temperature determination, which could limit its thermographic functionality. Contrary, the $Gd_3Ga_5O_{12}:Cr^{3+}$ film exhibited appropriate temperature sensitivity with adequate precision of the temperature determination, proving to be suitable for thermographic applications. An evaluation of the two-dimensional luminescence characteristics of the $Gd_3Ga_5O_{12}:Cr^{3+}$ thin film revealed spatial inhomogeneities in the luminescence lifetime of the film. A study on $Gd_3Ga_5O_{12}:Cr^{3+}$ powders samples, varying the doping concentration and co-doping with cerium, was included with the aim of increasing the understanding about the luminescence characteristics of this phosphor. These results showed that increasing the Cr doping concentration only changes significantly the luminescence lifetime for concentrations above 1 mol%, while temperature sensitivity and precision of the temperature determination are maintained. Co-doping with small amounts of cerium reduces the afterglow of the $Gd_3Ga_5O_{12}:Cr^{3+}$ phosphor. However, an excess of cerium could significantly affect the luminescence properties, resulting in poor precision of the temperature determination.

Resumen

Se evaluó el desempeño de la pulverización catódica (*sputtering*) para producir recubrimientos de materiales fosforescentes para la medición de temperaturas superficiales. Se depositaron exitosamente películas delgadas de titanato de calcio dopado con praseodímio, $CaTiO_3:Pr^{3+}$, y granate de gadolinio y galio dopado con cromo, $Gd_3Ga_5O_{12}:Cr^{3+}$, en sustratos de acero inoxidable, utilizando sputtering por radiofrecuencia combinada con campo magnético. Los objetivos para el proceso de sputtering se prepararon mediante las técnicas sol-gel con combustión (para el $CaTiO_3:Pr^{3+}$) y reacciones de estado sólido (para el $Gd_3Ga_5O_{12}:Cr^{3}$) combinadas con sinterización a alta temperatura. Se evaluaron las propiedades físicas, químicas y de luminiscencia de las películas delgadas, mediante difracción de rayos X (DRX), espectroscopia de fotoelectrones emitidos por rayos X (XPS) y diagnóstico láser. Los resultados mostraron que las propiedades de luminiscencia de las películas fueron restablecidas con tratamiento térmico después de la deposición por sputtering. La película de $CaTiO_3:Pr^{3+}$ mostró una baja sensibilidad de la duración de la luminiscencia con el cambio de temperatura y una baja precisión en la determinación de la temperatura, lo cual podría limitar su funcionalidad para fines de termometría. Por el contrario, la película de $Gd_3Ga_5O_{12}:Cr^{3+}$ mostró una sensibilidad apropiada de la duración de la luminiscencia con el cambio de temperatura con una alta precisión en la determinación de la temperatura, probando que esta película delgada es adecuada para aplicaciones de termometría de superficies. Una evaluación de las características de luminiscencia en dos dimensiones de la película de $Gd_3Ga_5O_{12}:Cr^{3+}$ reveló una homogeneidad relativamente baja en la duración de la luminiscencia de la película. Se estudió para muestras en polvo de $Gd_3Ga_5O_{12}:Cr^{3+}$, el efecto de la concentración del cromo y el codopado con cerio, con el fin de incrementar el entendimiento de las propiedades de luminiscencia de este material fosforescente. Estos resultados mostraron que el incremento en la concentración de cromo sólo influye significativamente en la duración de la luminiscencia para concentraciones mayores a 1 % molar, mientras se mantienen la sensibilidad de la duración de la luminiscencia con el cambio de temperatura y la alta precisión en la determinación de la temperatura. Codopar con pequeñas cantidades de cerio causa una reducción del resplandor posterior a la luminiscencia. Sin embargo, un exceso de cerio puede afectar significativamente las propiedades de luminiscencia del $Gd_3Ga_5O_{12}:Cr^{3+}$, con una disminución de la precisión en la determinación de la temperatura.

Contents

List of Figures

List of Tables

1 Introduction

Temperature is one of the most important properties for the design and optimization of combustion systems such as internal combustion and turbine engines. To improve their efficiency, engines need to be operated at high temperatures. Operating engines at high temperatures affects the thermal load on the components, shortening their lifetime and leading to their failure [1, 2]. Therefore, spatial- and temporal-resolved accurate information about surface temperatures is essential for the design of appropriate cooling schemes, the improvement of predictive design codes, and the development of new materials capable of operating in more demanding scenarios (i.e. higher gas temperatures and longer life cycles).

Existing techniques for the measurement of surface temperatures include thermocouples, thermochromic liquid crystals, temperature-sensitive paints, heat-sensitive paints, non-invasive pyrometry, and thermographic phosphors [3]. Thermocouples are cheap and require little effort. They are usually employed to measure temperature in one spot with a limited temporal resolution. However, two-dimensional temperature measurements would require embedding several thermocouples on the surface, resulting in a difficult and expensive installation, specially in moving components. This inherently intrusive characteristic affects also the thermal state of the surface under test. Additionally, they are sensitive to electromagnetic radiation [4].

Thermochromic liquid crystals are highly anisotropic fluids that exist between the boundaries of the solid phase and the conventional, isotropic liquid phase. They reflect definite colors at specific temperatures and viewing angle. However, TLCs are limited to measure temperatures from 240 K up to 380 K, with relative poor temporal resolution ($\sim$10 ms) [5]. Temperature-sensitive paints are coatings of luminescent molecules and an oxygen impermeable binder. The surface temperature is determined by the thermal quenching that reduces the luminescent intensity as temperature increases. Although the technique can provide two-dimensional temperature information, it is limited to temperatures < 350 K [6].

Heat-sensitive paints are an expensive and intrusive technique. They indicate temperatures associated with color changes remotely. However, excessive calibration times are required and only discrete peak values of the temperature with poor resolution are provided. Pyrometry is a non-intrusive, line of sight technique based on the blackbody radiation emitted by the surface of interest. Two-dimensional temperature maps with very high temporal and spatial resolution can be determined with this technique. Nevertheless, it is sensitive to stray light, chemiluminescence, and blackbody radiation of other sources. Moreover, it is limited by changes in the emissivity of the surface with temperature which causes in some cases poor accuracy [3].

In contrast, thermographic phosphors (TP) are usually ceramic materials doped with rare earths or transition metals that exhibit temperature-dependent luminescence characteristics. They offer a semi-intrusive, accurate, temporally and spatially highly resolving technique for remote measurement of surface temperatures over a broad temperature range from cryogenic temperatures up to 1970 K [7]. This technique is insensitive to the properties of the surface and robust against interferences from scattered light, chemiluminescence or soot radiation. With an appropriate handling, its accuracy is better than 1% [8, 9]. TP has been used to determine temperature in a variety of combustion applications such as impinging jet flames [10], gas turbine combustors [11], thermal decomposition of solid materials [12], internal combustion engines [13], fuel droplets and sprays [14] and 2D thermal imaging [15, 16].

The use of thermographic phosphors requires bonding to the surface of interest (substrate). The synthesis of the phosphors may be performed during the bonding process or separately. The latter case is the most employed method for thermography purposes. Thermographic phosphor powders shythesized separately are first mixed with binders, such as polymer binders [4, 17], silicon resins [18, 19] or other commercially available agents [20, 21], and then the mixture is applied to the substrate using air-brushing or -spraying. The method usually produces homogeneous coatings with thicknesses from 10 to 60 μm and with reproducible temporal and spectral luminescence properties. Additionally, this method has the advantages of being very simple and nearly all available phosphors may be bonded by this technique. However, the resistances of these binders to high temperatures, chemical aggressive environments, and mechanical stress are usually limited which limits the application of the thermographic phosphors for temperature measurements in real engines. Previous studies using thermographic phosphors in gas turbines report fast degradation of chemically-bonded coatings during fired operation of the engine [11, 22, 23, 24]. However, temperature measurements under controlled experimental conditions have been also successfully conducted in fixed and moving parts of gas turbines [25, 26] and internal combustion engines [16, 27].

Several thin film deposition techniques such as the sol-gel method, Chemical Vapor Deposition (CVD), and Physical Vapor Deposition (PDV) are available for the production of uniform, homogeneous, well-adhered, high-purity coatings [28]. However, few studies report using those techniques as alternatives to bond thermographic phosphors [29]. The sol-gel method is a wet-chemical procedure for the direct preparation of a coating on the substrate. A colloidal route is used to synthesize ceramics with an intermediate stage that includes a sol and a gel state [30]. Thermographic phosphors such as TiO_2:Eu^{3+} [31] and Al_2O_3:Cr^{3+} [32] have been bonded using the sol-gel method.

Chemical Vapor Deposition, CVD, has been employed for the deposition of several materials, including metals, semiconductors, oxides and alloys. Initially, the precursors are transferred to the vapor phase by evaporation or sublimation, then they are transported by a transport gas flow to the reaction chamber where they are adsorbed on the substrate surface. After being activated energetically, they react in a heterogeneous chemical reaction to form a thin solid film [28]. CVD has been reported to deposit films of Al_2O_3:Cr^{3+} [33], Al_2O_3:Dy^{3+} [34] and Y_2O_3:Eu [35] in thermography applications.

In the case of Physical Vapor Deposition, PVD, the components of the film are initially prepared in solid sources or targets. Then, the components are transferred to the vapor phase inside a vacuum chamber by physical processes such as electron beam evaporation (EB-PVD), sputtering, pulsed laser, or plasma spray. Finally the atoms are recondensed on the substrate to form the film [28]. For thermography purposes, phosphors such as YSZ:Eu [36], YSZ:Dy [37], YAG:Tm [37], and Al_2O_3:Cr^{3+}[38] have been successfully bonded with EB-PVD while films of YSZ:Eu have been deposited with plasma [39] .

Several factors have to be considered to guarantee the accuracy and robustness of the thermographic phosphors technique. First, the intensity of the emitted luminescence signal should be high enough to distinguish it from the background noise and any other kind of radiation. Second, the thickness of the phosphor coating applied on the surface should be minimized to reduce the error induced by the thermal gradient between the surface of the substrate surface and the top layer of the phosphor coating [24]. Third, the adhesion of the coating to the surface should give good durability characteristics to the coating. Particular care has to be given to the measurement and calibration strategies with the aim of reducing the error [29].

Among the PVD techniques, sputtering could be an alternative to overcome the challenges related to the coating preparation. Sputtering is the ejection of surface atoms form a target material by ion bombarding (plasma) with the subsequent condensation of those atoms on another surface (substrate). This is a very versatile process that allows depositing a large variety of materials with high purity, homogeneity and adhesion and with film thicknesses from the nano to the micro scale [40]. Sputtering has been widely used

for the preparation of thin films of phosphors such as Y_2GeO_5:Mn [41], $ZnGa_2O_4$:Mn [42, 43], ZnO:Er [44], La_2O_3:Bi [45], $MgWO_2$ [46], Ga_2O_3:Mn [47], ZnS:Cu [48] and $SrGa_2S_4$:Eu [49] for electroluminescence applications. However, in the referred literature only sputtered films of Y_2O_3:Eu^{3+} [24, 50] and YVO_4:Eu [23] have been evaluated for thermographic purposes.

The aim of the present work is to evaluate sputtering deposition as a bonding technique of thermographic phosphors. For this purpose, two thermographic phosphors have been selected, namely, praseodymium-doped calcium titanate, $CaTiO_3$:Pr^{3+}, and chromium-doped gadolinium gallium oxide, $Gd_3Ga_5O_{12}$:Cr^{3+} (also known as GGG:Cr^{3+}). $CaTiO_3$:Pr^{3+} is a phosphor with low lifetimes at low temperatures (from 300 to 620K). $CaTiO_3$:Pr^{3+} was selected mainly due to its simple structure. The use of sputtering deposition of $CaTiO_3$:Pr^{3+} for the thermographic approach has not been reported. Sputtered films of this phosphor have been only employed in electroluminescence applications [51, 52, 53] since $CaTiO_3$:Pr^{3+} has an emission very closed to the "ideal" red color [54]. On the other hand, GGG:Cr^{3+} is a thermographic phosphor with appropriate low lifetime characteristics and insensitivity of its luminescence to the surrounding gas phase in a relative wide range of temperatures (from 300 to 1000K) that makes it ideal for temperature measurements in combustion systems such as internal combustion engines [9]. To the best of the author's knowledge, there is not report about the use of sputtering to deposit specifically this phosphor. Previous studies of laser deposition of GGG:Cr^{4+} [55] and GGG:Nd [56] for laser applications and EB-PVD of GGG:Ag [57, 58] for electroluminescence applications are the state of the art.

The present study is organized as follows: relevant theoretical background regarding luminescence phenomena, thermographic phosphors and sputtering is reviewed in Chapter 2. Chapter 3 summarizes the main and specific objectives of the present work. Chapter 4 details the methodology followed to achieve the objectives, including the preparation of the phosphor targets, the deposition of the thin films using sputtering, the characterization of the phosphor films, and the evaluation of the luminescence properties at different temperatures. The results and analysis of the evaluation of sputtering as a coating technique of thermographic phosphors, for potential thermography applications with high spatial and temporal resolutions, are presented in Chapter 5. Additional experiments on GGG:Cr powder samples were carried out due to the potential of this phosphor for thermography applications. These results are also included and discussed in this study.

2 Fundamentals and Background

This chapter summarizes some relevant theoretical aspects of luminescence in and its application for surface temperature measurements. General descriptions of the crystal structures and luminescence properties of praseodymium-doped calcium titanate, $CaTiO_3$:Pr^{3+}, and chromium-doped gadolinium gallium oxide, $Gd_3Ga_5O_{12}$:Cr^{3+}, are also included. Finally, the background and general aspects of sputtering, as a deposition technique of thin films, are reviewed.

2.1 Luminescence and thermographic phosphors

2.1.1 Principles of luminescence

In general, luminescence processes involve the excitation of luminescent molecules, to jump to higher electronic states, followed by different de-excitation phenomena. Vibration relaxation, internal conversion, intersystem crossing and emissions are example of de-excitation phenomena that return the excited state back to the ground or to an intermediate state [7]. Figure 2.1 depicts a simplified energy level diagram showing the main luminescence processes. Excitation involves the absorption of sufficient energy to raise a molecule's electron form the ground state S_0 into the electronic state S_1, which generally occurs in order of femtoseconds. The molecule does not remain excited continually as the amount of energy absorbed must be released according to the principle of energy conservation. DIfferent de-excitation processes are of relevance in luminescence [7]:

- Fluorescence: a radiative transition from the excited state accomplished by the emission of a photon. The emission wavelength is found to be less than the excitation wavelength due to energy level differences, resulting in emissions of longer wavelengths. Fluorescence typically occurs in a timescale of less than 10^{-8} s.
- Intersystem crossing: a transition from the excited state S_1 to the intermediate state T_1. Intersystem transitions require changes in electron spin and generally have an extremely low probability of occurrence. However, molecules containing heavy atoms (e.g. transition metals) often facilitate intersystem crossing, making these as common as internal conversions, in times from 10^{-10} to 10^{-8} s.
- Phosphorescence: if after an intersystem transition the molecule has not returned to its ground state, phosphorescence is the transition from T_1 to S_0. The energy level of T_1 is lower than that of S_1 and therefore the emission wavelength of phosphorescence is higher than that of fluorescence. Additionally, this process is orders of magnitude slower than fluorescence ($> 10^{-8}$ s).

2.1.2 Thermographic phosphors

Phosphors are materials that non-thermally convert energy into electromagnetic radiation. They are usually defined as rare-earth or transition-metal-doped ceramic materials that emit visible light after excitation by short-wavelength light, X-ray radiation or electron bombardment [29]. Phosphors consist of two components: a host compound and an activator or doping agent from which the light is emitted. In

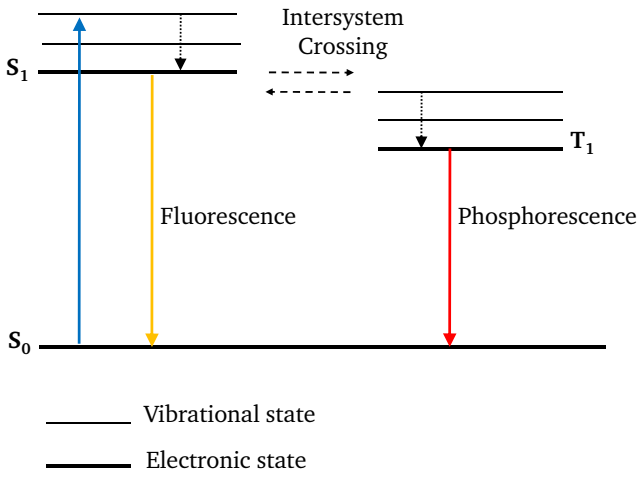

Figure 2.1: Simplified energy level diagram of the main luminescence processes.

the case of praseodymium-doped calcium titanate, $CaTiO_3$:Pr^{3+} and chromium-doped gadolinium gallium oxide, $Gd_3Ga_5O_{12}$:Cr^{3+}, $CaTiO_3$ and $Gd_3Ga_5O_{12}$ are termed as host, the Pr^{3+} and Cr^{3+} ions as activators or doping agents.

The excitation energy can be absorbed by the activator, by the host crystal or by another dopant (co-dopant). For the subsequent return from the excited state to the ground state, basically radiative transfer processes compete with non-radiative processes. Whereas the spontaneous emission of at least one photon is involved in the first case, non-radiative processes only rely on internal energy transfer. Thermographic phosphors are those whose rates of the non-radiative processes are a function of temperature due to internal energy transfer processes that are enhanced by the temperature [29].

Because the doping agents are in a not-static host, temperature might have a significant effect on the luminescence behavior of the phosphor. As represented in the configurational coordinate diagram in Figure 2.2, after excitation, electrons occupying an upper vibrational level of an excited state (point B) relax to the ground vibrational level of that state (C) losing energy by releasing phonons. Following radiative emission, the electrons reaching a higher vibrational level of the ground state (D) further lose energy (phonons) on their return to their ground state equilibrium (A) [7]. If the temperature is high enough, electrons in the excited state can intersect the ground state curve (point E) allowing vibrational relaxation via phonon release to the ground state without any radiative emission. This can be described as the absorption of thermal energy (phonon) from point C, which excites the electrons to the intersection point E. Because non-radiative processes can now also take place, the observed luminescence intensity from a large quantity of excited ions decreases, explaining the thermal quenching behavior that changes the luminescence properties of thermographic phosphors [7].

In some host materials, the outer crystal field, could cause another energy potential (known as charge transfer state) that can be added on to the existing configuration coordinate diagram (Figure 2.3). Excited electrons can now return to the ground state via the charge transfer (CT) curve. If an excited electron reaches an excited state of E3, it would normally return to the ground state by radiative emission. However, if the electrons are further excited by elevated temperatures, the electrons can intersect the crossover point of the CT curve, enabling the transfer of electrons to a lower energy level of E2 without any radiative emission. Likewise, electrons in the E2 or E1 states can transfer their energy to the ground state in the same way [7]. Different hosts will have the CT curve in slightly different places, thus explaining the different behavior of a doping agent in different hosts [54].

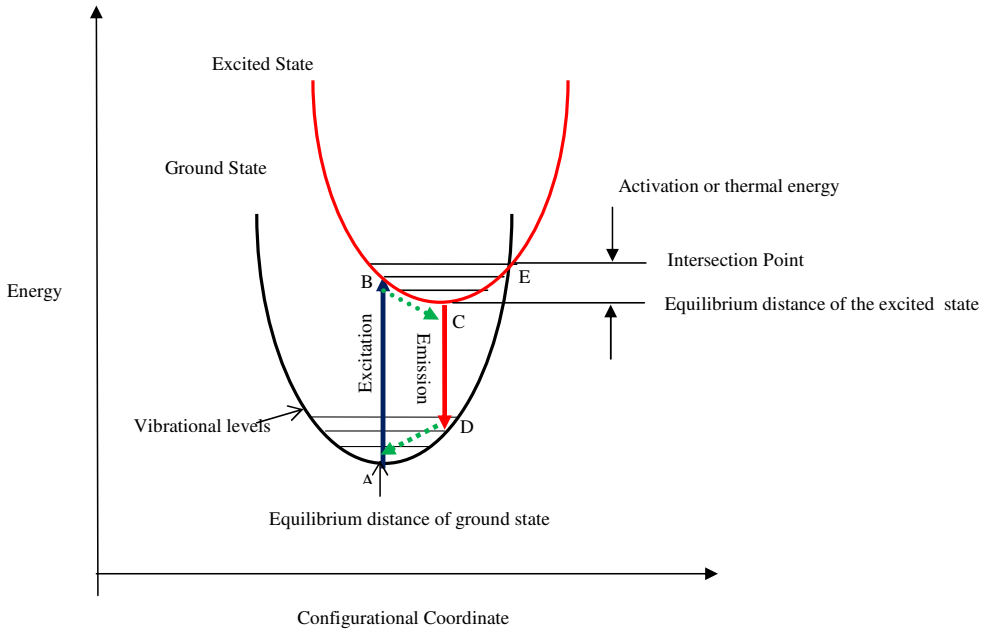

Figure 2.2: Configurational coordinate diagram [7].

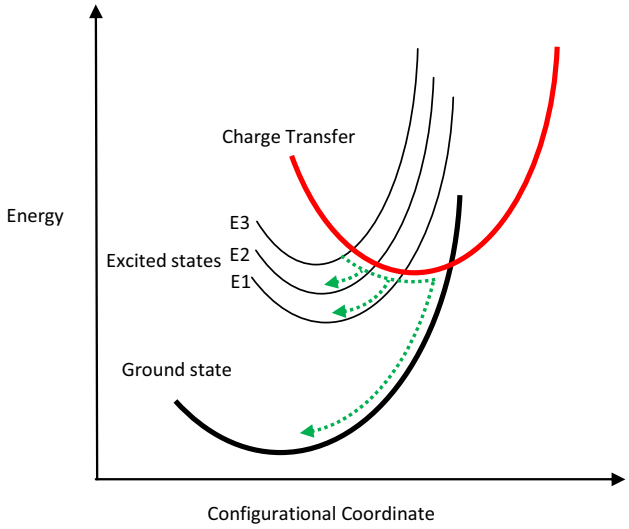

Figure 2.3: Configurational coordinate diagram with charge transfer state [7].

As Brübach *et al.* [29] pointed out, in thermographic phosphors the distinction between the phenomenon of fast spin-allowed (fluorescence) and slow spin-forbidden transitions (phosphorescence) is not well-defined, in this study the terminology is restricted to the general term, luminescence.

2.1.3 Praseodymium-doped Calcium Titanate, $CaTiO_3:Pr^{3+}$

In the thermographic phosphor praseodymium-doped calcium titanate, $CaTiO_3:Pr^{3+}$, the perovskite $CaTiO_3$ acts as host material and the Pr^{3+} ion as doping agent. In Figure 2.4, at room temperature, the structure of $CaTiO_3$ is orthorhombic and is made up of corner-shared TiO_6 octahedra with Ca ions in the large cavities at the corners of the unit cell [59]. The Pr^{3+} ion has the [Xe] $4f^2$ configuration. The energy level scheme of Pr^{3+} up to about 25000cm^{-1}, in Figure 2.5 (a), consists of a large number of energy levels. Upon excitation with UV or visible light, the emission spectrum can either be dominated

by emission from the $^3P_0$ level (greenish-blue emission) or from the $^1D_2$ level (red emission).

In $CaTiO_3$:Pr^{3+}, the Pr^{3+} ions are expected to occupy the C_{1h} calcium sites of the $CaTiO_3$. Upon UV excitation, this phosphor shows only emission from the $^1D_2$ level, which is located in the red spectral region [59]. This attribution suggests the total quenching of the luminescence transition $^3P_0 \rightarrow {}^3H_4$ transition. Various non-radiative de-excitation pathways could explain the quenching of $^3P_0$ luminescence in $CaTiO_3$: (1) multi-phonon relaxation, (2) cross-relaxation within pairs of Pr^{3+} ions and (3) intersystem crossing through either low-lying $4f^15d^1$ levels or through Pr- to-metal charge transfer state (CTS) [60].

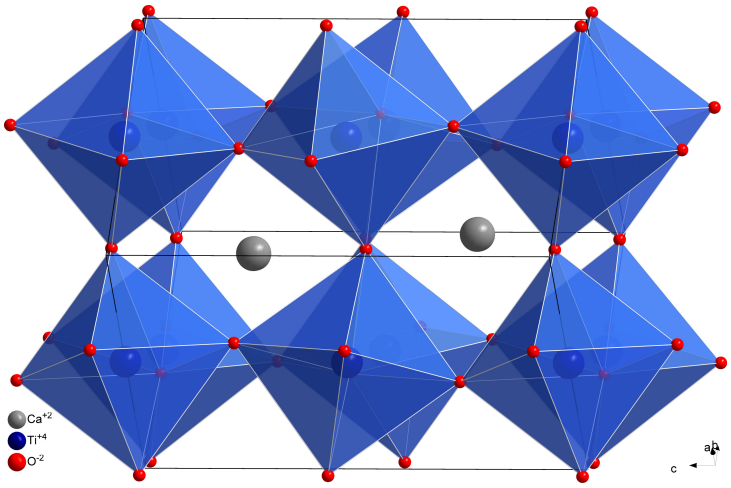

Figure 2.4: Perovskite structure of $CaTiO_3$.

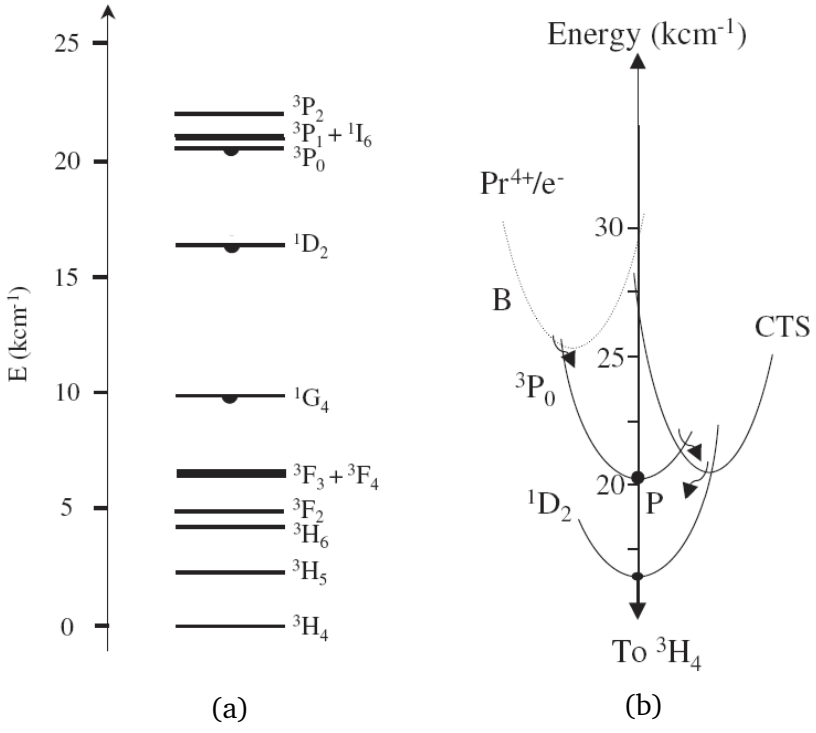

Figure 2.5: (a) Energy level scheme of the Pr^{3+} ion up to about 25000cm^{-1}, (b) Coordinate energy diagram for Pr^{3+} in $CaTiO_3$ [60].

Boutinaud *et al.* [60] recently proposed that the presence of two very short Pr^{3+} - Ti^{4+} interatomic distances of 3.17 Å in $CaTiO_3:Pr^{3+}$ makes possible a photon assisted energy transfer from Pr^{3+} to Ti^{4+} at relatively low energy. This energy transfer, referred to as Pr^{3+} / Ti^{4+} $\rightleftharpoons$ Pr^{4+} / Ti^{3+} charge transfer state (CTS), interferes strongly with the excited dynamics of the Pr^{3+} in $CaTiO_3:Pr^{3+}$, causing the quenching of the otherwise prominent greenish-blue emission from the $^3P_0$ level, as represented in Figure 2.5 (b).

2.1.4 Chromium-doped Gadolinium Gallium Oxide, $Gd_3Ga_5O_{12}:Cr^{3+}$

Chromium-doped gadolinium gallium oxide is a thermographic phosphor in which $Gd_3Ga_5O_{12}$ serves as host material for the luminescent transition-metal ions of Cr^{3+}. $Gd_3Ga_5O_{12}$ belongs to the cubic crystalline system, has a garnet structure, with $Ia3d$ space group and a bulk cell parameter (a_0) of 12.376 Å. This is why $Gd_3Ga_5O_{12}$ is sometimes referred as GGG. The garnet structure is composed of a 24(c) dodecahedral site (D_2 point symmetry) for Gd^{3+} with coordination number 8 and two sites for Ga^{3+}, a 16(a) octahedral site with a coordination number 6, and a 24(d) tetrahedral site of coordination number 4. O^{2-} ions occupy the 96(h) sites with each one being a member of two dodecahedra, one octahedron and one tetrahedron [61]. The garnet structure can be viewed as interconnected dodecahedra, octahedra and tetrahedra with shared O atoms at the corners of the polyhedra, as in Figure 2.6.

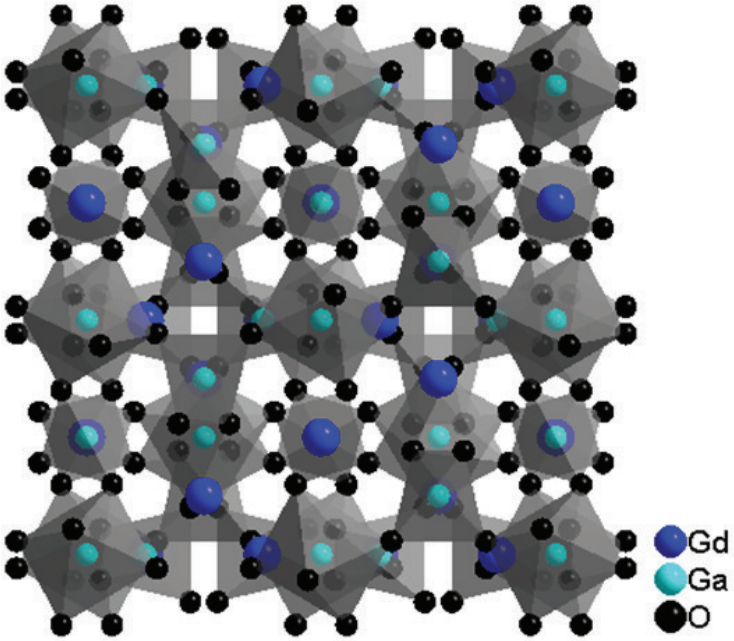

Figure 2.6: Structure of the $Gd_3Ga_5O_{12}$ garnet [61].

The Cr^{3+} ions are expected to enter into the Ga^{3+} sites of the GGG. Depending on the crystal-field strength, the lowest Cr^{3+} emitting level can be the $^4T_2$ or the ^2E states. Each excited state exhibits different luminescence properties due to the different electron-lattice coupling. As depicted in Figure 2.7, at room temperature and atmospheric pressure, the Cr^{3+} in GGG emission is dominated by the spin-allowed $^4T_2 \rightarrow {}^4A_2$ transition which results in a fast decay and a broad emission band. However, the narrow R-lines emission associated with the spin-forbidden transition from the ^2E level to the $^4A_2$ ground state is expected to be also present [62].

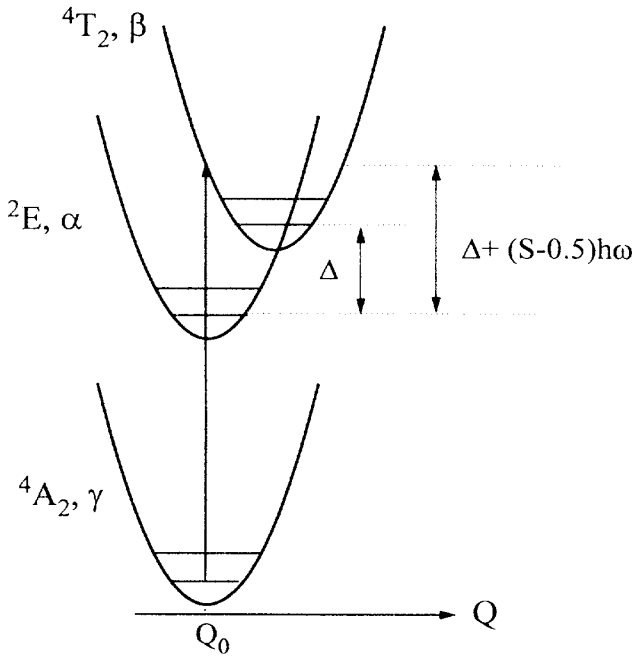

Figure 2.7: Coordinate energy diagram for Cr^{3+} in $Gd_3Ga_5O_{12}$ [62].

2.2 Temperature measurement with thermographic phosphors

2.2.1 Typical phosphor thermometry system

A typical phosphor thermometry system is illustrated in Figure 2.8. In general, an excitation source, usually a laser, is used to excite the phosphor that is bonded onto the surface of interest. The subsequent emission is passed through an optical filter to remove unwanted emissions at different wavelengths. The light is collected and converted into a signal using a detector. The stored data is analysed and compared with calibration data to determine temperature.

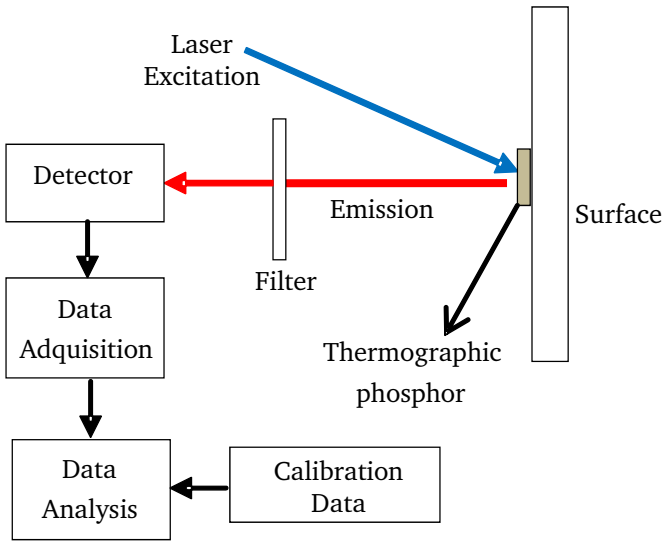

Figure 2.8: Schematic of a typical phosphor thermometry system.

Thermographic phosphors offer surface thermometry with high spatial and temporal resolution over a broad temperature range, up to 1970 K. The method is rather insensitive to the properties of the surface and robust against interferences from scattered light, chemiluminescence or soot radiation. Provided careful handling, its accuracy is better than 1% [29]. Among the disadvantages of the phosphor thermometry systems are: decreasing signals with increasing temperatures, bonding of the phosphor, phosphor coating can be semi-intrusive or intrusive depending on thermal properties and thickness [7].

2.2.2 Temperature measurement strategies

Due to the complex phenomena involved in luminescence, appropriate calibration of the emission signal at well-known temperatures is required to relate luminescence properties and temperature. Figure 2.9 summarized the classification of the temperature measurement strategies proposed by Brübach *et al.* [29]. The strategies can be classified according to the different response signals of the luminescence characteristics. The time-resolved luminescence characteristics become evident in the time-domain, i.e. in the decay of the luminescence after a pulsed excitation as well as in the frequency-domain, i.e. in the phase shift of the luminescence in reference to an amplitude modulated excitation.

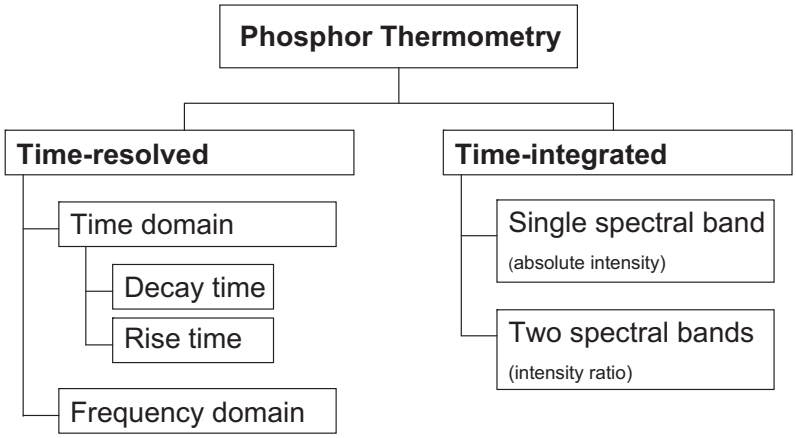

Figure 2.9: Classification of temperature measurement strategies [29].

In the time domain, the transient luminescence intensity following a pulsed excitation can be approximated by a mono-exponential decay characteristic. This decay process is faster at higher temperatures due to higher rates of non-radiative transitions. For this approach the temporal signal characteristic is reduced to the scalar value of the lifetime,τ, as a measure for temperature. For the less common rise-time approach, it is exploited that there are different potential energy transfers and paths that occur at different timescales changing the rise time characteristics with temperature because of the properties of the crystal structure of the phosphor [7]. In the frequency domain, a continuous excitation wave is used instead of a pulsed one. The resulting wave will have a different amplitude and phase due to various time lags of certain luminescent processes. Consequently, the temperature sensitivity of this phase shift is exploited for thermometry.

The time-integrated luminescence intensity of thermographic phosphors also depends on the temperature. However, the determination of the absolute luminescence intensity is critical, as this depends on hardly reproducible boundary conditions like the excitation energy, the homogeneity of the phosphor layer, the quality and stability of the alignment, impurities on the optics or other disturbing factors related to the excitation source, the phosphor and the detector [29]. The use of the one spectral band approach demands an in-situ calibration, which is not feasible in many applications. Some drawbacks

are compensated by the normalization of one spectral band's time-integrated luminescence intensity to another one. Therefore, the method of the temperature-dependent intensity ratio reduces the signal intensity of two spectral bands to a scalar value by a simple quotient.

2.3 Sputtering

2.3.1 Interactions of ions with surfaces

Figure 2.10 represents the phenomena that may occur when an ion approaches the surface of a solid (also know as target): (1) The ion may be reflected, probably being neutralized in the process; (2) the impact of the ion may cause the surface to eject an electron, usually referred to as a secondary electron; (3) the ion may become implanted; (4) the ion impact may also be responsible for some structural changes such as vacancies, interstitials, and changes of stoichiometry or charge level; (5) the ion impact may set up a series of collisions between atoms of the target, possibly leading to the ejection of one of these atoms [63]. This last interaction is know as sputtering.

In the sputtering process the bombarding ions strike the atomic array of the target, scattering the target atoms in all directions, including some out of the target surface. Ions are usually used to bombard the target because they can be easily accelerated by an electric field. After the ion impact, the collision phenomena in the target could result in the sputter ejection of an atom from the surface or gradual dissipation of the impact energy to lattice vibrations (i.e. heat). The sputter ejection is inefficient, with typically 1% of the incident energy reappearing as the energy of the sputtered atoms [63].

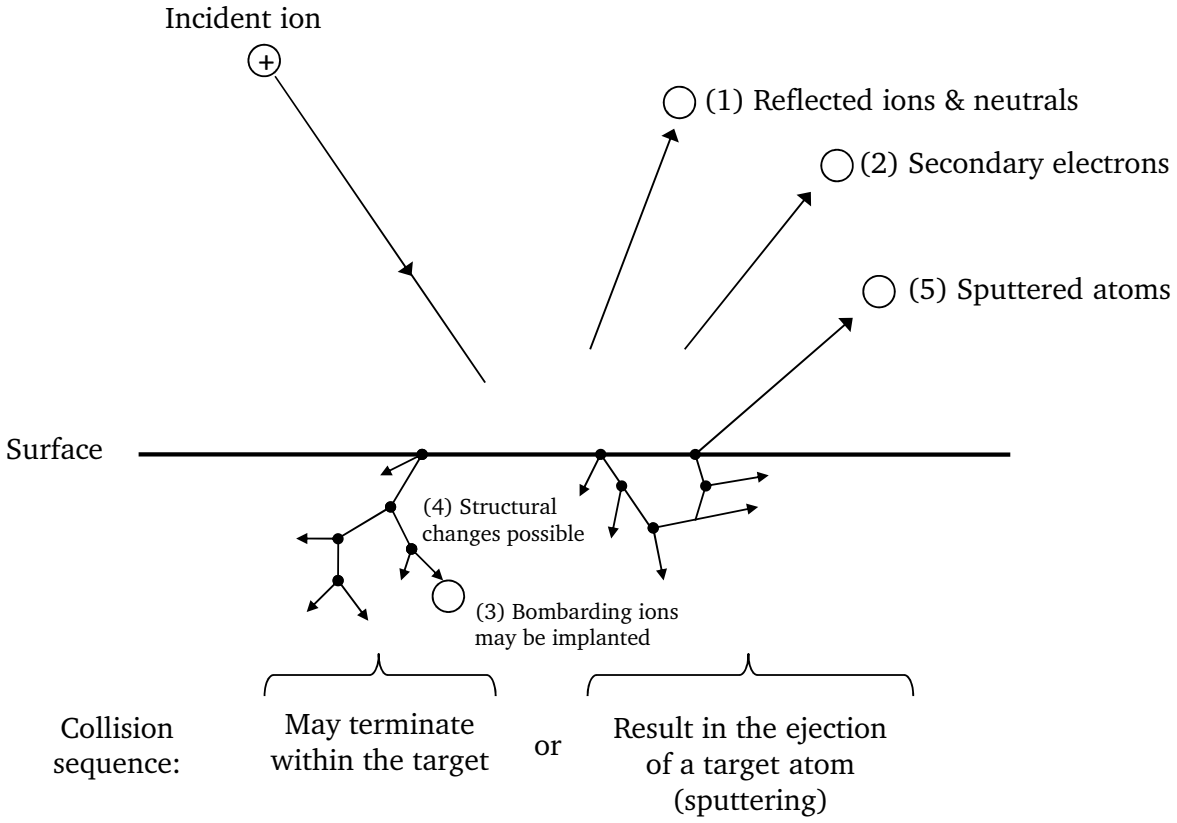

Figure 2.10: Possible interactions of ions with surfaces (adapted from [63]).

2.3.2 Sputtering deposition

One of the applications of sputtering is the deposition of coatings on a surface. An ejected atom can, under certain circumstances, move through certain distance until it strikes and condenses on the surface of a receiver, which is known as a substrate. By repeating the process over and over, a coating of several atomic or molecular layers of target material builds up on the substrate. The coating, between 100 nm and 3 μm, is called thin film. Sputtering deposition is a very versatile process that allows depositing a large variety of materials, producing films with high purity, homogeneity and adhesion [40, 63].

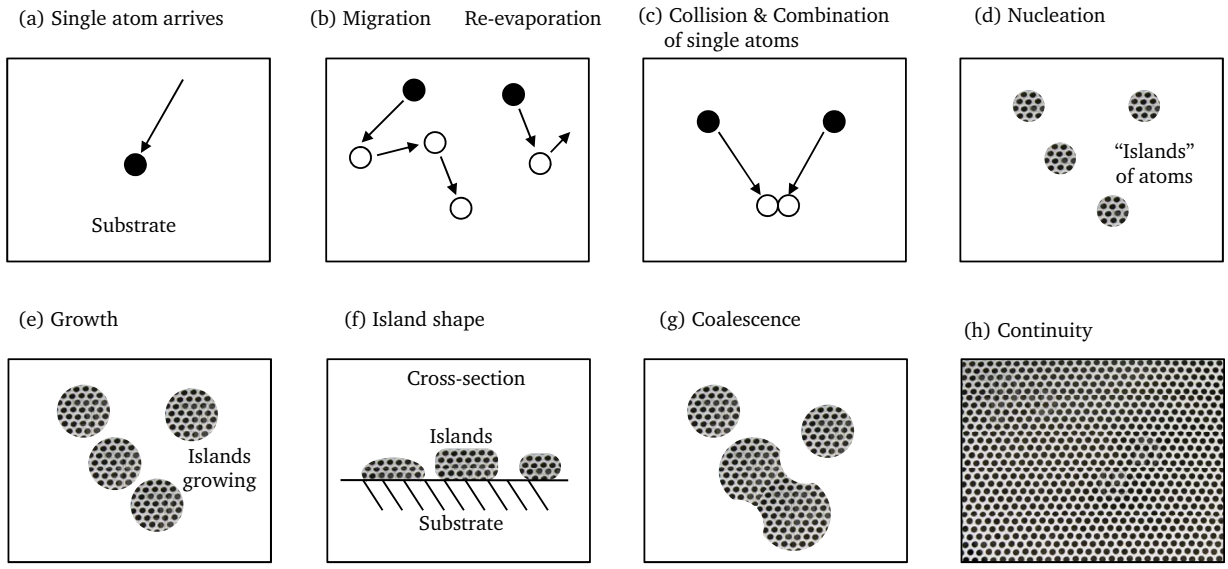

Figure 2.11: Formation of a thin film (adapted from [63]).

Sputtering deposition is carried out under vacuum. The material arrives at the substrate mostly in an atomic form. The atom diffuses around the substrate with a motion determined by its binding energy to the substrate and is influenced by the nature as well as the temperature of the substrate. Energetically, the surface of the substrate has adsorption sites for the depositing and diffusing atom. As represented in Figure 2.11, once finding an adsorption site, the atom can jump into an adjacent site, might re-evaporate or join another diffusing single atom to form a doublet, which is less mobile but more stable than a single atom. The chances of forming the atomic pair depend on the single atom density and on the arrival or deposition rate. As time advances, other single atoms join he doublets to form triplets, quadruplets and so on. This is known as the nucleation stage of the thin film growth, leading to the formation of quasi-stable "islands" with densities around $10^{10}/cm^2$ [63]. The islands grow in size rather than in number. Eventually they grow to be large enough to touch and agglomerate during the coalescence stage. Coalescence proceeds until the film reaches continuity, which usually occurs after the film is several Ångstroms in average thickness. During the island stage, each island is usually a single crystal or contains just a few crystals. Therefore, on a polycrystalline substrate (e.g. stainless steel) the orientation of each island is random, so that the resulting film is either polycrystalline or amorphous.

2.3.3 Conventional sputtering system

Figure 2.12 depicts the schematic of a conventional direct current (DC) sputtering system. The material to be sputtered is transformed into a sputtering target (nearly always a solid) which becomes the cathode of an electrical circuit, and has a high negative voltage (DC) applied to it. The substrate, that is intended to coat, is placed on an electrically grounded anode at a certain distance from the target. These electrodes

are housed in a chamber which is evacuated (known as base pressure). A sputtering gas, usually argon, is introduced into the chamber to some specified pressure (known as working pressure), commonly between 4×10^{-2} and 16×10^{-2} mbar . The action of the electric field is to accelerate electrons which in turn collide with argon atoms, breaking some of them up into argon ions and more electrons to produce the plasma. The charged particles are accelerated by the field, the electrons tending towards the anode (causing more ionization on the way) and the ions towards the cathode. When the ions strike the cathode, they undergo the possible interactions mentioned above. The secondary electrons are responsible for maintaining the electron supply and sustaining the plasma. The sputtered atoms from the target fly off in random directions and some of them land on the substrate (anode), condense and form the thin film. The rate of film formation (deposition rate) on the substrate depends mainly on the system pressure, the nature of the sputtering gas and the power applied to the circuit.

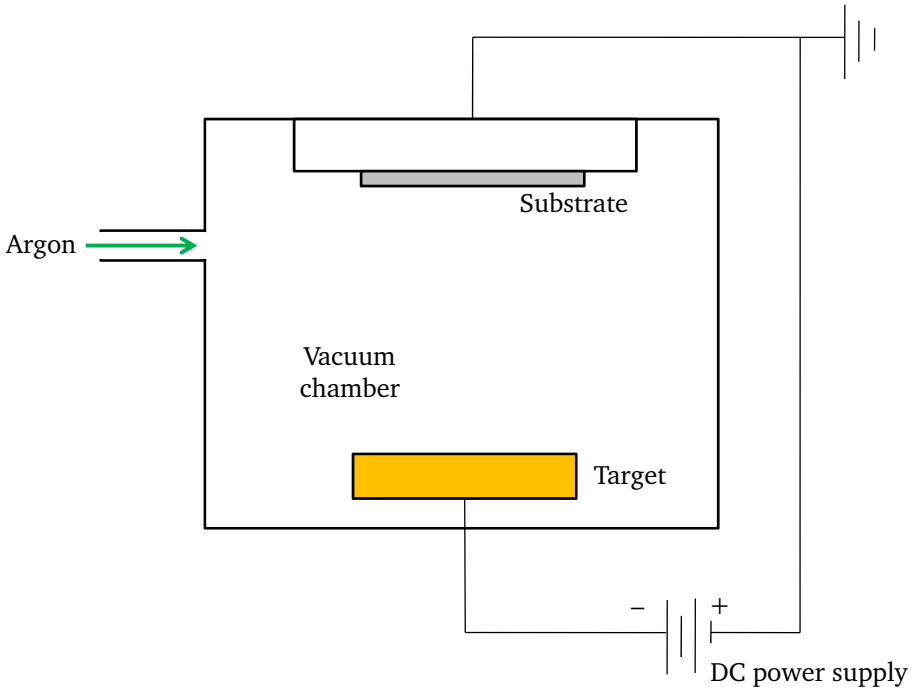

Figure 2.12: Schematic of a conventional DC sputtering system.

2.3.4 RF sputtering

If a substrate is intended to be coated with an electrically insulating material, DC sputtering is not suitable. When an insulator-covered electrode (i.e. a target of an insulator material) is placed in an independently sustained DC plasma, the surface of this electrode will charge up to a floating potential, so that the fluxes of ions and electrons to the surface become equal, regardless of the potential applied to the electrode, backing the insulator and generating the recombination of the ions and electrons at the surface of the electrode. To overcome this, an alternating voltage power, supplied at radio frequencies (RFs) around 10 MHz, can be used to generate the plasma. In this case, the target is alternately bombarded by ions and then electrons so as to avoid charge build-up. The positive charge accumulated during one half-cycle can be neutralized by electron bombardment during the next half-cycle. The RF sputtering makes a more efficient use of the electron impact ionization, so that working pressures could be practically reduced down to 1×10^{-3} mbar [63].

2.3.5 Magnetron sputtering

Magnetron systems are used in sputtering to attempt to trap electrons near the target so as to increase their ionizing effect. This is achieved by using perpendicular electric and magnetic fields. An electron emitted in the normal direction from the target into a magnetic field B parallel to the surface of the target, as represented in Figure 2.13, is rapidly accelerated away from the target because there is a strong electric field in the space above the target's surface. However, the electron stays within the space near the target in a cycloidal orbit due to the magnetic field. The net result is that the electron is trapped near the target. If trapped electrons do not collide, the loss process of fast electrons going to the substrate and walls of the vacuum chamber is eliminated. If the electron makes collisions (ionizing), the sustainability of the plasma is enhanced. Typical types of magnetrons include cylindrical, circular and planar magnetrons, depending on the application [63].

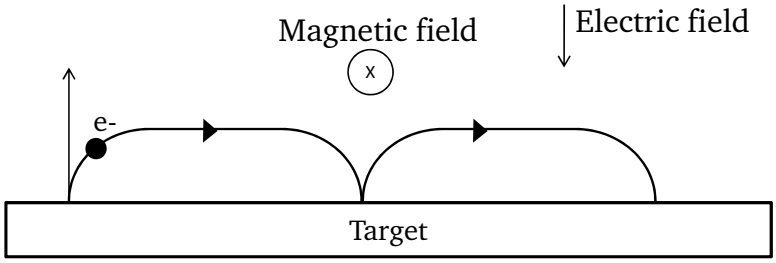

Figure 2.13: Motion of a electron ejected from the surface of the target into the region of a magnetic field parallel to the surface in the presence of a electric field.

3 Objectives

3.1 Main Objective

To evaluate the performance of sputtering as a technique to generate functional and stable coatings of different thermographic phosphors for applications of surface temperature measurements within combustion environments.

3.2 Specific objectives

- To prepare stable targets as sputter sources using sintering.
- To analyze the phase composition of the target materials via XRD.
- To determine appropriate parameters for sputtering the thermographic phosphors on stainless steel substrates.
- To physically and chemically characterize the sputtered coatings using surface science techniques.
- To verify the functionality at different temperatures of the thermographic phosphor coatings after sputtering using laser techniques.

4 Materials and Methods

This chapter details the methodology followed to prepare the phosphor targets and their characterization, the deposition of the thin films by RF magnetron sputtering, the chemical and physical characterization of the phosphor thin films and the evaluation of the temperature-dependent luminescence properties. At the end of the chapter, the description of the additional experiments on GGG:Cr powder samples is also included.

4.1 Synthesis of the targets

4.1.1 $CaTiO_3:Pr^{3+}$ target

The $CaTiO_3:Pr^{3+}$ target was prepared by the sol-gel combustion method combined with high temperature sintering. The sol-gel combustion method was used to prepare the precursor powder of $CaTiO_3:Pr^{3+}$ following two steps: xerogel formation and combustion reaction. The polymeric gel, combined with the fast combustion reaction, makes the method suitable to synthesise multicomponent systems, like $CaTiO_3:Pr^{3+}$, where the stoichiometry must be strictly maintained. After these steps the powder was ground and compressed to form the target. Finally, the target was sintered at 1373 K.

The flowchart in Figure 4.1 shows the experimental procedure followed to prepare the $CaTiO_3:Pr^{3+}$ precursor powders with a Pr doping concentration of 1 mol% (with respect to the Ca content). $CaCO_3$, $Ti(OC_4H_9)_4$, and $Pr(NO_3)_3{\cdot}5H_2O$ were used as starting materials. During the first step, $CaCO_3$ and $Ti(OC_4H_9)_4$ were converted into $Ca(NO_3)_2$ and $Ti(NO_3)_4$ in aqueous solution using nitric acid, HNO_3. After this, $Pr(NO_3)_3{\cdot}5H_2O$ was added to the solution. The metal nitrates aqueous solution was then heated under magnetic stirring in the presence of citric acid ($C_6H_8O_7{\cdot}H_2O$), which acts as chelating agent promoting gel polymerization. Next, the xerogel synthesis was performed at low temperature (353 K) during several hours to ensure the homogeneity at the atomic scale, preventing preferential precursor precipitations. The combustion reaction step is a strong exothermic and autocatalytic reaction of the xerogel. It was activated in an electric furnace at a temperature of 473 K during 20 minutes, resulting in a yellowish foam. The fastness of the combustion reaction prevented any phase segregation phenomena, preserving the stoichiometry. The foam was finally ground to form the precursor powder. The sol-gel combustion procedure was repeated for three different batches to produce enough precursor powder for the target preparation. Table 4.1 summarizes the amounts of starting materials used for each individual batch.

Table 4.1: Amounts of starting materials used for the production of $CaTiO_3:Pr^{3+}$ precursor powders.

Component	Amount (g)		
	Batch A	Batch B	Batch C
$Pr(NO_3)_3{\cdot}5H_2O$	0.0806	0.0757	0.0814
$Ti(OC_4H_9)_4$	6.3040	5.9209	6.3640
$CaCO_3$	1.8579	1.7413	1.8716
$C_6H_8O_7{\cdot}H_2O$	7.7851	7.3119	7.8592

The sintering of the target was divided in three steps: (1) the three batches of precursor powders were sintered in air at 873 K for 6 hours using the controlled temperature ramp in Figure 4.2 (a) in an electric

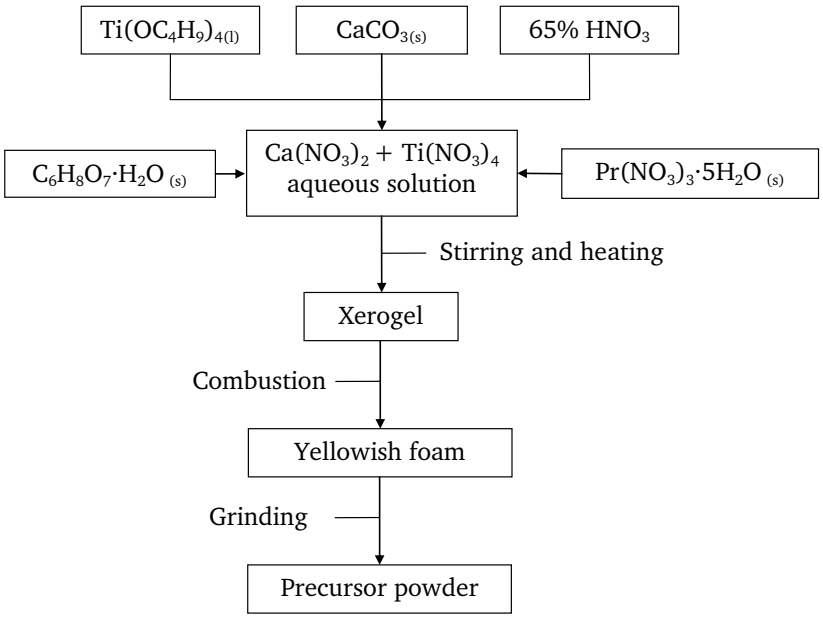

Figure 4.1: Flowchart of the sol-gel combustion method used to prepare the precursor powder of $CaTiO_3:Pr^{3+}$.

furnace (Carbolite CWF 1200, T_{max} = 1473 K) equipped with a temperature controller (Eurotherm 2416); (2) The three sintered batches were ground again, mixed and slowly compressed, using the tool described in Figure 4.3, up to 980 MPa to form the target; (3) The target was finally sintered in air at 1373 K for 6 hours using the controlled temperature ramp in Figure 4.2 (b). The temperature for sintering the precursor powders was selected to guarantee the synthesis of $CaTiO_3:Pr^{3+}$ while keeping a good compressibility of the powder. The maximum temperature for sintering the target was limited by the maximum temperature of the furnace.

4.1.2 $Gd_3Ga_5O_{12}:Cr^{3+}$ target

The $Gd_3Ga_5O_{12}:Cr^{3+}$ target, with a Cr doping concentration of 0.5 mol% (with respect to the total content of metals), was prepared by high-temperature solid-state reactions using an ammonium hydroxide process as represented in Figure 4.4. Five individual batches, with the same composition, were prepared with the amounts listed in Table 4.2. For each individual batch, high-purity (99.99%) oxides of gallium (Ga) and gadolinium (Gd) in the correct proportions were dissolved in hot, concentrated nitric acid (HNO_3) under magnetic stirring. The stoichiometric amount of $Cr(NO_3)_3{\cdot}9H_2O$ was added to the solution. After stirring well, the Gd and Cr metal nitrates are in aqueous solution while the Ga_2O_3 stays as solid particles. A NH_4OH solution was added to form a ultrafine precipitate of $Gd(OH)_3$ and $Cr(OH)_3$ covering the Ga_2O_3 particles. This with the aim of increasing the contact area between the metal oxides during the solid-state reactions. The precipitate was then washed with water and dried in air to remove the NH_4NO_3 by-product and excess of NH_4OH.

Table 4.2: Amounts of starting materials to produce the $Gd_3Ga_5O_{12}:Cr^{3+}$ target.

Component	Amount (g)
$Cr(NO_3)_3{\cdot}9H_2O$	0.0400
Gd_2O_3	2.1750
Ga_2O_3	1.8650

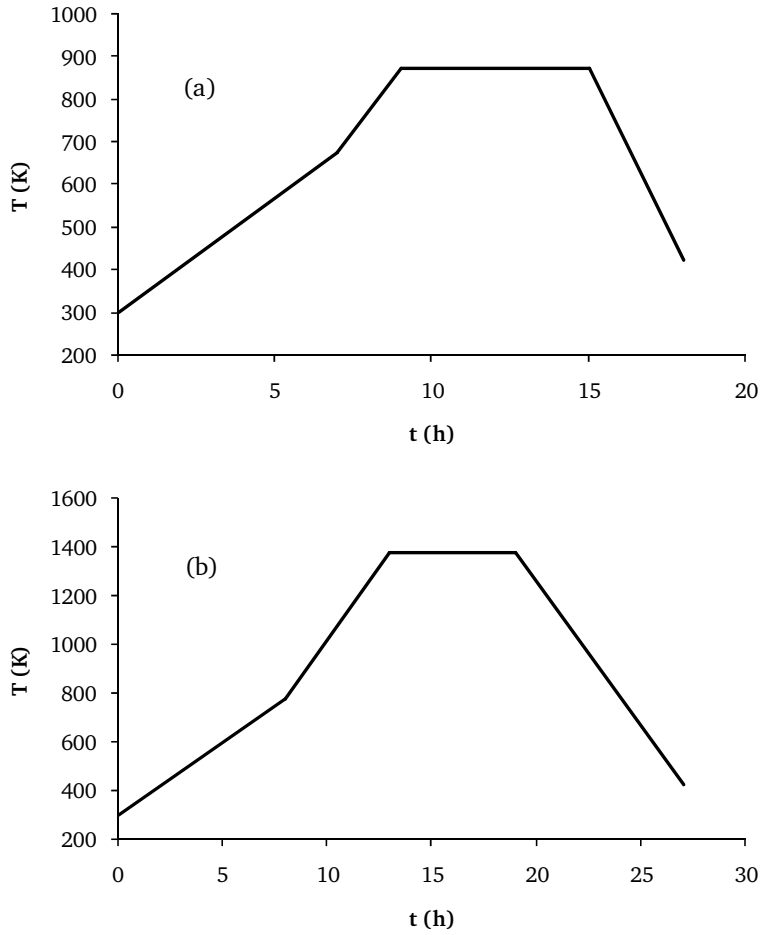

Figure 4.2: Controlled ramps for the sintering of $CaTiO_3$:Pr^{3+} (a) precursor powders and (b) target.

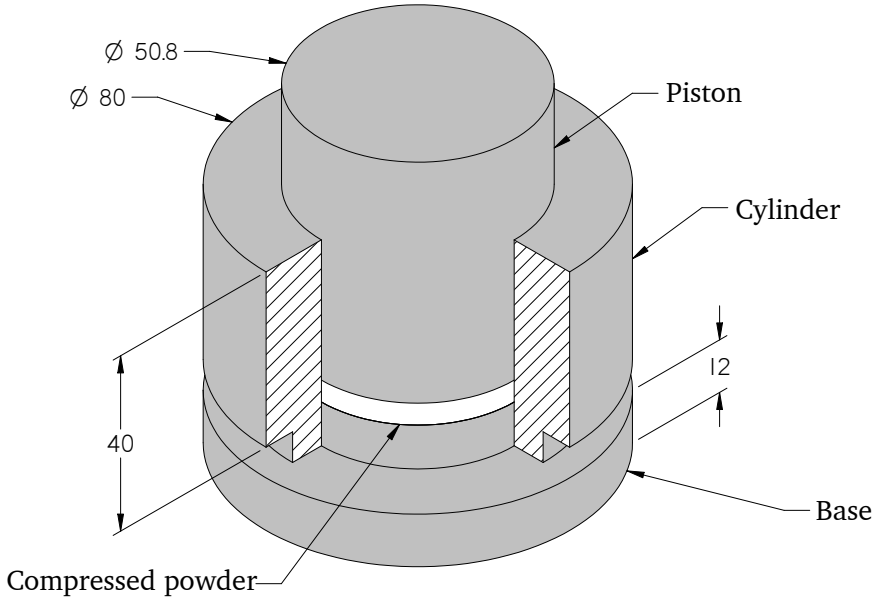

Figure 4.3: Tool for the compression of powders. The powders were introduced in the cylinder and compressed to form the targets by applying a pressure normal to the piston (dimensions in mm).

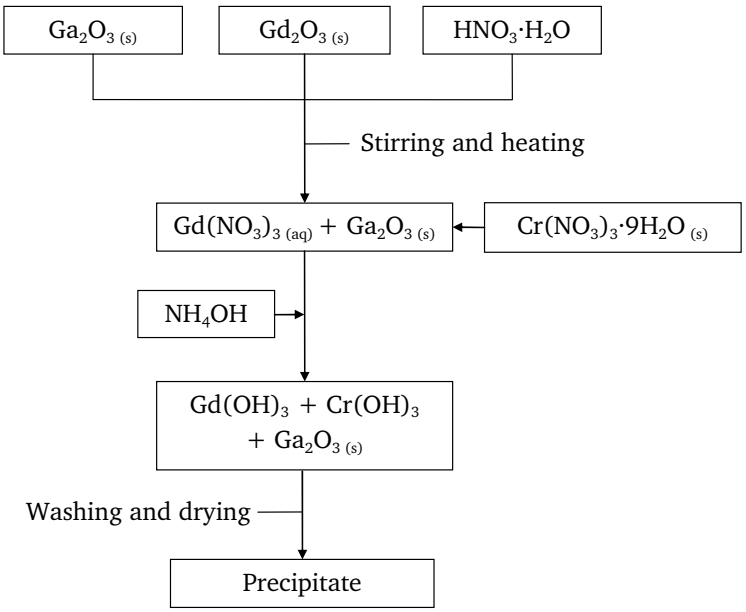

Figure 4.4: Flowchart of the method used to prepare the GGG:Cr^{3+} target.

After drying, the precipitate was grounded. The five grounded powders were mixed and slowly compressed, with the tool in Figure 4.3, up to 980 MPa to form the target. The target was sintered in air at 1373 K for 6 hours, using the controlled ramp shown in Figure 4.5, to convert the hydroxide into a crystalline garnet of $Gd_3Ga_5O_{12}$:Cr^{3+}

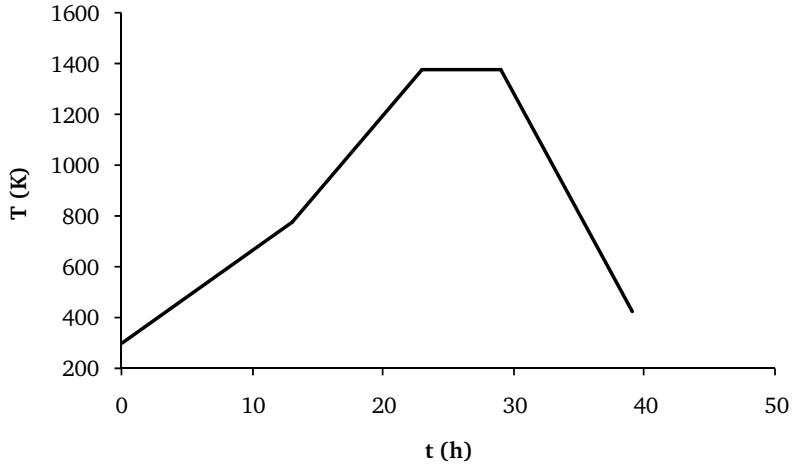

Figure 4.5: Controlled ramp for the sintering of the $Gd_3Ga_5O_{12}$:Cr^{3+} target.

4.2 Characterization of the targets

The composition and crystal structure of the targets and the corresponding precursor powders was studied using a X-ray diffraction technique (XRD). X-ray scattering is a family of non-destructive analytical techniques which provides information about the crystallographic structure and chemical composition of solids. These techniques are based on the scattering X-rays hitting a crystalline substance. X-ray wavelengths are comparable with inter-atomic distances (∼1Å). Therefore, it is regarded an excellent means of crystal diffraction study for this length scale. Atoms scatter X-ray waves, primarily through the atoms'

electrons that can emanate secondary spherical waves. This phenomenon is known as elastic scattering, and the electron shell is known as the scatterer. A regular array of scatterers produces a regular array of spherical waves. Although these waves cancel each other out for most of the directions through destructive interference, they add constructively in a few specific directions, determined by Bragg's law:

$$n \cdot \lambda = 2 \cdot d \cdot \sin\theta \tag{4.1}$$

where n is an integer determined by the order given, λ is the wavelength of the X-rays , d is the spacing between the planes in the atomic lattice and θ is the angle between the incident ray and the scattering planes.

Representative powder samples collected from the targets and the precursor powders were used for the characterization with X-ray diffraction. A powder sample consists of an enormous number of randomly orientated small crystallites. In such a sample, various lattice planes are present in every possible orientation. For each set of planes, therefore, at least some crystals must be oriented at the Bragg angle, to the incident beam and thus, diffraction occurs for these crystals and planes. A powder diffractogram contains information about the diffraction angles and their corresponding intensities. Factors such as crystal class, lattice type, symmetry, unit cell parameter, the distribution and type of atoms in the unit cell affect the intensity and number of reflections. As a result, nearly all crystalline solids have a unique powder X-ray diffraction pattern in terms of position and intensities of the observed reflections.

The X-ray measurement of the powder samples was performed on a STOE Stadi P diffractometer at room temperature. A position sensitive detector in Debye-Scherrer geometry was used (see Figure 4.6). In this geometry, a monochromatic incident beam uniformly illuminates the powder sample, the 2θ angle between the incident and scattered beams, is fixed for a given Bragg reflection. The Debye-Scherrer geometry employs a parallel beam that uniformly illuminates the powder sample. The detector is placed near the scattering plane. A series of slits, known as Soller slits, are employed to define the incident and scattered beam directions. The main advantage of this geometry is that the sample can be easily rotated around its axis to obtain a good average and to eliminate part of the non-randomness of the powder sample.

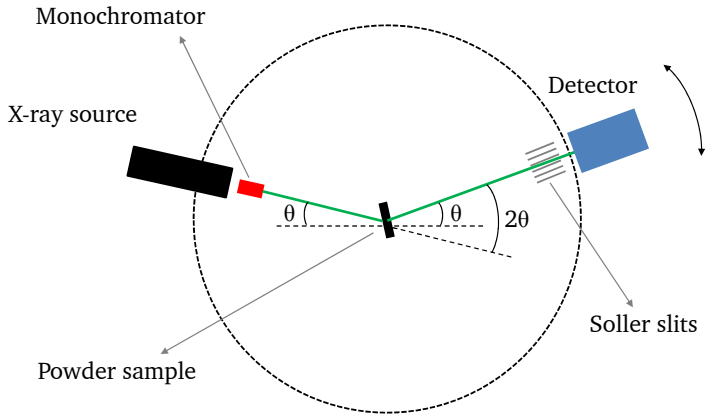

Figure 4.6: Powder diffractometer in Debye-Scherrer geometry.

The diffractometer is equipped with a copper anode and curved germanium (111) monochromator with Cu-$K_{\alpha 1}$ radiation of wavelength 1.54056 Å. The obtained powder X-ray pattern was analysed by using the software provided by STOE [64]. The materials were identified by comparing with well known substances, with crystallographic data provided by the International Centre for Diffraction Data (ICDD) data base, which are included in the software [64].

4.3 Deposition of the thin films

4.3.1 Surface preparation machine

The deposition of the thin films of $CaTiO_3$:Pr^{3+} and $Gd_3Ga_5O_{12}$:Cr^{3+} was carried out using an Omicron ultra high vacuum (UHV) system for surface preparation [65]. The machine, with the main components highlighted, is represented in Figure 4.7. The system consists of a main vacuum chamber equipped with a turbo-molecular pump, an ion getter pump, a titanium sublimation pump, a fast entry lock chamber, a sample transfer system, a mobile sample holder stage, two independent sputtering sources for targets of 50.8 mm dia., a sample heating system and a set of instrumentation and controllers including an automatic pressure controller. The system allows typical preparation methods such as sputtering, annealing and evaporation coating.

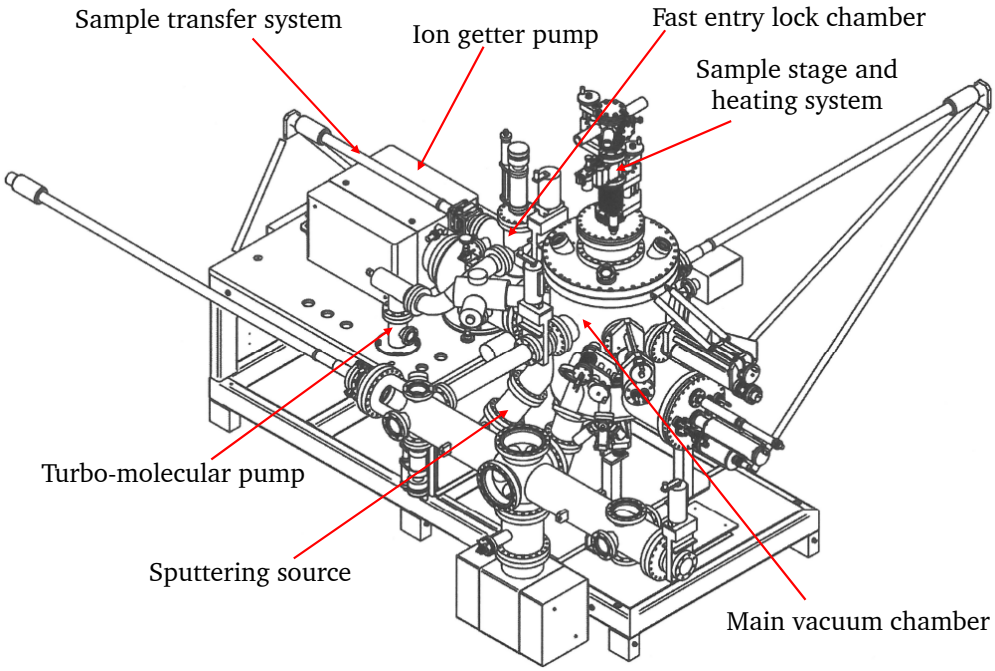

Figure 4.7: 3D schematic of the surface preparation machine (adapted from [65]).

4.3.2 Sputtering setup and parameters

The system was set up to use sputtering as deposition technique. Figure 4.8 illustrates a schematic of the main components inside the main vacuum chamber. The $CaTiO_3$:Pr^{3+} and $Gd_3Ga_5O_{12}$:Cr^{3+} targets were simultaneously installed in the two independent sputtering sources with the advantage of carrying out independent deposition experiments for both phosphors without venting the main chamber. To install the targets they had to be bonded first to copper backing plates using a commercial silver epoxy glue (Lesker KL-325K) and then they were hold in the sources by magnetic keepers as shown in Figure 4.9. The epoxy bonding guaranteed enough mechanical and thermal strengths as well as good heat conduction to allow proper cooling of the targets.

After installing the targets, the main chamber was first pumped down from atmospheric pressure to pressures around 5×10^{-8} mbar and then down to around 1×10^{-8} mbar using the ion getter pump. In this experiment there was no need to use the titanium sublimation pump. Four substrates were installed

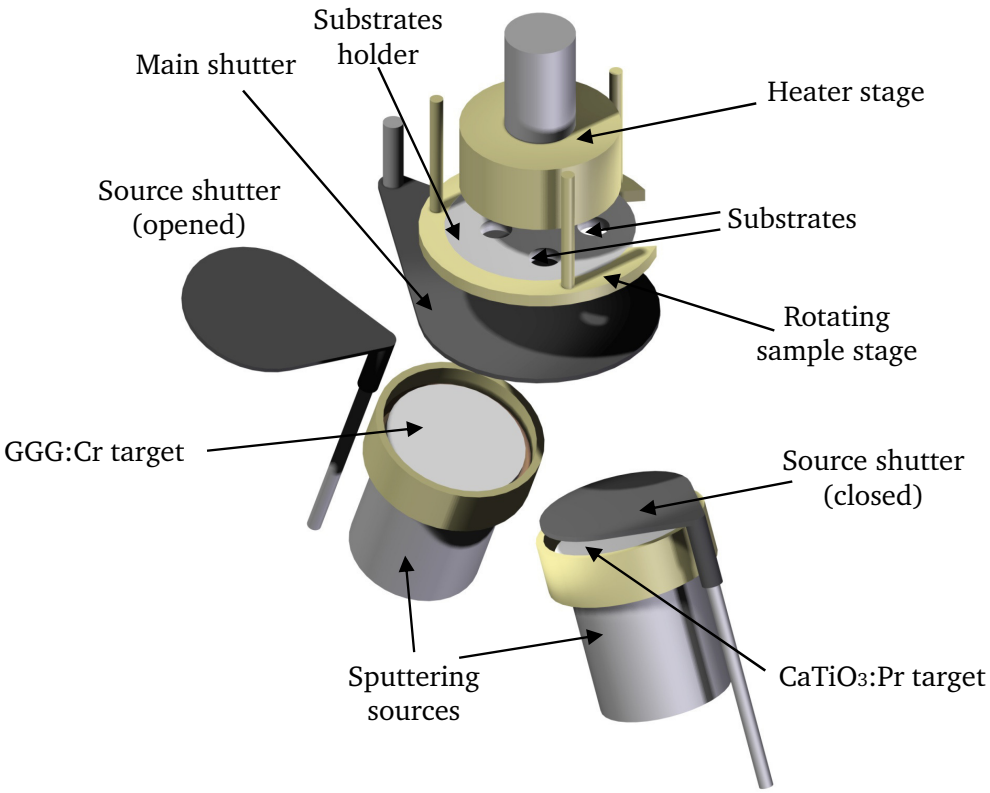

Figure 4.8: Details of the set up inside the main vacuum chamber.

simultaneously during each individual experiment using a 2-inch diameter sample holder. In the case of $CaTiO_3:Pr^{3+}$, two substrates of stainless steel (1.4301 or 304) and two of indium tin oxide (ITO)/glass were used while for $GGG:Cr^{3+}$ three substrates of stainless steel and one of quartz glass were employed. For each deposition experiment the sample holder with new substrates could be easily installed inside the main chamber using the fast entry lock and the transfer system without venting the whole system.

Films of $CaTiO_3:Pr^{3+}$ and $GGG:Cr^{3+}$ were deposited by RF magnetron sputtering, using the same set up but with different parameters. Table 4.3 summarizes the most important parameters used for the deposition of the $CaTiO_3:Pr^{3+}$ and $GGG:Cr^{3+}$ films. As both targets are insulators typical DC sputtering configurations are not suitable. When an insulator is placed in a DC discharge, its surface charges up to a floating potential, so that the fluxes of ions and electrons to the surface become equal and recombine on the surface of the target extinguishing the discharge. To overcome this, a RF discharge can be applied so that the positive charge accumulated during one half-cycle can be neutralized by electron bombardment during the next half-cycle. A RF generator (Seren IPS Inc. R301, max. power 400 W) and an automatic matching network (Seren IPS Inc. MC2) were used to produce an almost continuous discharge since the target is alternately bombarded by ions and then by electrons to avoid charge build-up. Additionally, a circular magnetron configuration (see Figure 4.9 (b)) was employed to trap electrons near the target increasing their ionizing effect. In this configuration the sputtered material has a pronounced forward direction perpendicular to the center magnet. Therefore, the sample holder was rotated to ensure good uniformity of the film thickness.

High-purity Argon (grade 5.5) was selected as sputtering gas due to its facility to be ionized, inert nature and availability. A small amount of oxygen was added to the sputtering gas with two purposes, avoiding any change of the targets oxidation state and restoring the stoichiometry of deposited films which usually have a deficiency of oxygen when using metal oxide targets. Flows of 38 sccm of Ar and 2

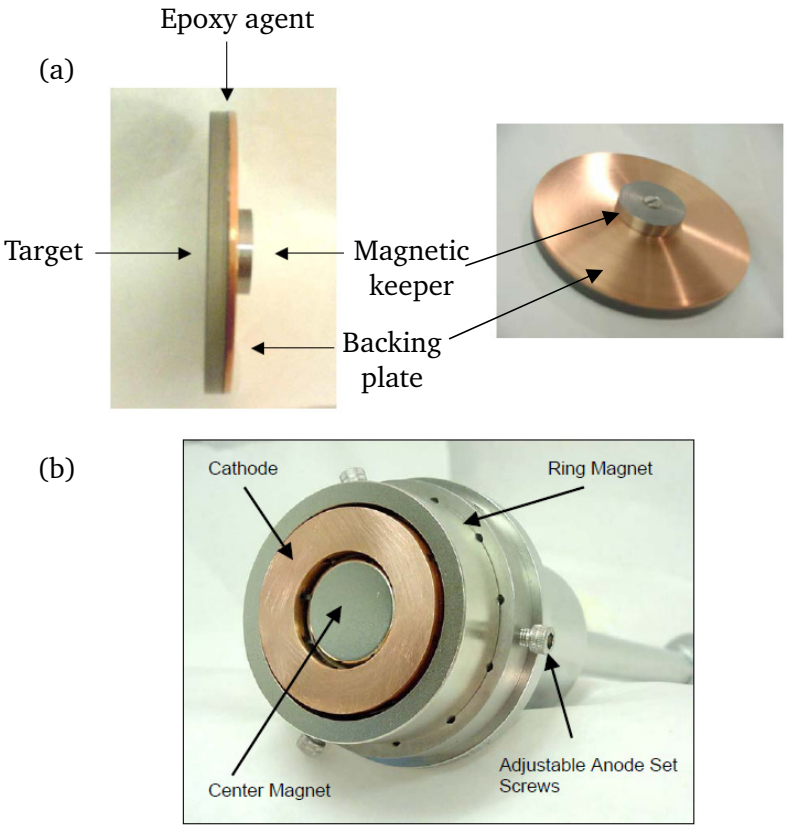

Figure 4.9: (a) Bonding of target to the backing plate and (b) sputtering source [65].

Table 4.3: Sputtering parameters for the deposition of $CaTiO_3:Pr^{3+}$ and $GGG:Cr^{3+}$ films.

Parameter	Value	
	$CaTiO_3$:Pr	GGG:Cr
RF power (W)	100	60
Base pressure (mbar)	1×10^{-8}	1×10^{-8}
Working pressure (mbar)	0.011	0.011
$O_2/(Ar + O_2)$ (mol%)	5	5
Substrate temperature (K)	623	723

sccm of O_2 combined with a working pressure of 0.011 mbar produced stable plasmas for both targets. The working pressure during the deposition was automatically controlled by changing the gate valve position of the turbo-molecular pump with a pressure controller (VAT 641 PM-5). The substrates were located at around 10 cm above the target (see Figure 4.8) and were heated with a heating stage during the process to facilitate the formation of the films. Prior to each deposition, the targets were cleaned using the plasma for 15 min with the shutters closed. After this time, the main shutter and the source shutter were opened to start the deposition for several hours until achieving the desired film thickness. The temperature of the sputtering sources and the targets were kept as low as possible using a water cooling system during the deposition experiments to avoid any damage or change of the targets.

4.3.3 Annealing of the phosphors films

The phosphor films were annealed after deposition to restore their right crystal structure. $CaTiO_3:Pr^{3+}$ films were annealed at 2×10^{-6} mbar and 973 K for 4 hours using the surface preparation machine

described in section 4.3.1. Due to temperature limitations of the preparation machine, GGG:Cr^{3+} films were annealed at 1173 K for 12 hours in N_2 atmosphere at atmospheric pressure and using an electric quartz tube furnace Carbolite (SPLF 77720, T_{max} = 1673 K) with an automatic temperature controller (Eurotherm 2416).

4.4 Characterization of the thin films

4.4.1 X-ray photoelectron spectroscopy

X-ray photoelectron spectroscopy (XPS) was used to investigate the chemical composition of the deposited films. As represented in Figure 4.10 (a), XPS is based on the fact that a photon of sufficiently short wavelength (i.e. high energy) can ionize an atom, producing an ejected free electron by the photoelectric effect. Surface analysis by XPS is accomplished by irradiating a sample with monochromatic x-rays and measuring the energy of the detected electrons. The X-rays have usually a limited penetration, of the order of 1 to 10 micrometers, in solids [66]. The kinetic energy KE of the emitted electrons (the photoelectrons) depends on the energy of the photon $h\upsilon$ and can be expressed by:

$$KE = h\upsilon - BE - \phi_s \tag{4.2}$$

where BE is the binding energy of the atomic orbital from which the electron originates and ϕ_s is the spectrometer work function. The binding energy may be regarded as the energy difference between the initial and final states after the photoelectron has left the atom. Because there is a variety of possible final states of the ions from each type of atom, there is a corresponding variety of kinetic energies of the emitted electrons. Moreover, there is a different probability or cross-section for each final state.

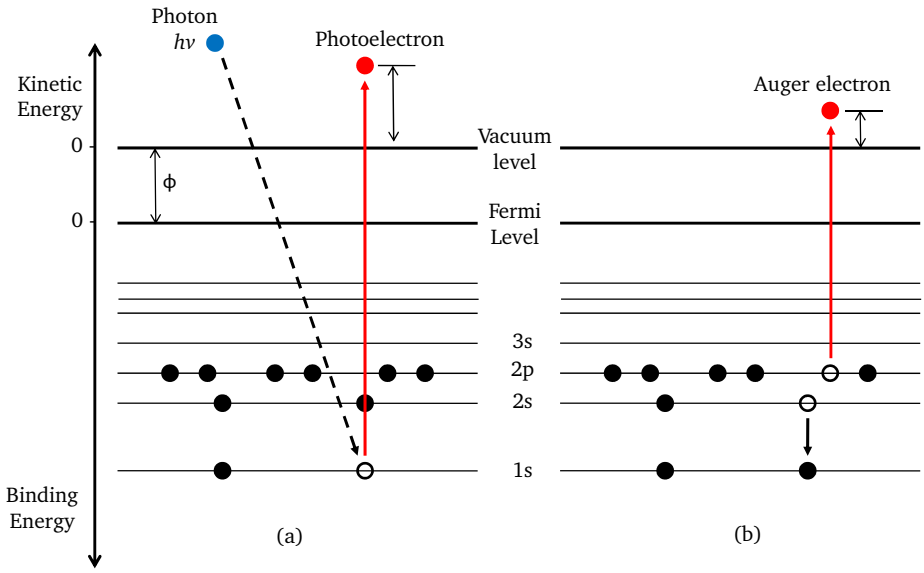

Figure 4.10: (a) XPS emission process and (b) relaxation process for a model atom.

Figure 4.11 schematically represents the relative binding energies and ionization cross-section of an example atom of uranium. By definition, the Fermi level corresponds to zero binding energy and the depth under the Fermi level in the figure indicates the binding energy of the electron or the relative energy of the ion remaining after electron emission. The line lengths indicate the relative probabilities of the various ionization processes. The p, d and f levels become split upon ionization, leading to vacancies

in the $p_{1/2}$, $p_{3/2}$, $d_{3/2}$, $d_{5/2}$, $f_{5/2}$ and $f_{7/2}$. Because each element has a unique set of binding energies, XPS can be used to identify and determine the concentration of the elements in the surface [66]. Auger electrons may be emitted because of relaxation of the excited ions remaining after photoemission. As represented in Figure 4.10 (b), an outer electron falls into the inner orbital vacancy, and a second electron is simultaneously emitted, carrying off the excess of energy.

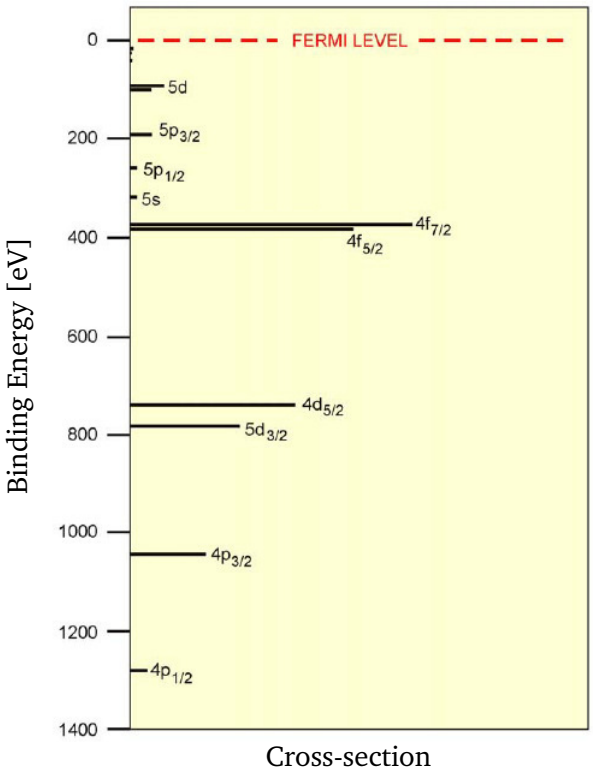

Figure 4.11: Relative binding energies and ionization cross-section of Uranium (adapted from [66]).

The ionization process in the sample occurs at a depth of a few micrometers but only those electrons that originate within tens of angstroms below the surface can leave the surface without energy loss producing the peaks in the spectra. The electrons that undergo inelastic loss processes before emerging form the background. The electrons leaving the sample are detected by an electron spectrometer according to their kinetic energy. The analyzer is usually operated as an energy window, referred to as pass energy, accepting only those electrons having an energy within this range. The pass energy is fixed and the scanning for different energies is accomplished by applying a variable electrostatic field before the analyzer. Photoelectrons are finally detected as discrete events recording the number of electrons for a given detection time and energy.

The XPS system used for the analysis of the deposited films consisted of an Al-K_α source (operating at 15kV and 400 W), a monochromator (Specs FOCUS 500), a hemispherical energy analyzer (Specs PHOIBOS 150) with a lens aperture of 1.5 kV and a slit of 7 × 20 mm, and an electron multiplier detector (Specs MCD-9). The measurements were performed at 1×10^{-10} mbar with an excitation energy of 1486.61 eV and a pass energy of 20 eV. Survey scans were measured up to binding energies of 1300 eV with steps of 0.5 eV. For quantification purposes, detailed scans of the main peaks were measured with steps of 0.05 eV. The spectra were recorded and analyzed using the SpecLab software.

4.4.2 XRD of the thin films

The conventional configuration used for X-ray diffraction (XRD) of thick samples is the Bragg-Brentano geometry. In this one, the X- ray beam is incident at an angle typically between 15° and 50°. The depth of penetration into the sample is given by the absorption length times the sine of the incidence angle. If the sample is a thin layer, most of the X-ray beam passes through the film and is scattered by the substrate. To study the crystal structure of the thin films and since polycrystalline substrates of stainless steel were used for the deposition, the thin-film XRD configuration shown in Figure 4.12 was chosen to maximize the XRD signal from the thin film while suppressing the XRD signal from the substrate.

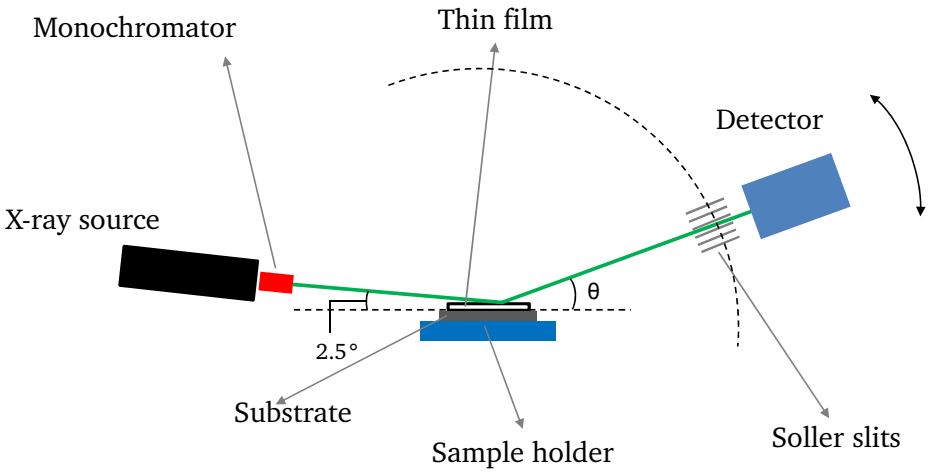

Figure 4.12: Stadi P diffractometer in the thin-film configuration.

The key in thin-film XRD is to choose very small angles of incidence, increasing the path length of the X-rays in the film and reducing the amount of X-rays that penetrate through to the substrate. An incidence angle of 2.5° was set using the same STOE Stadi P diffractometer. During the measurements the incidence angle was fixed and the detector scanned over the range of diffraction angles because most of the diffraction peaks from the samples lie in the region $20° \leq 2\theta \leq 100°$.

4.4.3 Film thickness

Mean values of the film thickness were estimated using a surface profilometer (Bruker Dektak XT). This is an instrument commonly used for surface texture analysis as it measures the surface topography of a sample to reveal a topographical image of the surface. The surface profilometer was equipped with a diamond-tipped stylus moving vertically and laterally to scan across the surface of the sample. To estimate the mean thickness of the deposited films, the stylus profilometer measured vertical displacements as a function of position at different edges of the films. The film thickness was then calculated as the mean value of the difference of the vertical displacement at the film position and the vertical displacement at the substrate position. For a better estimation, the films deposited on ITO/glass and quartz glass were used for the measurements of the $CaTiO_3$:Pr^{3+} and GGG:Cr^{3+} films, respectively, due to their superior surface quality over the stainless steel substrates.

For comparison, the thickness of the films were estimated using a thickness/deposition rate monitor (Sycon Instruments STM-100/MF) prior deposition. This instrument uses the time-proven 6 MHz oscillating quartz crystal as the sensor device. The sensor was located inside the main vacuum chamber at the

same position of the substrates. The plasma was ignited with the same parameters of Table 4.3, except for the high temperatures of the substrates to avoid damaging the sensor. The thickness / deposition rate monitor uses the resonant frequency of the exposed quartz crystal to sense the mass of deposited films attached to its surface. There is a known relationship between the mass of such a film and the measured frequency of the sensor crystal. Knowing the frequency change due to accumulated mass, film thickness is determined by the following equation:

$$A_f = \left[\frac{N_q \cdot D_q}{\pi \cdot D_f \cdot Z \cdot F_c} \right] \cdot \arctan \left[Z \cdot \tan \left[\frac{\pi \cdot (F_q - F_c)}{F_q} \right] \right] \tag{4.3}$$

where A_f (Å) is the film thickness, $N_q = 1.668 \times 10^{13}$ HzÅ is the frequency constant for AT-cut quartz, $D_q = 2.648$ g/cm^3 is the density of quartz, D_f (g/cm^3) is the density of the material, F_q and F_c are the frequencies of the sensor crystal prior and after depositing material on it, respectively (these values are not revealed by the manufacturer), and Z is a factor of the material defined as:

$$Z = \left[\frac{D_q \cdot U_q}{D_f \cdot U_f} \right] \tag{4.4}$$

where D_q and D_f are the densities and U_q and U_f are the shear modulus of the quartz and film materials, respectively.

4.5 Evaluation of the thermographic functionality of the thin films

4.5.1 Measurement of the luminescence lifetime

To evaluate the luminescence functionality of $CaTiO_3$:Pr^{3+} and GGG:Cr^{3+} thin films, measurements of the luminescence lifetime at different temperatures were carried out using the setup represented in Figure 4.13. The fourth harmonic (266 nm) of a non-focused, pulsed, Q-switched Nd:YAG laser (Quanta Ray, INDI, repetition rate: 10 Hz, pulse width 5-8 ns) was used to excite luminescence. The pulse energy was adjusted by the combination of a half-wave-plate and a Glan polarizer and it was referenced by a pyroelectric energy detector (Gentech- EO, QE25-SP-S-MB). The laser beam profile was spatially limited by two apertures with diameters of 4 mm and 2 mm placed at distances of 3000 and 1200 mm from the phosphor sample, respectively.

For spatial filtering and for minimizing the influence of blackbody radiation and other interfering light, the emitted luminescence light was imaged onto a pinhole (d = 100 μm) by a commercial 85 mm Nikkor camera lens. In order to enable homogeneous illumination of the photomultiplier tube (PMT) the signal was collimated by a plano-convex lens (f = 30 mm) behind the pinhole. The photomultiplier current was read out by an oscilloscope (Tektronix 5032B, 350 MHz) at an input resistance of 512 Ω and a cable capacity of C = 300 pF resulting in a threshold lifetime of τ = 153 ns.

For measurements above room temperature, the samples were placed within an optically accessible tube furnace (Carbolite, CTF 12/100/900, inner tube diameter: 105 mm, tube length: 900 mm, T_{max} = 1473 K). The furnace was equipped with a type N thermocouple (TMH GmbH, Maintal, Germany, specified accuracy of 0.4% in the designated temperature range), which was directly mounted in contact with the phosphor sample. Prior to the measurement of temperature/luminescence characteristics, the furnace was heated up until the sample reached its desired maximum temperature. After switching off the furnace, measurements of the lifetime decay were performed at decreasing temperature in steps of ΔT = 10 K. Due to the inherent decelerating of the cooling down rate, the measurements were aborted before

reaching room temperature (at 310 K).

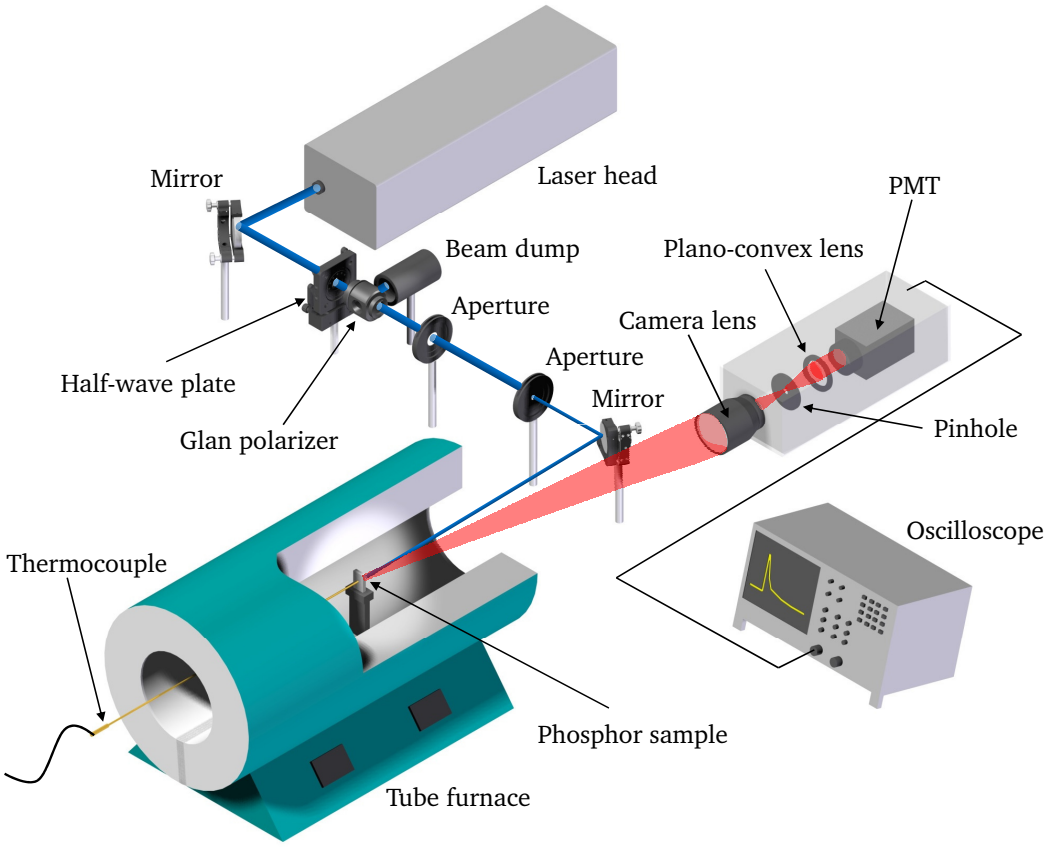

Figure 4.13: Experimental setup for the measurement of the luminescence lifetime.

Measurements of the temperature-dependent luminescence lifetimes of the $CaTiO_3:Pr^{3+}$ and $GGG:Cr^{3+}$ thin films were performed at a pulse energy of 1 mJ after the second aperture. In the case of the $CaTiO_3:Pr^{3+}$ film, 200 single-shots were recorded by the PMT at each referred temperature within the range from 310 to 500 K while 100 single-shots were recorded in the case of the $GGG:Cr^{3+}$ film within the range from 310 to 1000 K. These surface temperature ranges are of relevance within combustion environments [9]. At a laser pulse repetition rate of 10 Hz and an average cooling down rate of approximately 0.03 K s^{-1}, the sample temperature change during the acquisition of each set of single-shots was in the order of 0.6 and 0.3 K for $CaTiO_3:Pr^{3+}$ and $GGG:Cr^{3+}$, respectively. With the aim of comparing the luminescence properties of the source material and the deposited film, the lifetimes of the $GGG:Cr^{3+}$ target were measured using the same setup (Figure 4.13) and at the same temperature range used for the film. The stability of the coatings was also checked after each experiment. In this thesis, a stable coating is referred as a thin film that is still adhered to the substrate after laser excitation and/or high temperature treatment.

The emission spectra of the samples was monitored at room temperature by a spectrometer (Stellar Net STE-EPP2000-C, grating 600 lines/mm, slit width: 50 μm, max. resolution =1.5 nm) within a spectral range of 200 to 850 nm. The transfer function of the spectrometer was corrected by a spectrally calibrated light source (Ulbricht sphere, Gigahertz-Optik UMBB-300).

4.5.2 Spatially resolved lifetime characteristics

To evaluate the spatial homogeneity of the lifetime characteristics of the deposited films, the experimental setup was modified, as represented in Figure 4.14, to measure the 2D luminescence lifetime of the deposited films. The Gaussian beam profile was converted into a top-hat profile by a beam homogenizer (Holo Or, Israel, diffusing angle: 0.68°) in order to ensure spatially homogeneous excitation. The luminescence was monitored by a high-speed CMOS camera (LaVision High Speed Star 6, maximum frame rate: 675 kHz, dynamic range: 12 bit), equipped with a Nikkor 50 mm photo lens. Due to signal strength limitations, this experiment was only carried out for the GGG:Cr^{3+} thin film. The spatially resolved luminescence was evaluated at room temperature recording images of 100 single-shots with an excitation energy of 40 mJ (after the first aperture).

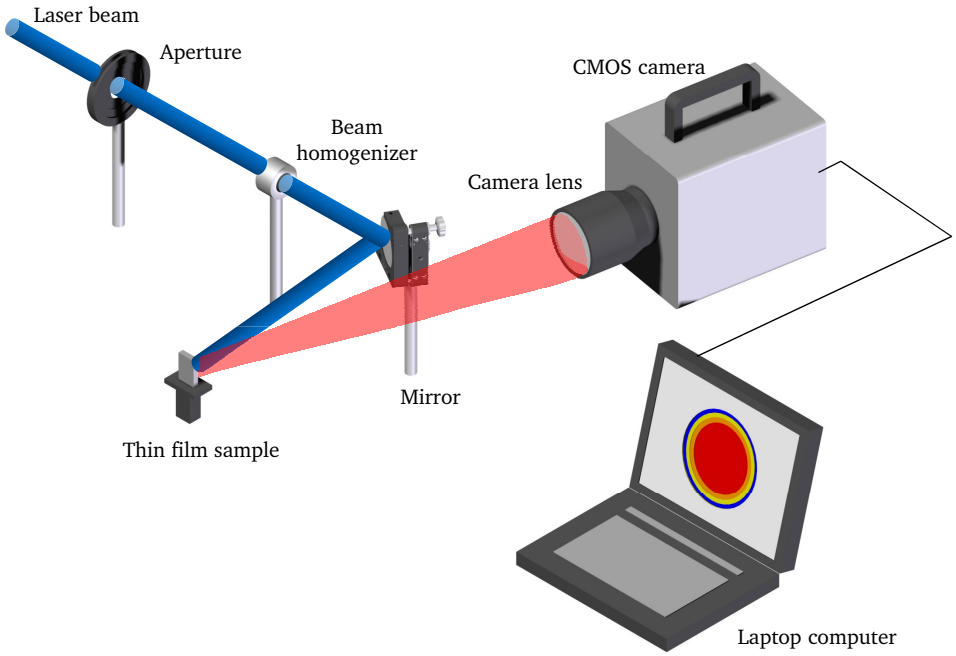

Figure 4.14: Modified experimental setup for the spatially resolved experiment.

4.5.3 Data evaluation

For the evaluation of the temperature-dependent luminescence characteristics, the measured decay signals of the thin films were converted to scalar lifetimes, τ, using the iterative fitting algorithm of Brübach *et al* [8], modified by Fuhrmann *et al* [67]. In this algorithm, the single-shot waveforms are approximated by a mono-exponential decay

$$I(t) = I_0 exp^{-\frac{t}{\tau}} + b \tag{4.5}$$

where I_0 is the initial intensity at t_0 and b is the off-set intensity, which is computed by averaging the signal intensity prior to the respective laser pulse. The linear regression of the sum (LRS), as introduced by Everest and Atkinson [68], is applied to determine the luminescence lifetime τ. LRS uses the fact that the integral of the decay waveform (Equation 4.6)

$$\int_o^t I(t)dt = \int_o^t (I_0 exp^{-\frac{t}{\tau}} + b)dt = \tau(I_0 + b) - \tau I(t) + bt \tag{4.6}$$

can be rewritten to have the decay waveform as a function of its own integral in a linear equation (Equation 4.7) and thus least- squares fitting can then be applied to determine the lifetime τ.

$$I(t) = I_0 + b - \frac{1}{\tau}\int_o^t I(t)dt + \frac{bt}{\tau} \tag{4.7}$$

When using phosphors like GGG:Cr^{3+} that are able to record temperatures over a broad temperature range, the lifetimes generally change over several orders of magnitude requiring the adaption of the detection system settings (i.e observation length Δt, trigger point t_0, etc.). Therefore, iteratively adapted fitting windows are used to avoid inaccuracies on the determination of the lifetimes.

As represented in Figure 4.15, the algorithm is related to the lifetime τ instead of Δt. The fitting window starts at $t_1 = t_0 + c_1\tau$ and ends at $t_2 = t_0 + c_2\tau$, where t_0 is the instant of the laser trigger and c_1 and c_2 are two constants. As τ is one of the unknown quantities, the fitting routine has to be applied iteratively using the initial guess $\tau_0 = c_0\Delta t$, where c_0 is a constant. For the iteration, the evaluated lifetime of the current iteration step is used for the definition of the next step's fitting window and for the new initial guess of the LRS algorithm. The convergence criterion is achieved when the difference of the maximum and the minimum τ of the last three steps is less than one thousandth of the average τ of these steps:

$$max(\tau_i, \tau_{i-1}, \tau_{i-2}) - min(\tau_i, \tau_{i-1}, \tau_{i-2}) < 10^{-3} \cdot \left[\frac{1}{3}(\tau_i + \tau_{i-1} + \tau_{i-2})\right] \tag{4.8}$$

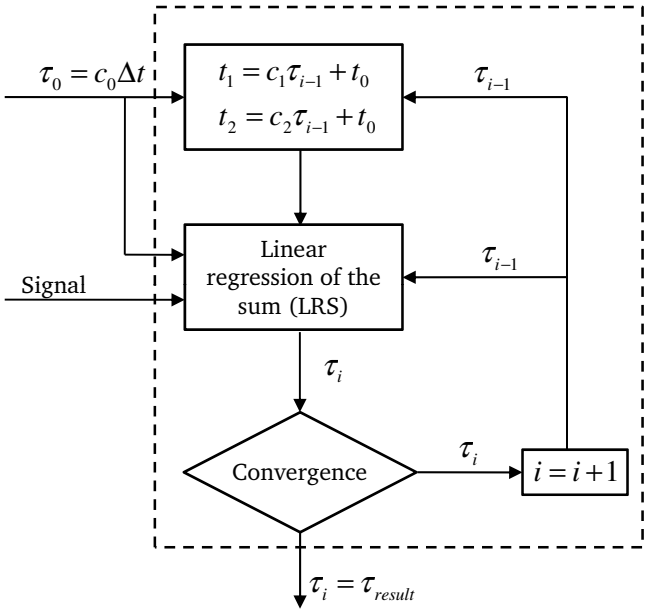

Figure 4.15: Flow chart of the algorithm using the iterative fitting window.

In the case of the the spatially resolved 2D luminescence evaluation, images acquired by the camera have been background subtracted and subsequently corrected for nonlinearity of the CMOS chip prior to the application of the iterative fitting algorithm for the temporal convolution of each pixel.

4.6 Additional experiments with GGG:Cr^{3+} powders

Experiments with GGG:Cr^{3+} powders varying the doping concentration of Cr^{3+} were performed to study the temperature-dependent luminescence characteristics. This phosphor has a potential for thermographic applications in combustion systems where temperature measurements with high spatially and temporal resolutions are required. Additionally, the effect of co-doping with Cerium (Ce), as a way to reduce the afterglow and improve the luminescence characteristics of GGG:Cr^{3+}, was also evaluated.

Five samples of GGG:Cr^{3+} with doping concentrations 0.125, 0.25, 0.5, 1, and 2 mol% of Cr (with respect to the total content of metals) and two samples of GGG:Cr,Ce (0.5 mol% Cr) co-doped with 0.038 and 0.114 % by mass Ce, respectively, were prepared following the procedure described in Section 4.1.2 with some variations. The amount of starting materials are summarized in Table 4.4. $(NH_4)_2Ce(NO_3)_6$ was used as Ce source. After drying in air at 373 K, the samples were ground, sintered in air at 1373 K for 6 hours, ball milled, sintered again in air at 1673 K for 3 hours, and ball milled again to improve the crystal structure of the powders. The crystal structure of the samples was studied and compared by XRD (see Section 4.2) while luminescence lifetimes were measured, using the setup described in Section 4.5.1, in the range from 480 to 670 K and the data were analyzed according to Section 4.5.3.

Table 4.4: Amounts of starting materials to produce the GGG:Cr and GGG:Cr,Ce powders.

Component	Amounts (g)						
	GGG:Cr (mol%)					GGG:Cr (0.5 mol%),Ce (%w)	
	0.125	0.25	0.5	1	2	0.038	0.114
$Cr(NO_3)_3{\cdot}9H_2O$	0.0080	0.0160	0.0320	0.0640	0.1281	0.0661	0.0661
Gd_2O_3	1.0875	1.0875	1.0875	1.0875	1.0875	2.1749	2.1749
Ga_2O_3	0.9372	0.9372	0.9372	0.9372	0.9372	1.8744	1.8744
$(NH_4)_2Ce(NO_3)_6$	0	0	0	0	0	0.0060	0.0180

5 Results and Discussion

This chapter presents first the results on the preparation process of the $CaTiO_3:Pr^{3+}$ and $GGG:Cr^{3+}$ targets. Next, the evaluation of the sputtering deposition of phosphor thin films is presented along with the analysis of the chemical composition and crystal structure of the thin films. Then, the luminescence characteristics of the deposited thin films of $CaTiO_3:Pr^{3+}$ and $GGG:Cr^{3+}$ are evaluated at different temperatures. Additionally, an evaluation of spatially resolved lifetime characteristics of the $GGG:Cr^{3+}$ is presented and discussed. Finally, the chapter includes the results of the effect of doping concentration on the temperature-dependent characteristics of $GGG:Cr^{3+}$ powders with and without co-doping with cerium.

5.1 Phosphor targets

The target is one of the most important component of a sputtering system since it is the source material for the film deposition. A stable sputtering target contains the components and stoichiometry desired in the film and it should have the following characteristics: (1) mechanical strength, (2) thermal strength, and (3) proper dimensions to fit in the sputtering sources. The $CaTiO_3:Pr^{3+}$ and $GGG:Cr^{3+}$ targets were prepared in the lab following the procedure detailed in section 4.1.

5.1.1 $CaTiO_3:Pr^{3+}$ target

A stable $CaTiO_3:Pr^{3+}$ target with a Pr doping concentration of 1 mol% (with respect to the Ca content) was prepared. The precursor powder was synthesised in three different batches, namely, A, B and C, to produce enough amount of material for the target. The amounts of starting materials for each batch varied slightly since the $Ti(OC_4H_9)_4$ was in liquid state, it was added first to the solution, and due to the preparation method the final amount added varied slightly. The amounts of the other starting materials were recalculated to keep the right stoichiometry. XRD measurements of the powders sintered at 873 K for 6 hours were carried out to verify that the three different batches had the same crystal structure.

Fig 5.1 presents the XRD patterns of powders samples from the three batches. As can be observed, at this temperature the powder of the three batches developed the same crystal structure. The main diffraction peaks (1 2 1), (0 4 0), (0 4 2), (2 4 2), and (1 6 1) of the orthorhombic $CaTiO_3$ standard powder diffraction file ICSD 16688 [69] can be identified in the patterns. Moreover, the intensity ratios of the main peaks are basically equal. The small differences on the relative intensities can be attributed to differences on the amounts of powder sample used for each measurement. The shape of the background corresponds to the amorphous structure of the adhesive tape employed to hold the powder samples. Background subtraction was not performed since XRD was not used in the present study for quantitative calculations.

Once verified the reproducibility of the preparation method, a total of 6.5 g of sintered precursor powder was compressed at 980 MPa, resulting in a target of 50.8 mm of diameter and 4 mm thickness with high flatness. At this step, the use of less than 6 g of powder produced targets with low mechanical strength while targets made from more than 7 g were not compressed enough, showing some cracks at the cross section, due to limitations on the maximum pressure applied (980 MPa). The target was sintered in air at 1373 K for 6 hours. The flatness of the target was maintained during this step by two flat ceramic

plates, one on the top and one on the bottom of the target. After sintering the target shrank, resulting in the stable target of 45 mm of diameter and 3 mm of thickness shown in Figure 5.2.

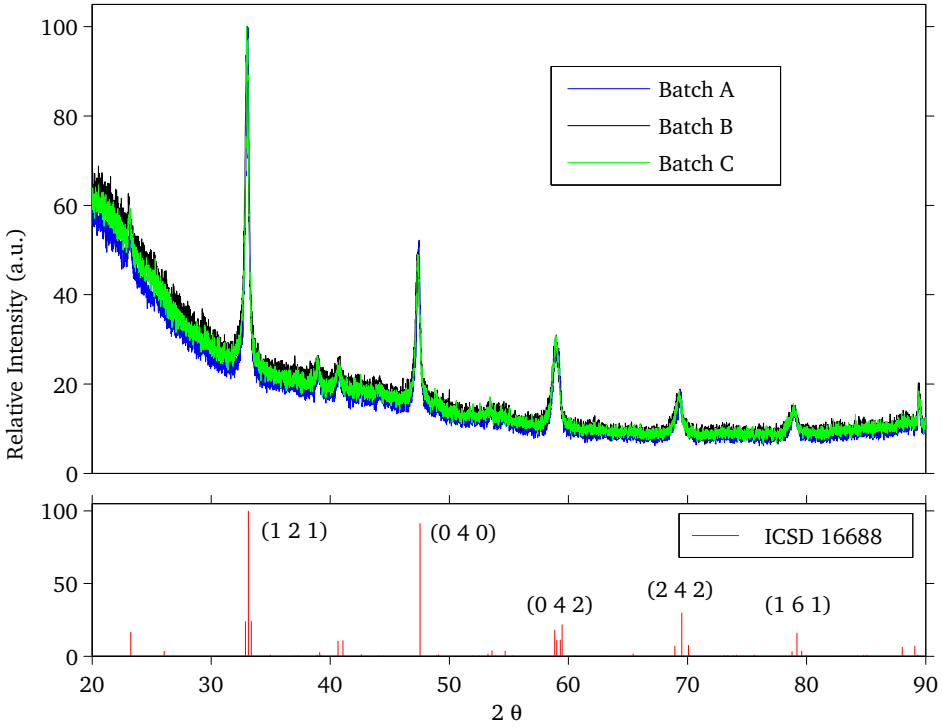

Figure 5.1: XRD patterns of the three different batches of $CaTiO_3:Pr^{3+}$ precursor powder along with the standard powder diffraction file ICSD 16688 [69].

Figure 5.2: $CaTiO_3:Pr^{3+}$ target (diameter 45 mm).

The composition and crystal structure of the $CaTiO_3:Pr^{3+}$ target was studied using XRD. The powder sample was collected by scratching the surface of the target. Figure 5.3 shows the XRD pattern of the target's sample. All the reflections of the orthorhombic $CaTiO_3$ from $2\theta = 20$ to $90°$ are present. The main peaks (1 2 1) and (0 4 0) are sharp and well-developed. The XRD result indicates that the target is single phase $CaTiO_3:Pr^{3+}$ with high crystallinity.

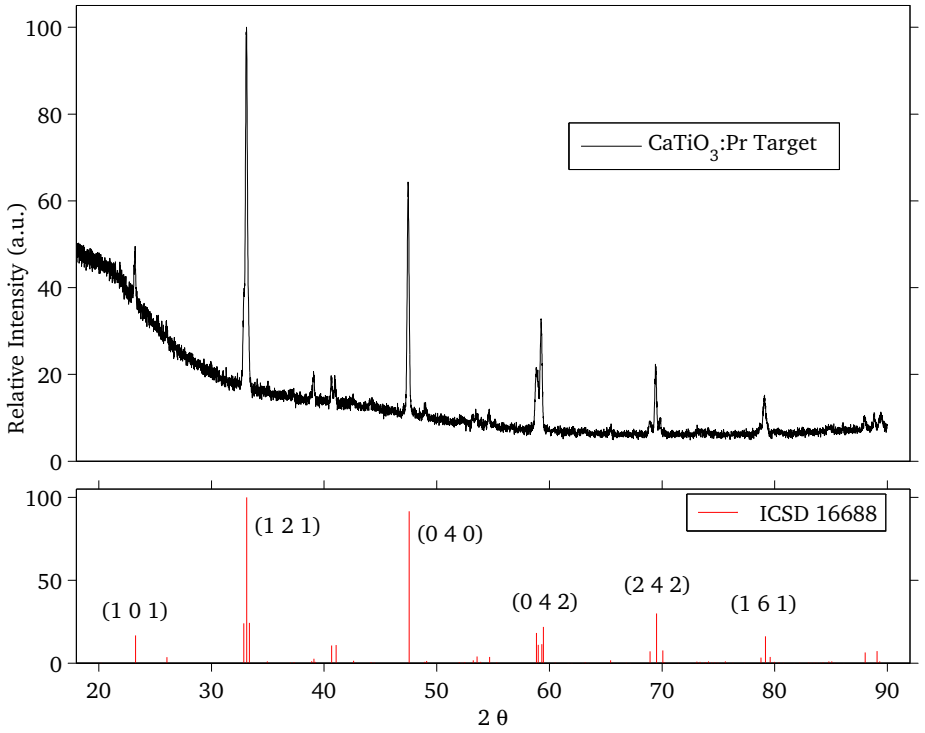

Figure 5.3: XRD pattern of the $CaTiO_3$:Pr^{3+} target along with the standard powder diffraction file ICSD 16688 [69].

5.1.2 $Gd_3Ga_5O_{12}$:Cr^{3+} target

A stable $Gd_3Ga_5O_{12}$:Cr^{3+} target, with a Cr doping concentration of 0.5 mol% (with respect to the total content of metals), was prepared. A total of 19.4 g of dried and ground powder was compressed forming a target of 50.8 mm diameter and 5 mm of thickness with high flatness. Unlike the $CaTiO_3$:Pr^{3+} target, small variations on the total amount of powder resulted in changes only in the target's thickness but not in its mechanical strength.

The sintering of the GGG:Cr^{3+} target at 1373 K is a critical step that should be performed slow to avoid damages of the target during the high temperature solid-state reactions. Sintering was performed locating the target between two flat ceramic plates to ensure the preservation of its flatness. A picture of the produced target after sintering is shown in Figure 5.4. The GGG:Cr^{3+} target slightly shrank resulting in a stable target of 49 mm of diameter and 4 mm of thickness. Although there was a small crack on the surface of the target, it did not compromise its stability.

In this case, although five individual batches were used for the preparation of GGG:Cr^{3+}, the composition and crystal structure of the target was studied by XRD only after sintering because GGG:Cr^{3+} was only formed during this step. Figure 5.5 shows the XRD pattern of the sintered target. The diffraction pattern is consistent with the cubic garnet single phase $Gd_3Ga_5O_{12}$ ICSD 9237 [70]. The main peaks (4 0 0), (4 2 0), (4 2 2), (4 4 4), (6 4 0) and (6 4 2) are sharp and well-developed, and all the reflections with lower intensities can be easily identified. However, small traces of a second phase of Gd_3GaO_6 were detected as indicated by the red circle in the pattern. The presence of this second phase is due to the limitation of the sintering temperature to 1373 K. However, it is expected that this impurity does not affect the luminescence properties of the material [71].

Figure 5.4: $Gd_3Ga_5O_{12}:Cr^{3+}$ target (diameter 49 mm).

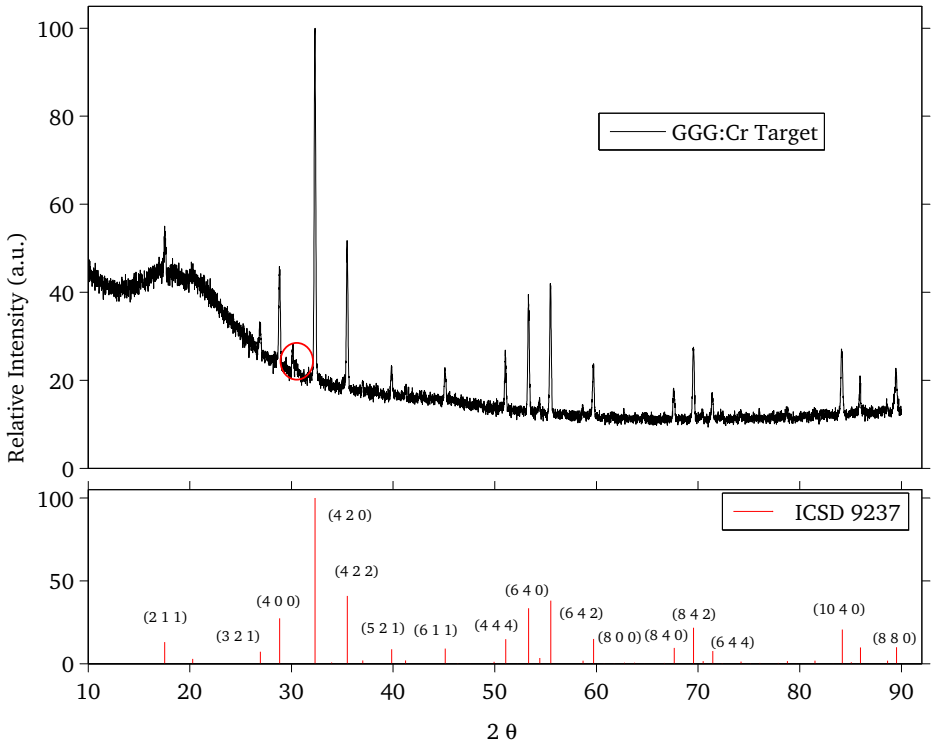

Figure 5.5: XRD pattern of the $Gd_3Ga_5O_{12}:Cr^{3+}$ target along with the standard powder diffraction file ICSD 9237 [70].

5.2 Thin films of thermographic phosphors

Thin films of $CaTiO_3:Pr^{3+}$ and $GGG:Cr^{3+}$ were deposited by RF magnetron sputtering using the parameters of Table 4.3. The deposition was attempted first using only Argon as sputtering gas. However, after several hours of sputtering, both targets revealed a dark layer. For the $CaTiO_3:Pr^{3+}$ target, the layer could be a result of reduction of the Pr from Pr^{3+} to Pr^{2+} at the outer coat of the target due to the low partial pressure of O_2 inside of the sputtering chamber. In the case of the $GGG:Cr^{3+}$ target, the reason of the formation of the dark layer is not clear. To overcome this, a small amount of oxygen was mixed with the sputtering gas. The addition of 5% O_2 prevented any change on the oxidation state of both

targets. Additionally, it is unlikely to completely sputter metal oxide targets in a molecular form, hence the deposited films tend to be deficient in gaseous species [63]. Therefore, O_2 was also used to fully oxidize the sputtered films restoring their stoichiometry. The ratio of oxygen in the sputtering gas was low enough to prevent reduction on the deposition rate [72].

Prior to the experiments, the RF power was optimized to increase the deposition rate without destroying the targets or their bondings. For each target, the plasma was ignited at 5 W and slowly increased in steps of 5 W. The deposition rate was monitored with the sensor installed inside the sputtering chamber. For the Z factor (Equation 4.4), density values of 3.98 and 7.10 g/cm^3 and shear modulus values of 105.4 and 88 GPa were used for $CaTiO_3$ and $Gd_3Ga_5O_{12}$ [73, 74], respectively. The $CaTiO_3$:Pr^{3+} target started to reveal some superficial cracks at powers higher than 100 W while 60 W was determined as the limit for the GGG:Cr^{3+} target. At these conditions, deposition rates of 72 and 26 nm/h were estimated for $CaTiO_3$:Pr^{3+} and GGG:Cr^{3+}, respectively. These values are considerable low in comparison to those reported in the literature for sputtering of thermographic phosphors [23, 24, 50, 52].

Another important parameter of the sputtering deposition is the temperature of the substrate. Temperatures of 623 and 723 K were set for the substrates during the experiments of $CaTiO_3$:Pr^{3+} and GGG:Cr^{3+}, respectively, to enhance the mobility of the sputtered atoms arriving to the surface and thus increasing their opportunity of finding low energy positions in the growing film. However, higher temperatures were not used because the deposition rate could be reduced as the temperature increases due to re-evaporation or re-sputtering of the atoms from the substrate [72].

Depositions were conducted during 15 hours for $CaTiO_3$:Pr^{3+} and during 40 hours in the case of GGG:Cr^{3+} to compensate the low deposition rates, expecting to produce films with thicknesses of $\sim$1 μm. Measurements with the profilometer determined mean thicknesses of 500 nm and 1.1 μm for the deposited films of $CaTiO_3$:Pr^{3+} on ITO/glass and GGG:Cr^{3+} on quartz glass, respectively. This means that the actual deposition rates were 33.3 nm/h for $CaTiO_3$:Pr^{3+} and 27.5 nm/h for GGG:Cr^{3+}. The disagreement between the expected and the actual deposition rates in the case of $CaTiO_3$:Pr^{3+} could have two possible reasons: (1) the deposition rate monitor is not suitable for $CaTiO_3$:Pr^{3+} with the current parameters and/or (2) the re-evaporation of deposited atoms was higher than expected because the deposition was performed at high temperature and the measurements with the deposition rate monitor were performed a room temperature. However, despite the high sputtering times, low deposition rates combined with high temperature of the substrates are expected to lead to large grains, a low density of crystal defects and large continuity of the films [63].

5.2.1 Chemical composition of the sputtered films

The chemical composition of the sputtered films was studied using XPS. The spectra were compared with standards from a database [66] to identify the components of the films. Figure 5.6 presents the XPS spectrum of the $CaTiO_3$:Pr^{3+} thin film. The photoelectron lines corresponding to electrons from the orbitals Ca2p$_{1/2}$ (351 eV), Ca2p$_{3/2}$ (347 eV), Ca2s (440 eV), Ti2p$_{1/2}$ (460 eV), Ti2p$_{3/2}$ (454 eV), Ti2s (561 eV) and O1s (531 eV) could be easily identified. The Auger lines Ca LMM, Ti LMM, and O KLL were also evident at the high binding energy region. The photoelectron peaks near the Fermi level are overlaps of the O2s, Ca3s, Ca3p, Ti3s, and Ti3p lines. Pr^{3+} could not be detected by XPS due to its low concentration. Additionally, the peak of C1s (284 eV) was also identified which is representative of hydrocarbon impurities from air present in the outer layers of the film.

Figure 5.7 presents the XPS spectrum of the GGG:Cr^{3+} thin film. The photoelectron lines of the gadolinium atom Gd3d$_{3/2}$ (1218 eV), Gd3d$_{5/2}$ (1186 eV), split Gd4p (1/2 at 291 eV and 3/2 at 272 eV), and Gd4d (140 eV), the gallium atom Ga2p$_{1/2}$ (1144 eV), Ga2p$_{3/2}$ (1117 eV), Ga3s (160 eV), Ga3s (160 eV),

split Ga3p (1/2 at 107 eV and 3/2 at 104 eV) and the oxygen atom O1s (531 eV) were distinguished. The Auger peaks O KLL Gd MNN and Ga LMM were identified at the positions corresponding to $Al_{k\alpha}$ excitation. The peaks at low binding energies correspond to overlapped lines of photoelectrons from the outer orbitals O2s, Ga3d, Gd5s, Gd5p and Gd4f. In this case the common carbon line C1s (284 eV) was not present because the surface of the sample was cleaned by sputtering the film during few minutes. Again, photoemission lines from the doping atoms Cr^{3+} could not be detected by XPS due to its low concentration in the film.

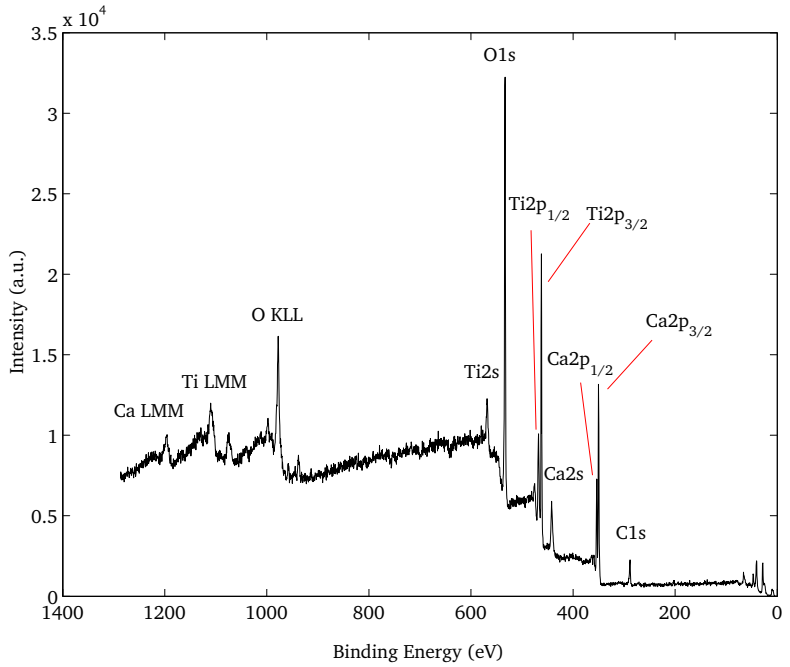

Figure 5.6: XPS spectrum of the $CaTiO_3$:Pr^{3+} thin film as-deposited.

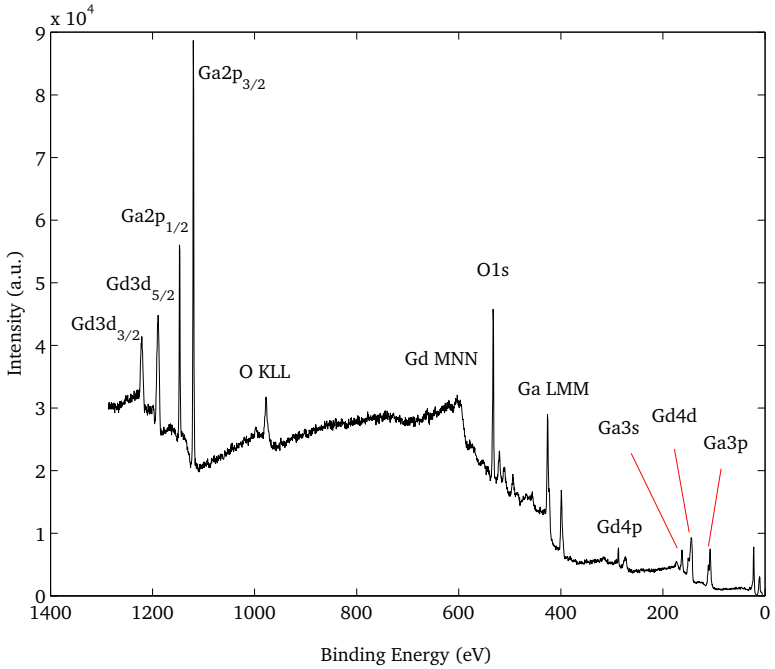

Figure 5.7: XPS spectrum of the $Gd_3Ga_5O_{12}$:Cr^{3+} thin film as-deposited.

The XPS spectra revealed the presence of all the atoms of the host materials in the films (i.e $CaTiO_3$, $Gd_3Ga_5O_{12}$). Additionally, a semiquantitave analysis, based on the peak area sensitivity factors method [66, 75], was carried out using the software CasaXPS [76] to estimate the relative concentration of the atoms detected in the films. For this purpose, detailed scans of the lines Ca2p, Ti2p and O1s for the $CaTiO_3$:Pr^{3+} film and $Ga2p_{3/2}$, Gd3d and O1S in the case of the GGG:Cr^{3+} film were used. For the $CaTiO_3$:Pr^{3+} film the analysis provided relative atomic concentrations of 20.2% Ca, 19.8% Ti, and 60% O while for the GGG:Cr^{3+} film the relative concentrations are 15.7% Gd, 27.8%Ga, and 56.5% O. Although these values are in good agreement with the stoichiometric relative concentrations, XPS semiquantitative analysis should be handled with care. Uncertainties could be as high as 20% due to the known limitations of XPS such as interferences and overlaps of peaks, background calculation of doublet lines, and shifting of binding energies [66, 75]. Moreover, since the Fermi level of insulating materials lies in a relative large gap (∼10 eV) between the conduction and valence bands, the binding energies shifts could be even larger in this case. Therefore, in this study the XPS semiquantative analysis was only used as an indicator of the approximate stoichiometry of the deposited films.

5.2.2 Crystal structure of the sputtered films

After deposition, both films did not show any luminescence signal regardless of the sputtering condition and therefore they were annealed. The $CaTiO_3$:Pr^{3+} film was annealed in vacuum at 973 K during 4 hours according to conditions reported by Chung *et al.* [52]. For the GGG:Cr^{3+} film, the annealing conditions for $Y_3Al_5O_{12}$:Ce films, reported by Chao *et al.* [72], were used as reference because YAG and GGG have identical crystal structures. The GGG:Cr^{3+} film was annealed at 1173 K for 12 hours in N_2 atmosphere and at atmospheric pressure to avoid the oxidation of the stainless steel substrate or of the dopant atoms. The crystal structure of the sputtered thin films was studied by XRD, before and after heat treatment.

Figure 5.8 presents the XRD patterns of the $CaTiO_3$:Pr^{3+} thin film as-deposited and annealed. The XRD pattern of one sample of stainless steel without annealing has been also included to facilitate the identification of the peaks. The small thickness of the $CaTiO_3$:Pr^{3+} film increased the path length of the X-rays in the substrate resulting in strong reflections from the stainless steel in the XRD patterns as can be seen in Figure 5.8. The strong reflection of the substrate at $2\theta = 43°$ is not completely included to facilitate the analysis. The XRD patterns reveal that the crystallization of the film started during the sputtering, likely due to the temperature of the substrate. After annealing, the crystallinity of the film corresponds to the single phase of $CaTiO_3$ and the reflections of the (1 2 1), (0 4 0), (0 4 2) and (2 4 2) planes can be identified in the pattern. However, although the film is single-phase the reflections are not very sharp suggesting poor crystallinity. The reflections from XRD measurements using the thin film geometry are broader and a little bit shifted in comparison to those obtained with the Debye-Scherrer geometry for powder samples.

Figures 5.9 and 5.10 present the XRD patterns of the GGG:Cr^{3+} film as-deposited and annealed. A sample of stainless steel substrate was annealed and analyzed by XRD to identify changes in its diffraction pattern due to the high temperature of the annealing process. The XRD patterns of the stainless steel substrate before and after annealing are included as references in Figures 5.9 and 5.10, respectively. As can be seen in Figure 5.9, after deposition at 723 K, the GGG:Cr^{3+} film is completely amorphous and all the reflections in the pattern correspond to the substrate. However after annealing, the crystal structure of the film is restored and the main peaks of the cubic $Gd_3Ga_5O_{12}$ are observed. In this case, the reflections from the GGG:Cr^{3+} film are stronger than those from the substrate probably due to the larger thickness of the film. All the peaks were identified to belong either to the $Gd_3Ga_5O_{12}$ or the substrate structures. It was not possible to determine if the second phase of Gd_3GaO_6 is also present in the film because of a strong reflection from the substrate around $2\theta = 30°$.

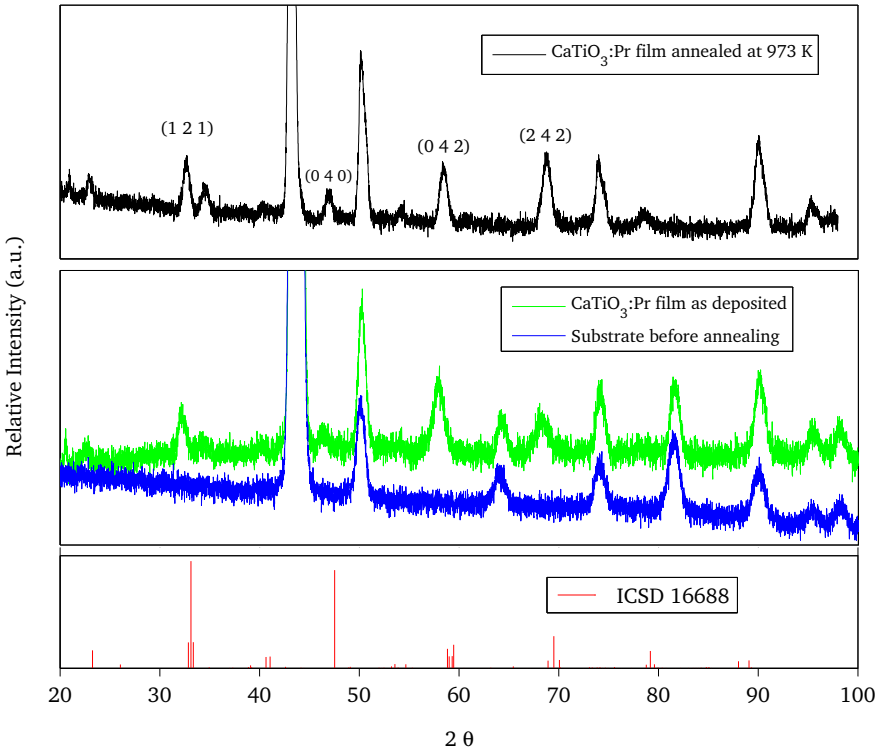

Figure 5.8: XRD patterns of the $CaTiO_3:Pr^{3+}$ thin film as-deposited and annealed at 973K along with the pattern of the stainless steel substrate before annealing and the standard powder diffraction file ICSD 16688 [69].

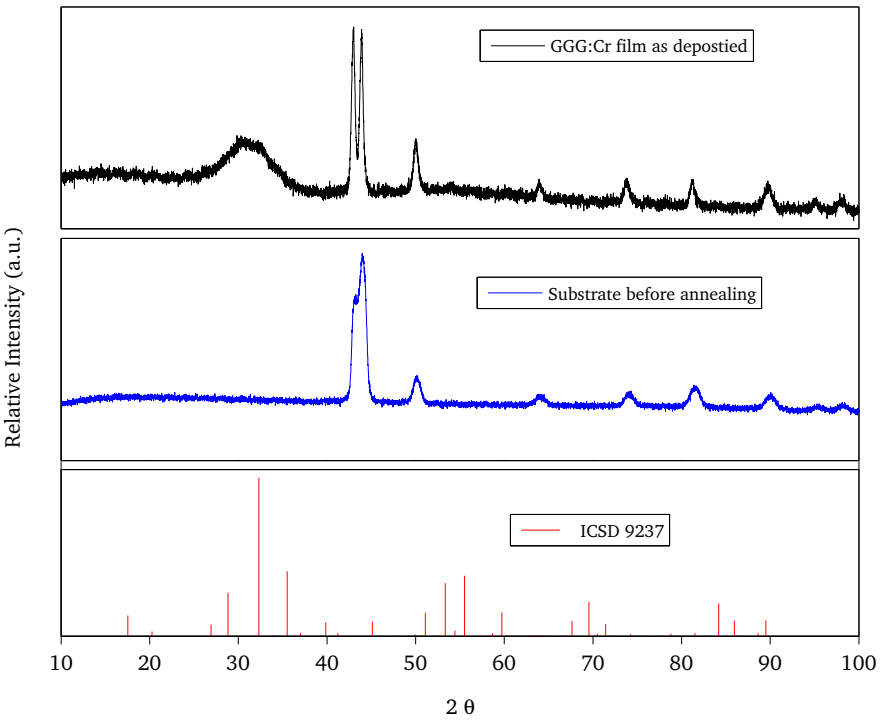

Figure 5.9: XRD patterns of the $GGG:Cr^{3+}$ as-deposited along with the pattern of the stainless steel substrate before annealing and the standard powder diffraction file ICSD 9237 [70].

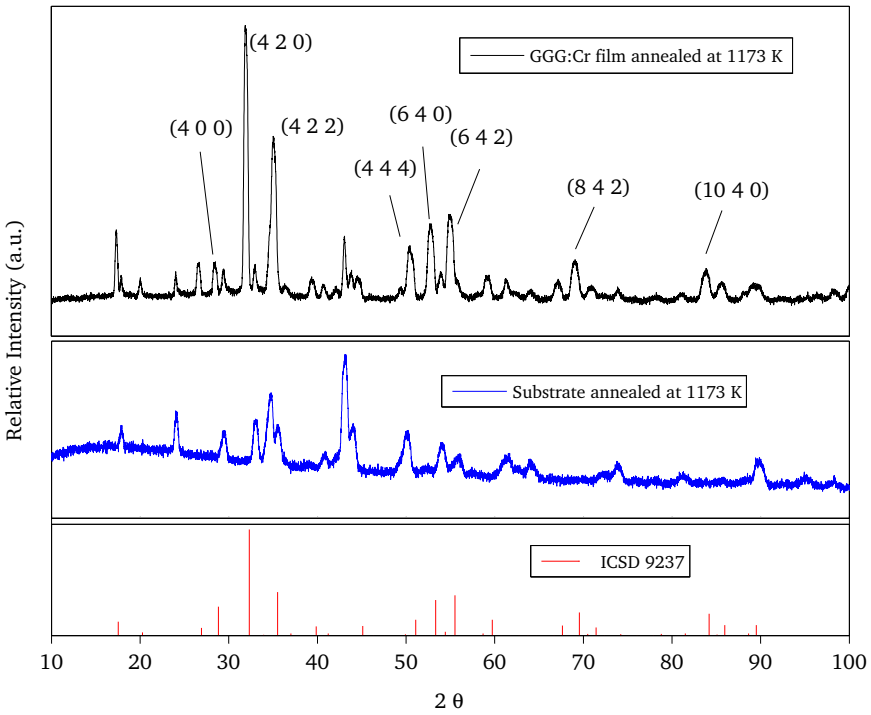

Figure 5.10: XRD patterns of the GGG:Cr^{3+} film along with the stainless steel substrate annealed at 1173 K and the standard powder diffraction file ICSD 9237 [70].

After deposition, the dopant atoms are situated in a variety of positions and rotations within the crystal structure of the host [24]. The Pr^{3+} and Cr^{3+}, therefore, experienced a variety of crystal field effects, which lead to weak or non- luminescent emission. The annealing process enabled the restoration of the crystal structure of the host material as well as the correct re-position of the dopant atoms within the host lattice. This resulted in improvements in coupling of the excitation energy and the electrons, restoring the luminescent properties. The XRD results of the stainless steel substrate suggest a re-crystallization of its structure during the annealing at high temperatures without any phase change.

5.3 Luminescence characteristics of the thin films

5.3.1 Luminescence emission spectra

The emission spectra of the thin films could not be recorded with the available spectrometer because the emission intensities were lower than the intensity of the background light. Nevertheless, the emission spectra of the $CaTiO_3$:Pr^{3+} and GGG:Cr^{3+} targets were measured at room temperature, averaged over 100 single-shots of the laser. They are presented in Figures 5.11 and 5.12, respectively. The $CaTiO_3$:Pr^{3+} spectrum shows a prominent branch between 580 and 650 nm with a maximum at approximately 615 nm, which corresponds to the $^1D_2 \rightarrow {}^3H_4$ transition. This result corresponds very well with previous studies [52, 77]. The GGG:Cr^{3+} spectrum reveals a prominent branch from 650 to 850 nm (end of the spectral range of the spectrometer) peaking at ∼730 nm, which corresponds mainly to the the $^4T_2 \rightarrow {}^4A_2$ transition. This spectrum is in good agreement with previous reports of GGG:Cr^{3+} [9, 78]. Additionally, the GGG:Cr^{3+} spectrum exhibited a sharp peak feature at ∼700 nm due to the R-line emission $^2E \rightarrow {}^4A_2$ [62].

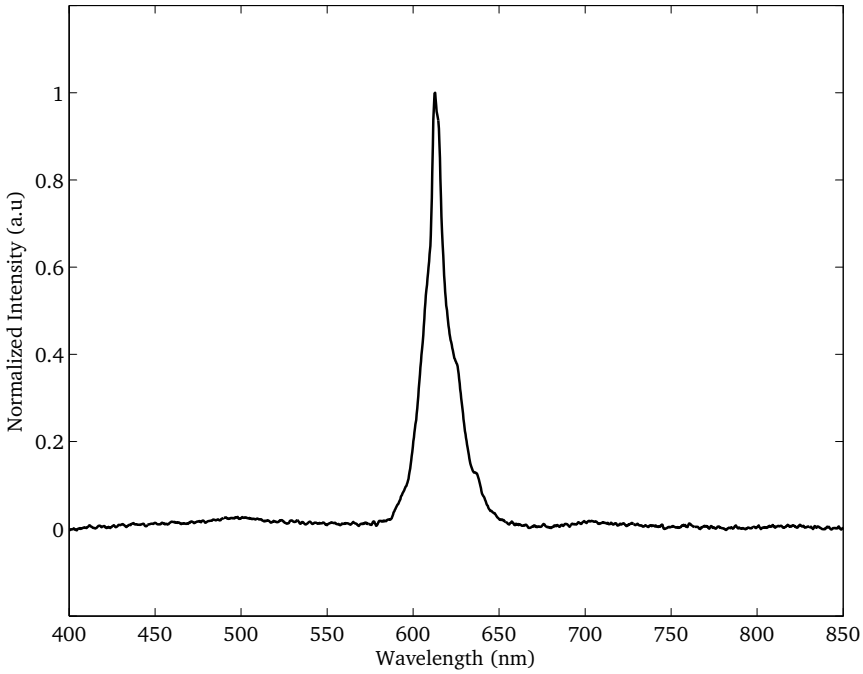

Figure 5.11: Emission spectrum of the $CaTiO_3$:Pr^{3+} target at room temperature.

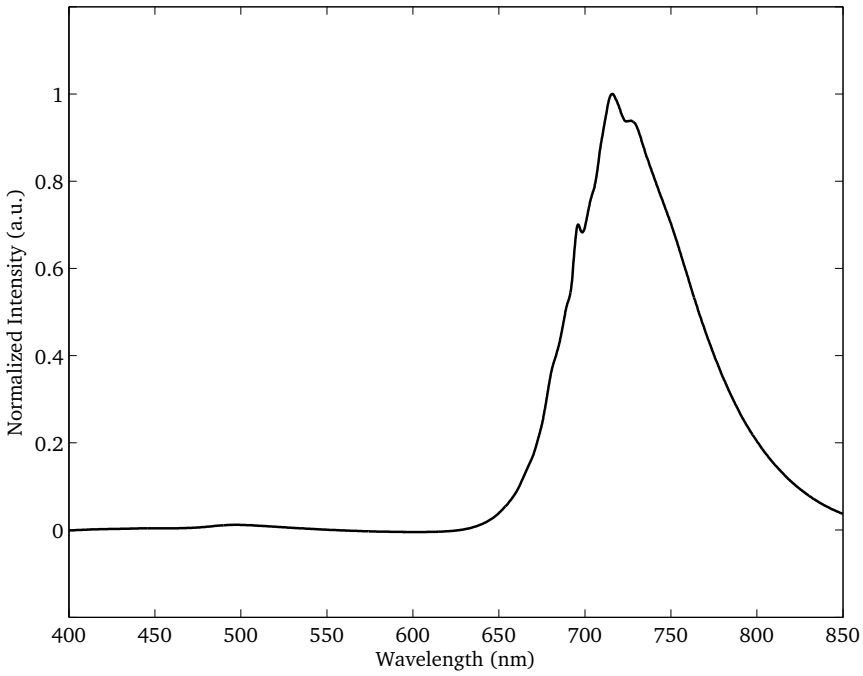

Figure 5.12: Emission spectrum of the GGG:Cr^{3+} target at room temperature.

5.3.2 Temperature-dependent luminescence characteristics

Figure 5.13 presents the temperature-lifetime characteristic for the $CaTiO_3$:Pr^{3+} thin film deposited on the stainless steel substrate. Brübach *et al.* [77] measured the temperature-lifetime characteristic of a $CaTiO_3$:Pr^{3+} powder sample with the same Pr^{3+} doping concentration as of the present study and their results are also included in Figure 5.13. The calibration curve of the film shows a fairly linear behavior in the semilogarithmic plot. The lifetime starts from 1.55×10^{-6} s at 310 K and decreases down to 4.60×10^{-7} at 500 K. The parameters $c_1 = 0.3$ and $c_2 = 1.4$ were used for the iterative fitting window algorithm. It was not possible to fit values of the lifetime at temperatures higher than 500 K due to low signal-to-noise ratio. Although, the lifetime of the thin film has a sensitivity in the observed temperature range, it is comparatively low with respect to the previous studies on $CaTiO_3$:Pr^{3+} powders [77]. Differences in the setups for the signal collection could explain the differences between the film and the powder results, as stated below.

The luminescence signal in [77] was measured using an interference filter at 610 nm and it was temporally resolved with an input resistance of 50 Ω. However, in the present study, when the decay waveforms were collected with 50 Ω and with a 610 nm filter, the signals were almost lost due to the weak emission from the film. The use of a higher resistance (500 Ω) could contribute to the attenuation of the calibration curve due to the cutoff frequency effect. On the other hand, when the measurements are carried out without an interference filter, light from different wavelengths could affect the decay waveform and therefore the lifetime values.

However, since it is unlikely to obtain exactly the same stoichiometric in the film as in the target when using sputtering [63], the film could have a different doping concentration and therefore different luminescence characteristics, which could also contribute to the difference in lifetimes of the film and the powder. Unfortunately, the determination of the Pr^{3+} doping concentration in the film was beyond the aims of the present study.

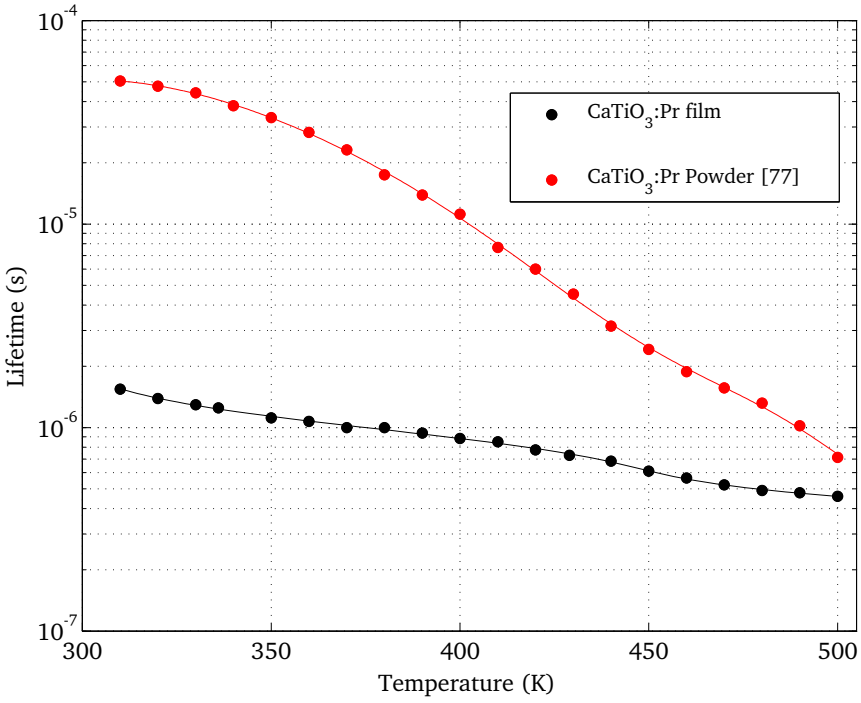

Figure 5.13: Temperature-lifetime characteristic of the $CaTiO_3$:Pr^{3+} film.

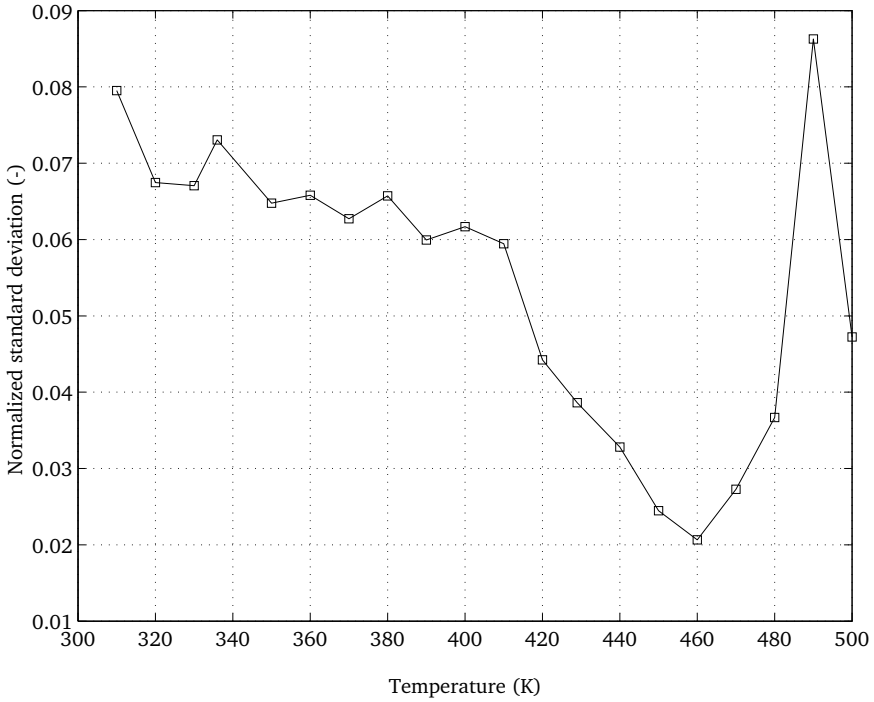

Figure 5.14: Normalized shot-to-shot standard deviation in terms of temperature for the $CaTiO_3:Pr^{3+}$ film.

There are different ways to characterize precision. In fact, a rigorous evaluation of precision implies different statistical test that are beyond the scope of this study. However, a first-order approach to evaluate the precision of the measurement can be attempted determining the normalized shot-to-shot standard deviation of the single-shot temperatures according to Equation 5.1 and plotted in Figure 5.14.

$$\frac{\sqrt{\frac{1}{N_s-1}\sum_{s=1}^{N_s}\left(T_s-\frac{1}{N_s}\sum_{s=1}^{N_s}T_s\right)^2}}{\frac{1}{N_s}\sum_{s=1}^{N_s}T_s} \tag{5.1}$$

where s and N_s are the index and number of the single shots (200 in the case of $CaTiO_3:Pr^{3+}$ film), respectively and T is the temperature.

As can be seen in Figure 5.14 the standard deviation starts from 8% at 310 K, decreases down to 2% at 460 K and rapidly increases again above 470 K due to the low signal-to-noise ratio and the low temperature sensitivity. The precision of the lifetime measurements with the $CaTiO_3:Pr^{3+}$ film is considerably low compared to thermometry systems with similar configuration [29]. The $CaTiO_3:Pr^{3+}$ coating was stable on the substrate after the laser measurements at the temperature range used. Improvements such as the increase of the film thickness and the enhancement of the crystal structure are suggested to improve the signal-to-noise ratio and thus the precision of surface temperature measurements using a $CaTiO_3:Pr^{3+}$ thin film.

Figure 5.15 shows the temperature-lifetime characteristic for the $GGG:Cr^{3+}$ thin film deposited on the stainless steel substrate in the range between 310 and 1000 K. In this case, lifetime measurements of the $GGG:Cr^{3+}$ target were carried out, in the same temperature range as for the film, to compare the luminescence properties of the source material and the thin film. The results are also included in Figure 5.15. Both calibration curves show piecewise linear shapes in the semilogarithmic plot, with reasonable differences between 600 and 800 K. The corresponding lifetimes start at 2.00×10^{-4} and 1.77×10^{-4}

at 310 K and decrease to 2.50×10^{-7} and 2.29×10^{-7} at 1000 K for the thin film and the target, respectively. The parameters $c_1 = 0.5$ and $c_2 = 3.5$ for the iterative fitting window algorithm yielded good results in terms of precision. The temperature sensitivities of the lifetimes are similar to those reported for a GGG:Cr^{3+} coating applied by air-brush on a stainless steel substrate [9], which were measured with similar setup and parameters as of the present study. The differences between the thin film and the target could be due to the inherent change in the stoichiometric (i.e. in the Cr^{3+} doping concentration) during the sputtering deposition.

The normalized shot-to-shot standard deviations of the single-shot temperatures calculated with Equation 5.1 (with $N_s = 100$ shots) are presented in Figure 5.16. The GGG:Cr^{3+} thin film provides standard deviations below 0.65% for the whole temperature range resulting in a high precision of the same order as the previous study of Fuhrmann *et al.* [9] for a thick GGG:Cr^{3+} coating (~10 μm). The target's precision behavior is similar, with an increase in standard deviations above 930 K. The variation of the precision at high temperatures could be related with two effects: (1) at short lifetimes, the trigger has a major disturbing influence on the decay waveform, decreasing the signal-to-noise ratio; (2) The the low-pass characteristics (cut-off frequency) of the detection system decrease the sensitivity at high temperatures, affecting the precision.

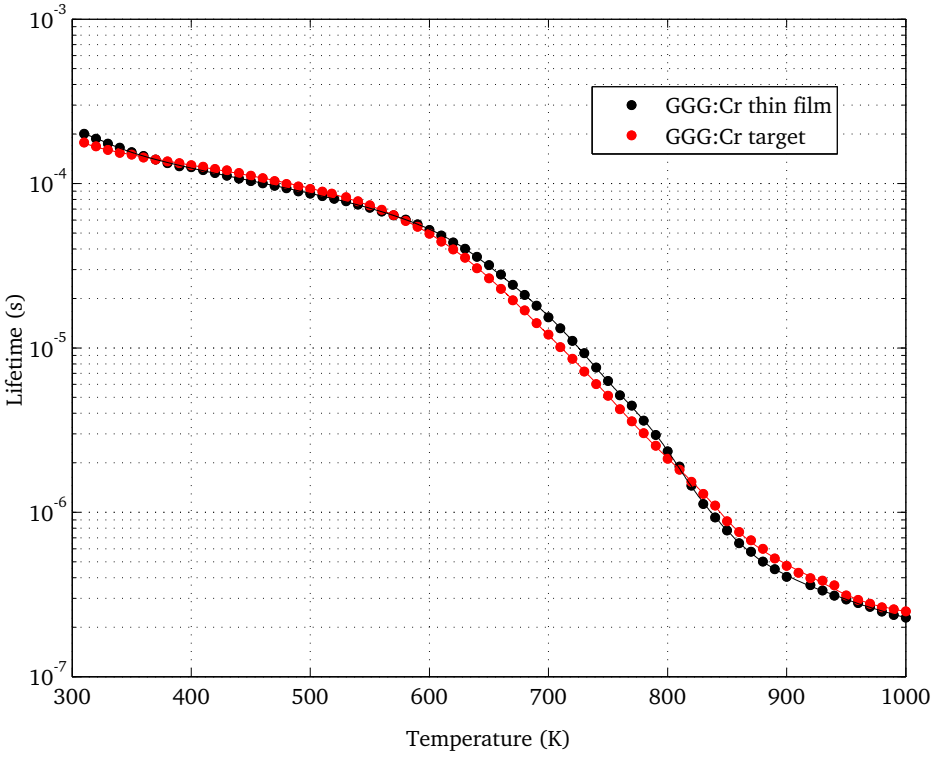

Figure 5.15: Temperature-lifetime characteristics of the GGG:Cr^{3+} film and target.

The results of temperature sensitivity and precision prove the feasibility of high-precision zero-dimensional single-shot temperature measurements using a thin film of GGG:Cr^{3+} in the range from 310 to 1000 K and its the most important result of this research. The GGG:Cr^{3+} coating was stable on the substrate after the laser measurements at different temperatures. However, because of the differences on the lifetimes of the film and the source material (target) can result in temperature differences as high as 20 K, it is recommended to construct calibration curves for every coating produced by sputtering deposition.

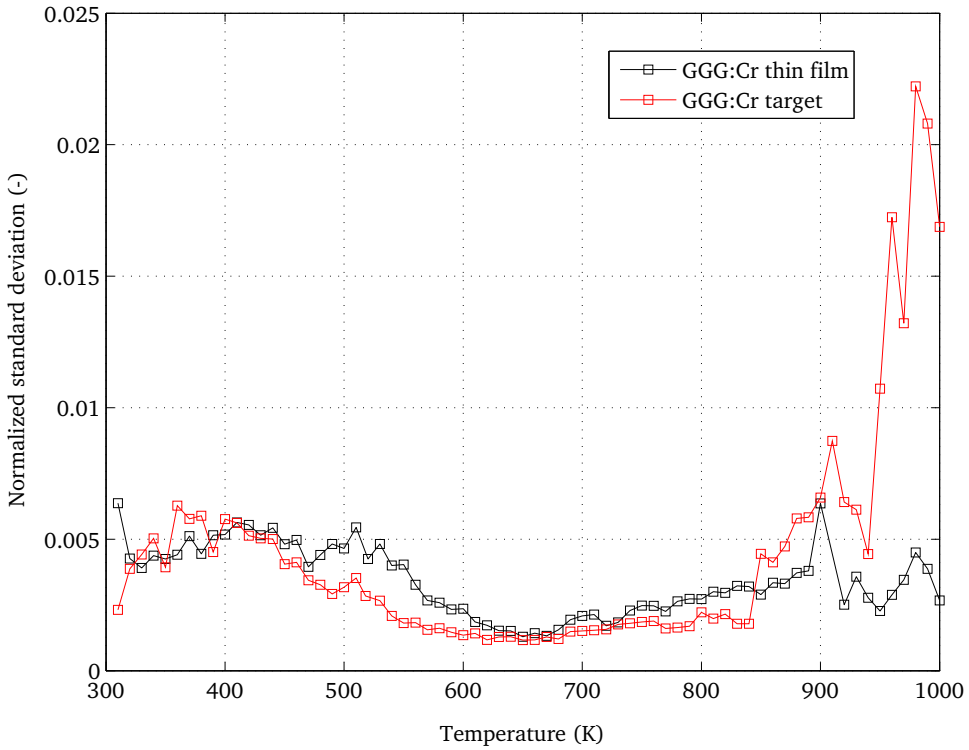

Figure 5.16: Normalized shot-to-shot standard deviations in terms of temperature for the GGG:Cr^{3+} film and target.

5.3.3 Spatially resolved lifetime characteristics

Two-dimensional luminescence lifetime measurements of the GGG:Cr^{3+} film were performed at room temperature (293 K) to evaluate the spatial homogeneity of the luminescence characteristics of the deposited films. This measurement was not possible with the $CaTiO_3$:Pr^{3+} film due to its low emission intensity. Although, it is beyond the original scope of this thesis, this analysis increases the understanding of the characteristics of the phosphor thin films produced by sputtering. In this way, opportunities for future studies can be identified.

Figure 5.17 presents the two-dimensional spatial distribution of the lifetime of the GGG:Cr^{3+} film at room temperature. The non-uniformities at the edges of the coating result from the "shadow" generated by the thickness of the substrate holder during the sputtering process. Clear spatial inhomogeneities of the luminescence lifetime of the GGG:Cr^{3+} film are observed. As quantified in Figure 5.18, there is a relative broad distribution of lifetimes in the film. At room temperature, a difference of 1×10^{-5} s in lifetime results in a ΔT of $\sim$10 K. Therefore, it could be considered that the film has a relative poor spatial homogeneity of luminescence properties.

Figure 5.19 displays the initial intensity of the luminescence emission of the GGG:Cr^{3+} film at 293 K. The inhomogeneities on intensity could be due to non-uniformities of the laser beam profile, inhomogeneities of the film thickness, or any other physical defects of the film. However, this does not explain the spatial inhomogeneity of the luminescence lifetime as similar patterns between Figures 5.17 and 5.19 can not be identified when comparing both figures. As a consequence, local differences in doping concentration could be the reason for such an inhomogeneity on lifetimes. From the sputtering process it is unlike to obtain such a random distribution of Cr^{3+} atoms [63]. However, during the annealing process, local differences in the crystallinity of the film, due to temperature gradients, and/or Cr diffusion from the

stainless steel substrate, due to the high temperature, could explain the luminescence characteristics of the film.

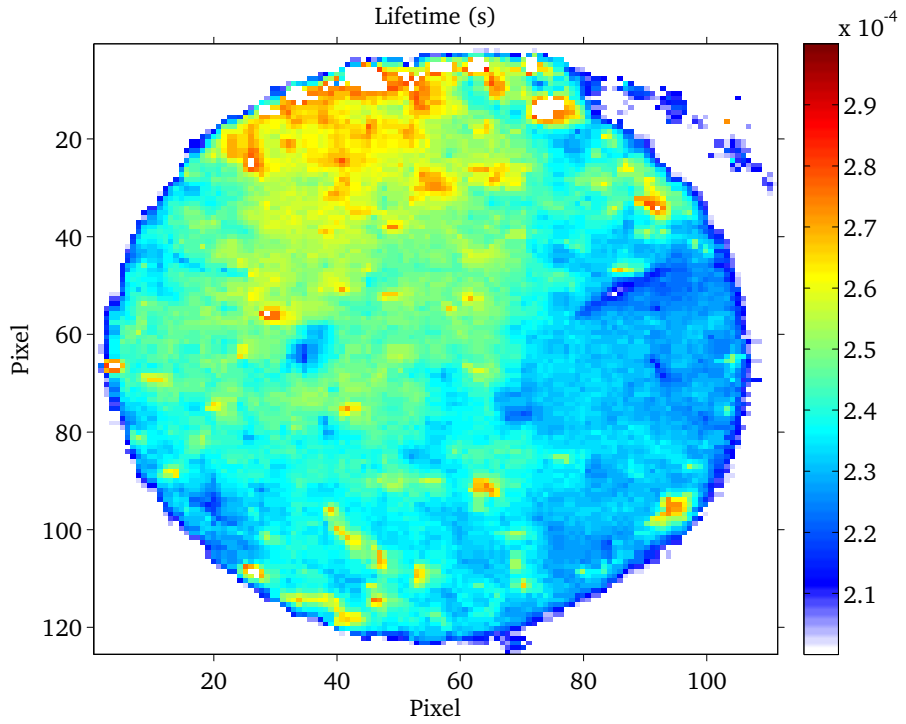

Figure 5.17: 2D luminescence lifetime of the GGG:Cr^{3+} film at room temperature.

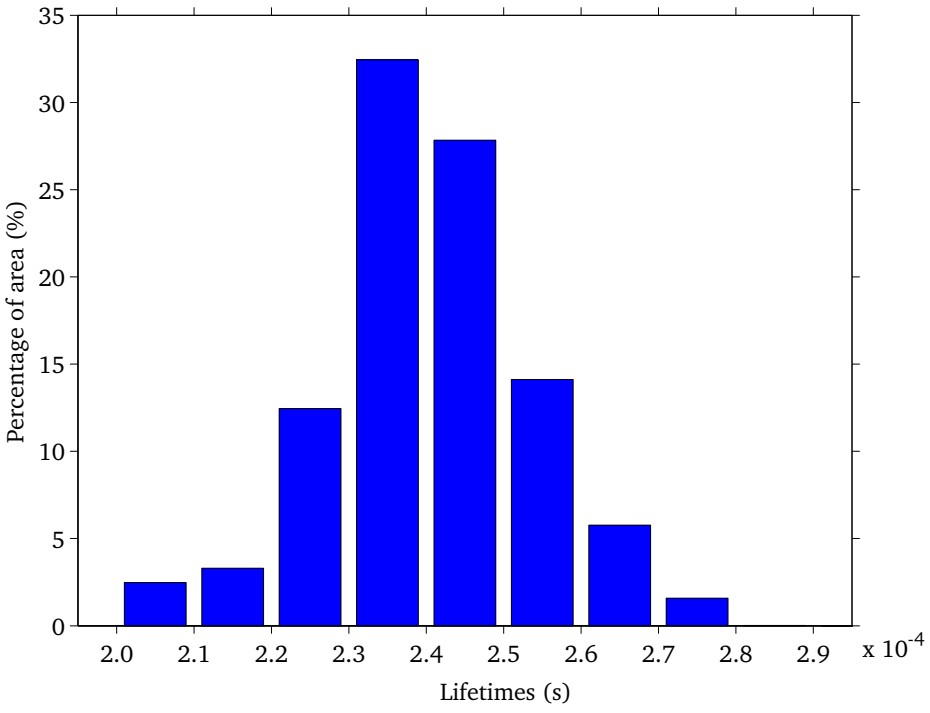

Figure 5.18: Distribution of lifetimes in the GGG:Cr^{3+} film at room temperature.

The sputtering deposition of films with larger thicknesses, the increase of the maximum temperature of the annealing, and the coating of substrates without Cr content are suggested for future studies on GGG:Cr^{3+} thin films. Additionally, studies of the morphology of the films by scanning electron microscopy (SEM) or atomic force spectroscopy (AFM) and the use of surface characterization techniques that allow measuring local doping concentrations such as Rutherford backscattering spectroscopy (RBS) or particle-induced X-ray emission spectrometry (PIXE) are highly recommended.

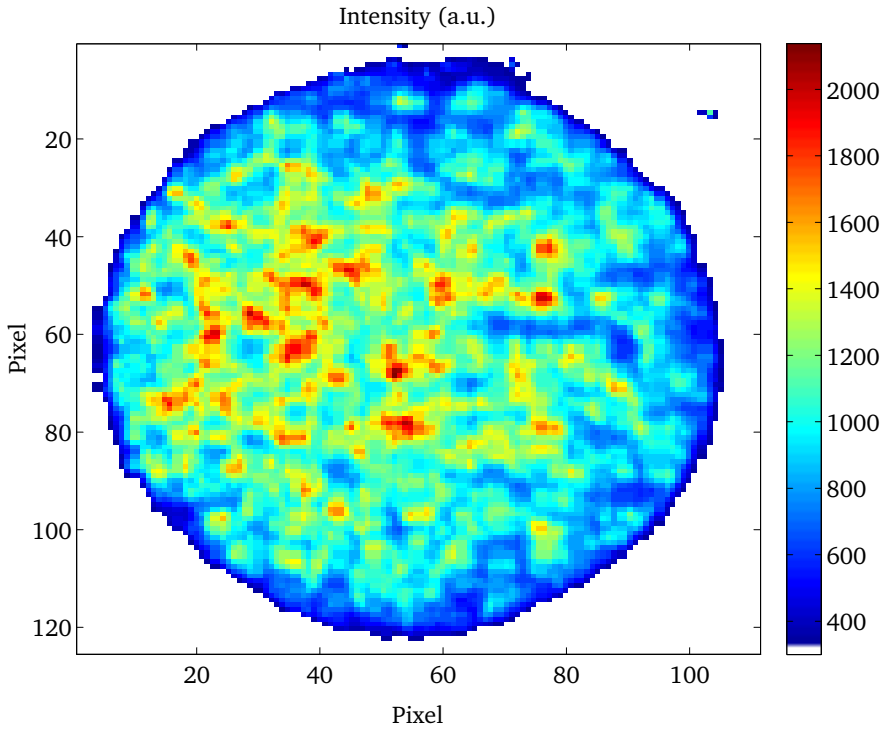

Figure 5.19: Initial intensity distribution of luminescence emission from the GGG:Cr^{3+} film at room temperature.

5.4 Results on GGG:Cr^{3+} powders

5.4.1 Crystal structures

As in 5.3.3, this section is beyond the scope of the thesis, however it is presented intending to improve the insight on the luminescence properties of the GGG:Cr^{3+} phosphor. Figure 5.20 shows the XRD patterns of the GGG:Cr^{3+} powders with different doping concentrations and co-doped with Ce as a way to reduce the afterglow. The diffraction patterns are consistent with the cubic garnet single phase $Gd_3Ga_5O_{12}$ ICSD 9237 [70]. All the reflections in the range $10° < 2\theta < 90°$ are sharper and more developed than those from the GGG:Cr^{3+} target (Figure 5.5). Variations in background are due to differences on the amount of powder used for each sample. The second phase of Gd_3GaO_6 is not present in any of the patterns. This means that the sintering of the powders up to 1673 K yields single phase GGG:Cr^{3+} with high crystallinity.

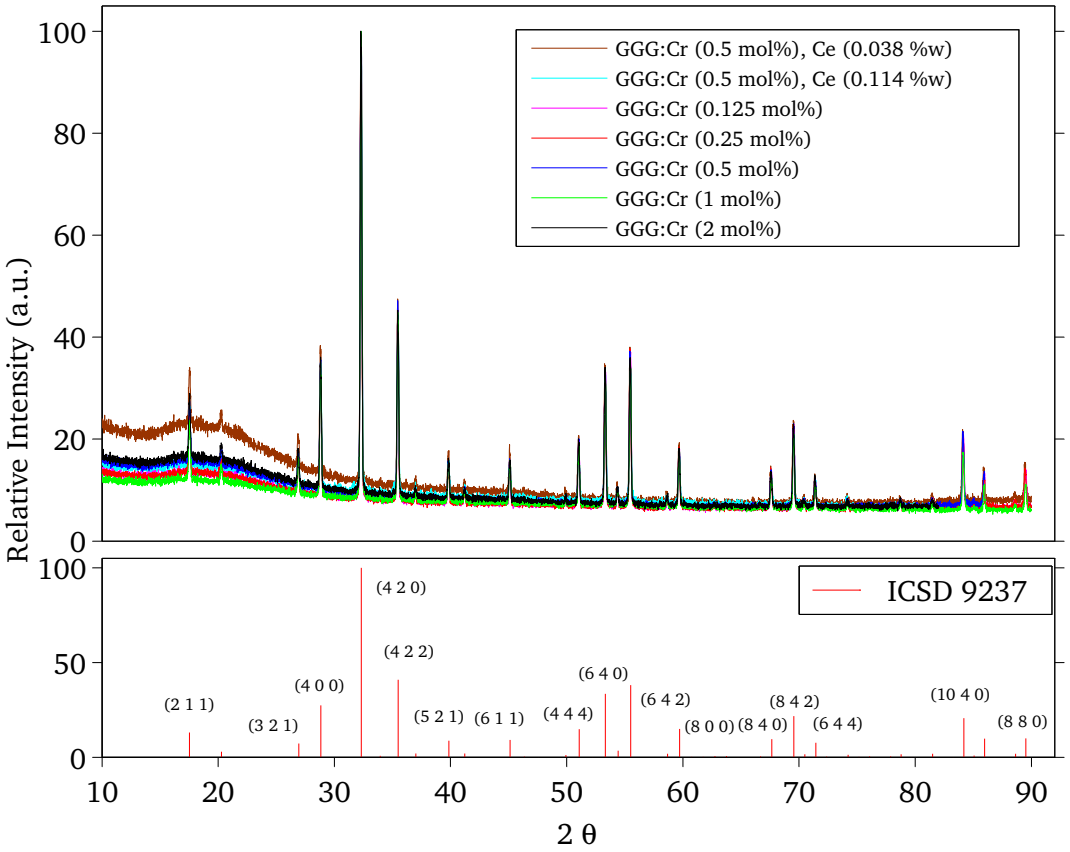

Figure 5.20: XRD patterns of the GGG:Cr^{3+} powder samples with different doping concentrations along with the GGG:Cr^{3+} samples co-doped with Ce.

5.4.2 Effect of doping concentration on the temperature-dependent luminescence properties

To study the effect of doping concentration on the temperature-dependent luminescence properties of GGG:Cr^{3+}, measurements of the lifetimes of powder samples with Cr concentrations of 0.125, 0.25, 0.5, 1, and 2 mol% were carried out in the range from 480 to 670 K. The results, obtained with the parameters $c_1 = 0.5$ and $c_2 = 3.5$ for the iterative fitting window algorithm, are plotted in Figure 5.21. At low doping concentrations there is not a clear effect of the Cr concentration on the luminescence lifetime. However, the luminescence lifetime decreases with the increase of the Cr concentration from 0.5 mol%, probably due to concentration quenching [7]. Although, the lifetimes are shifted when varying the doping concentration, the temperature sensitivities of the lifetimes are similar in this temperature range.

The normalized shot-to-shot standard deviations of the single-shot temperatures, calculated with Equation 5.1, for the samples with different doping concentrations are presented in Figure 5.22. The five GGG:Cr^{3+} samples provide standard deviations below 0.45% within the observed temperature range. Therefore, the selection of the doping concentration is not expected to affect the precision of the thermographic system to perform single-shot temperature measurements.

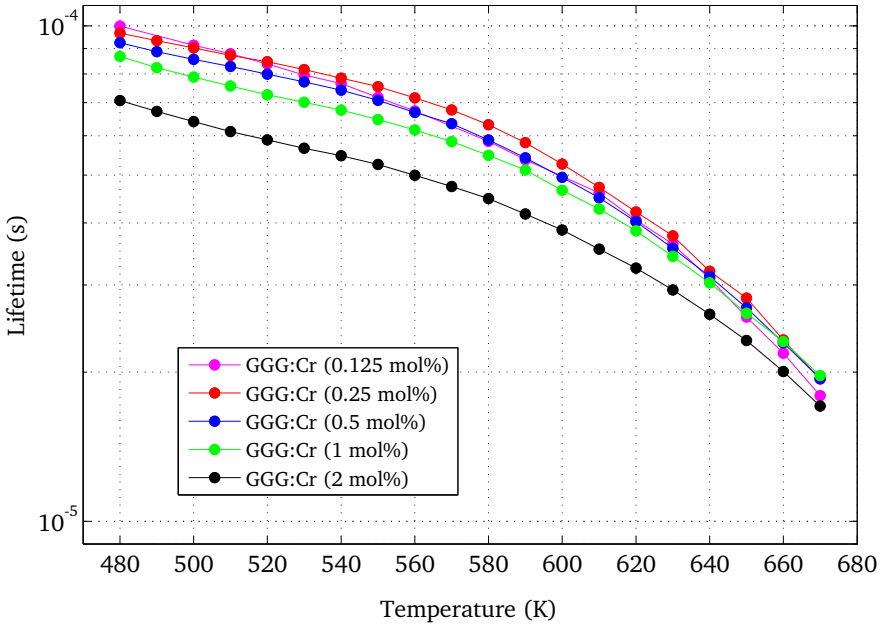

Figure 5.21: Temperature-lifetime characteristics of the GGG:Cr^{3+} powder samples with different doping concentrations.

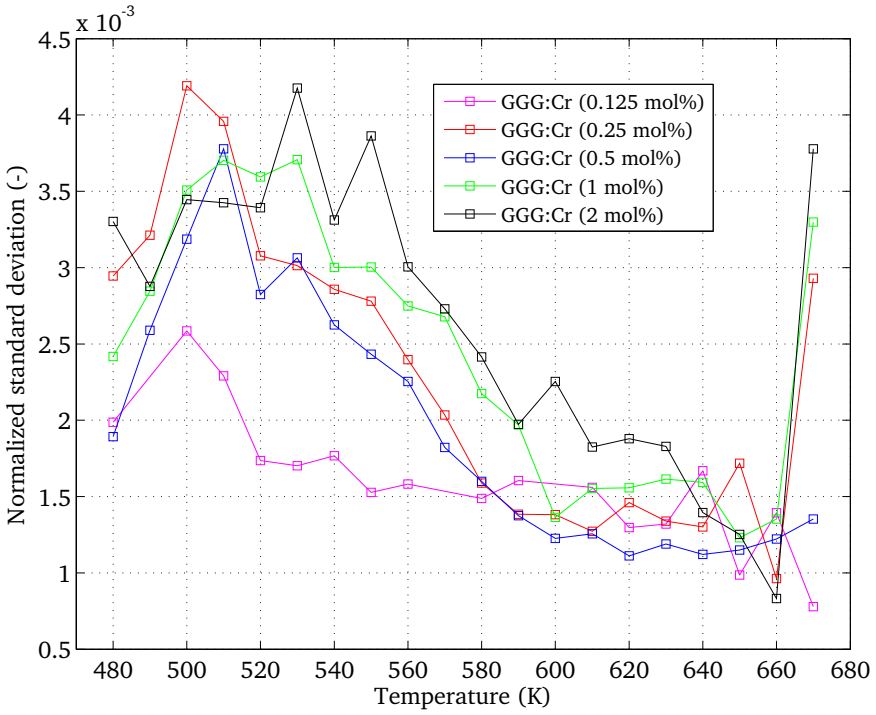

Figure 5.22: Normalized shot-to-shot standard deviations in terms of temperature for the GGG:Cr^{3+} powder samples with different doping concentrations.

5.4.3 Effect of co-doping with Ce on the temperature-dependent luminescence properties

The effect of co-doping with small amounts of Ce on the temperature-dependent luminescence properties of the GGG:Cr^{3+} was studied in the range from 480 to 670 K. Figure 5.23 presents the results of the luminescence lifetime of the GGG:Cr^{3+} sample with 0.5 mol% Cr content, along with the samples co-doped with 0.038 and 0.114 %w Ce. The parameters $c_1 = 0.5$ and $c_2 = 3.5$ were used for the iterative fitting window algorithm. As can be seen, the sample co-doped with 0.038 %w Ce has similar lifetime characteristics than the GGG:Cr^{3+} sample without Ce content. However, the increase of the Ce content up to 0.114 %w produces an irregular change in the lifetime values between 480 and 560 K, probably due to a major role of Ce transitions in the luminescences characteristics of the phosphor. To clarify this, the averaged normalized decays of the luminescence signals at 510 and 620 K are plotted in Figure 5.24. As can be observed, the luminescence decay at 510 K is highly multi-exponential, particularly until $\sim$100 μs. Therefore the fitting was carried out including this section of the decay, affecting the values of τ. Whereas, at 620 K, the highly multi-exponential part of the decay is shorter, affecting less the fitting. To overcome this, the parameters of the fitting algorithm were changed to $c_1 = 1.7$ and $c_2 = 3.9$, expecting to fit the lifetimes at sections where the decay shows fairly mono-exponential characteristics. As shown in Figure 5.23, with the change of the fitting parameters, a calibration curve with similar sensitivity as those of GGG:Cr^{3+} (0.5 mol%) and GGG:Cr^{3+} (0.5 mol%), Ce (0.038 %w) can be obtained.

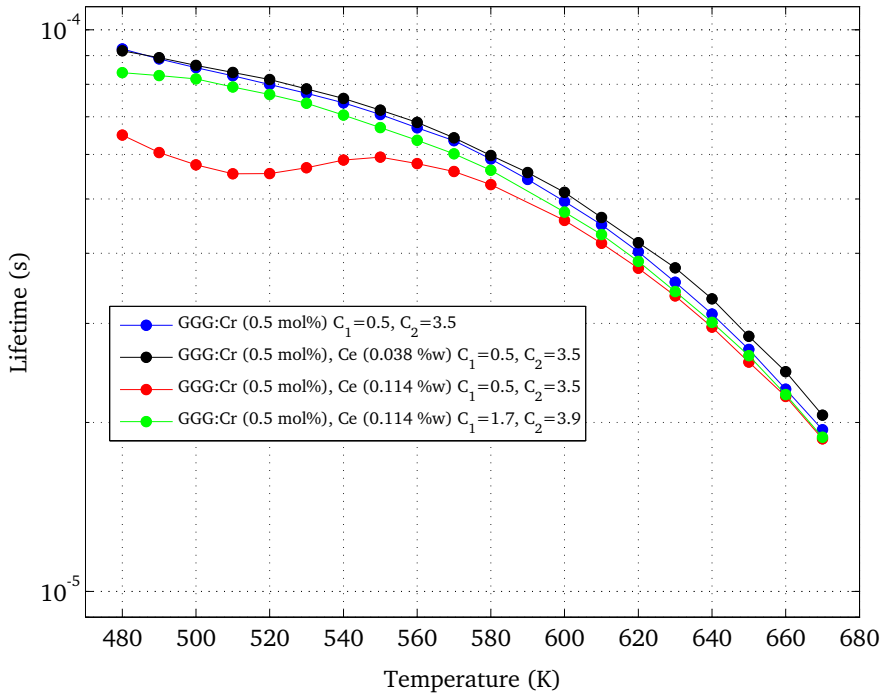

Figure 5.23: Temperature-lifetime characteristics of the GGG:Cr^{3+} powder samples co-doped with Ce.

The precision of the measurements decreases when co-doping with a high content of Ce. As can be seen in Figure 5.25, the normalized shot-to-shot standard deviation of the GGG:Cr^{3+} sample co-doped with 0.114 %w Ce is higher than 1%, particularly at temperatures between 480 and 540 K, while the values of the GGG:Cr^{3+} (0.5 mol%) and GGG:Cr^{3+} (0.5 mol%), Ce (0.038 %w) samples are lower than 0.5% in the whole range studied. Finally, as can be deduced from Figure 5.26, two improvements in the luminescence properties of GGG:Cr^{3+} by co-doping with small amounts of Ce could be obtained: (1) the decay of the luminescence signal is fairly mono-exponential, which is favorable for the fitting of lifetime values and (2) the luminescent afterglow is decreased in agreement with Greskovich *et al.* [78]. This

could be highly beneficial for example for high speed temperature measurements since the base lines of the decay waveforms would not strongly change during the sampling.

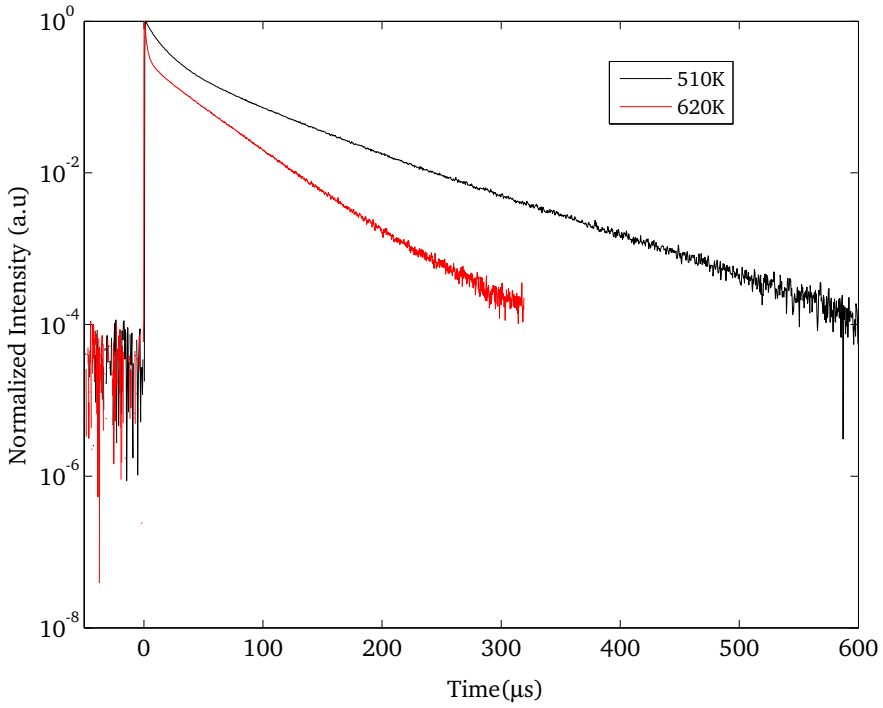

Figure 5.24: Normalized decays of the luminescence signals of the GGG:Cr^{3+} (0.5 mol%), Ce (0.114 %w) sample at 510 and 620 K.

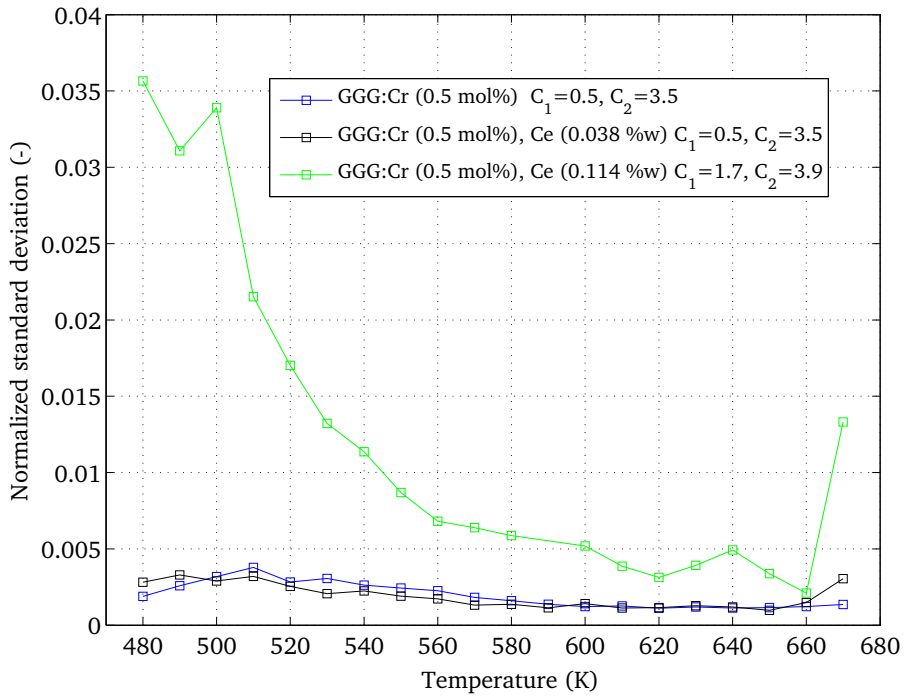

Figure 5.25: Normalized shot-to-shot standard deviations in terms of temperature for the GGG:Cr^{3+} powder samples co-doped with Ce.

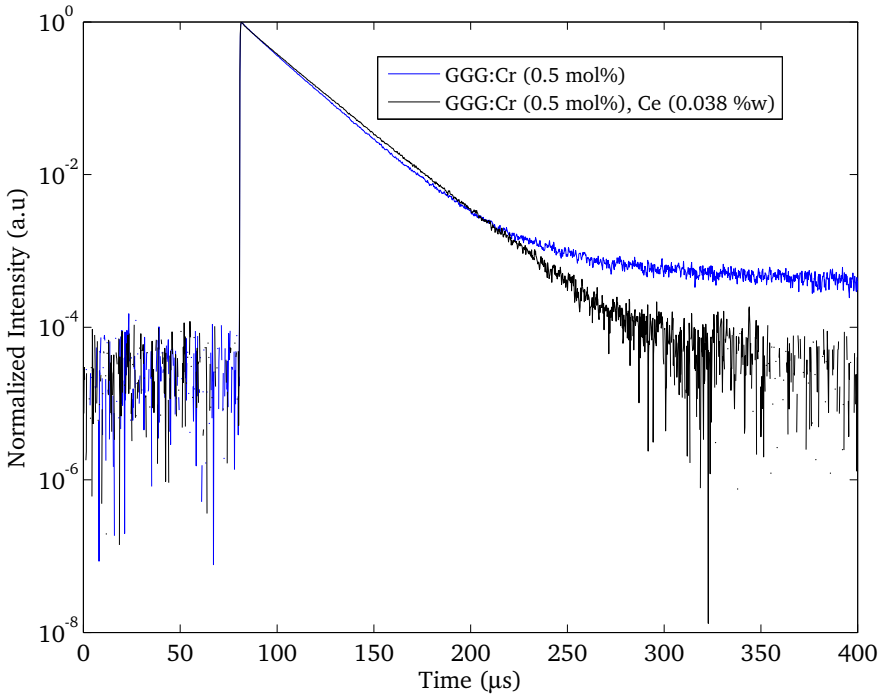

Figure 5.26: Normalized decays of the luminescence signals of the GGG:Cr^{3+} (0.5 mol%), and the GGG:Cr^{3+} (0.5 mol%), Ce (0.038 %w) samples at 670 K.

6 Concluding Remarks and Outlook

Stable thin films of praseodymium-doped calcium titanate, $CaTiO_3:Pr^{3+}$, and chromium-doped gadolinium gallium oxide, $Gd_3Ga_5O_{12}:Cr^{3+}$ have been successfully deposited on stainless steel substrates by radio frequency magnetron sputtering. The physical, chemical, and luminescence properties of the phosphor films have been evaluated for thermographic purposes. Experiments in $Gd_3Ga_5O_{12}:Cr^{3+}$ powders, varying the doping concentration and evaluating the effect of co-doping with cerium, have been included. From the results, their analysis and discussion, the following conclusions and outlook can be stated:

With appropriate handling, stable sputtering targets of $CaTiO_3:Pr^{3+}$ and $Gd_3Ga_5O_{12}:Cr^{3+}$ can be prepared by sol-gel combustion and solid-state reactions, respectively, combined with high temperature sintering. However, their thermal and mechanical strength limited the performance of the sputtering process and, therefore, decreased the deposition rate of the films, increasing significantly the time required for the deposition. It is recommended to sinter the targets at temperatures around 1800 K to enhance their properties, making them suitable for high-power sputtering deposition and reducing the deposition time.

The physical and chemical characterization of the films allowed determining that the annealing process is necessary to restore the crystal structure and the luminescence characteristics of phosphor films deposited by sputtering. Phosphors of complex crystal structures, such as $Gd_3Ga_5O_{12}:Cr^{3+}$, require annealing at high temperatures during several hours. This could represent a limitation for the applicability of sputtering to thermographic phosphors because some substrate materials could not resist annealing at high temperatures. In consequence, it is recommended to explore the use of advanced annealing processes such as laser annealing.

The functionality of the thin films of thermographic phosphors was evaluated at different temperatures by determining the luminescence characteristics under laser excitation. The $CaTiO_3:Pr^{3+}$ thin film showed a weak emission, resulting in low signal-to-noise ratios and poor temperature-dependent luminescence properties. Although the film exhibited fast luminescence decays, the low temperature sensitivity and poor precision could limit the use of $CaTiO_3:Pr^{3+}$ thin films for thermography applications.

In the case of the $Gd_3Ga_5O_{12}:Cr^{3+}$, the thin film exhibited a strong luminescence signal, fast luminescence decays, and appropriate temperature sensitivity in a relative wide range of temperatures (from 310 to 1000 K), with adequate precision of the temperature determination. However, when two-dimensional luminescence properties were evaluated, the film showed spatial inhomogeneities in the luminescence lifetime at room temperature, suggesting local differences of activator concentration in the film. Thin films of $Gd_3Ga_5O_{12}:Cr^{3+}$ proved to be suitable for point temperature measurements. Nevertheless, its application for spatially resolved temperature measurements would require further studies, for example, of the effects of the main parameters involved in sputtering deposition on the final functionality of the film. Moreover, multidimensional surface characterization of the thin films, that allow relating their physical and chemical properties with their spatial luminescence properties, is highly recommended.

Finally, the experiments in $Gd_3Ga_5O_{12}:Cr^{3+}$ powders samples revealed that variations in doping concentration of Cr^{3+} only change significantly the luminescence lifetime at concentrations above 1 mol%,

while sensitivity and precision of the temperature determination are maintained. Co-doping with small amounts of cerium reduces the afterglow and produces fairly mono-exponential luminescence decays. However, an excess of cerium affects significantly the luminescence properties of $Gd_3Ga_5O_{12}:Cr^{3+}$, resulting in highly multi-exponential decays and poor precision of the temperature determination.

Bibliography

[1] A. G. Evans, D. R. Mumm, J. W. Hutchinson, G. H. Meier, and F. S. Pettit. Mechanisms controlling the durability of thermal barrier coatings. *Progress in Materials Science*, 46(5):505–553, 2001.

[2] K. M. Kim, N. Yun, Y. H. Jeon, D. H. Lee, and H. H. Cho. Failure analysis in after shell section of gas turbine combustion liner under base-load operation. *Engineering Failure Analysis*, 17(4):848–856, 2010.

[3] P. R. N. Childs, J. R. Greenwood, and C. A. Long. Review of temperature measurement. *Review of Scientific Instruments*, 71(8):2959–2978, 2000.

[4] J. Brübach, M. Hage, J. Janicka, and A. Dreizler. Simultaneous phosphor and CARS thermometry at the wall-gas interface within a combustor. *Proceedings of the Combustion Institute*, 32(1):855–861, 2009.

[5] J. A. Stasiek and T. A. Kowalewski. Thermochromic liquid crystals in heat transfer research. *Proc. SPIE 4759, XIV Conference on Liquid Crystals: Chemistry, Physics, and Applications*, pages 374–383, 2002.

[6] T. Liu, B. T. Campbell, S. P. Burns, and J. P. Sullivan. Temperature- and pressure-sensitive luminescent paints in aerodynamics. *Applied Mechanics Reviews*, 50(4):227–246, 1997.

[7] A. Khalid and K. Kontis. Thermographic phosphors for high temperature measurements: Principles, current state of the art and recent applications. *Sensors*, 8(9):5673–5744, 2008.

[8] J. Brübach, J. Janicka, and A. Dreizler. An algorithm for the characterization of multi-exponential decay curves. *Optics and Lasers in Engineering*, 47(1):75–79, 2009.

[9] N. Fuhrmann, T. Kissel, A. Dreizler, and J. Brübach. $Gd_3Ga_5O_{12}$:Cr—a phosphor for two-dimensional thermometry in internal combustion engines. *Measurement Science and Technology*, 22(4):045301, 2011.

[10] J. Brübach, E. Van Veen, and A. Dreizler. Combined phosphor and CARS thermometry at the wall-gas interface of impinging flame and jet systems. *Experiments in Fluids*, 44(6):897–904, 2008.

[11] J. P. Feist, A. L. Heyes, and S. Seefelt. Thermographic phosphor thermometry for film cooling studies in gas turbine combustors. *Proceedings of the Institution of Mechanical Engineers, Part A: Journal of Power and Energy*, 217(2):193–200, 2003.

[12] A. Omrane, F. Ossler, M. Aldén, J. Svenson, and J. B. C. Pettersson. Surface temperature of decomposing construction materials studied by laser-induced phosphorescence. *Fire and Materials*, 29(1):39–51, 2005.

[13] S. W. Allison, M. R. Gates, D. L. Beshears, and G. T. Gillies. Phosphor thermometry at ORNL. *AIP Conference Proceedings*, 684(1):1033–1038, 2003.

[14] A. M. Murray and L. A. Melton. Fluorescence methods for determination of temperature in fuel sprays. *Applied Optics*, 24(17):2783–2787, 1985.

[15] A. Omrane, F. Ossler, and M. Aldén. Two-dimensional surface temperature measurements of burning materials. *Proceedings of the Combustion Institute*, 29(2):2653–2659, 2002.

[16] N. Fuhrmann, M. Schild, D. Bensing, S. Kaiser, C. Schulz, J. Brübach, and A. Dreizler. Two-dimensional cycle-resolved exhaust valve temperature measurements in an optically accessible internal combustion engine using thermographic phosphors. *Applied Physics B: Lasers and Optics*, 106:945–951, 2012.

[17] J. Ervin, C. Murawski, C. MacArthur, M. Chyu, and D. Bizzak. Temperature measurement of a curved surface using thermographic phosphors. *Experimental Thermal and Fluid Science*, 11(4):387–394, 1995.

[18] H. Aizawa, M. Sekiguchi, T. Katsumata, S. Komuro, and T. Morikawa. Fabrication of ruby phosphor sheet for the fluorescence thermometer application. *Review of Scientific Instruments*, 77(4):044902, 2006.

[19] S. S. Azim, C. Solaiyan, and G. Venkatachari. Development of coating for temperature sensing. *Progress in Organic Coatings*, 62(1):28 – 31, 2008.

[20] S. W. Allison, D. L. Beshears, T. Gadfort, T. Bencic, J. Eldridge, W. A. Hollerman, and P. Boudreaux. High temperature surface measurements using lifetime imaging of thermographic phosphors: bonding tests. *ICIASF Record, International Congress on Instrumentation in Aerospace Simulation Facilities*, pages 171–176, 2001.

[21] S. M. Goedeke, W. A. Hollerman, N. P. Bergeron, S. W. Allison, M. R. Cates, T. J. Bencic, C. R. Mercer, and J. I. Eldridge. *Study of Resbond®Ceramic binders used for high temperature non-contact thermometry*, pages 115–125. John Wiley & Sons, Inc., 2006.

[22] S. Alaruri, D. McFarland, A. Brewington, M. Thomas, and N. Sallee. Development of a fiber-optic probe for thermographic phosphor measurements in turbine engines. *Optics and Lasers in Engineering*, 22(1):17 – 31, 1995.

[23] I. P. McClean, A. J. Simons, C. B. Thomas, and J. E. Mutton. Comparison between thin film and bonded powder phosphors for thermographic sensing in gas turbine engines. *IEEE Trans Instrum Meas*, 49(1):129–131, 2000.

[24] R. M. Ranson, C. B. Thomas, and M. R. Craven. A thin film coating for phosphor thermography. *Measurement Science and Technology*, 9(12):1947, 1998.

[25] H. Seyfried, G. Sarner, A. Omrane, M. Richter, H. Schmidt, and M. Alden. Optical diagnostics for characterization of a full-size fighter-jet afterburner. *ASME Conference Proceedings*, 2005(46997):813–819, 2005.

[26] H. Seyfried, M. Richter, M. Aldén, and H. Schmidt. Laser-induced phosphorescence for surface thermometry in the afterburner of an aircraft engine. *AIAA Journal*, 45(12):2966–2971, 2007.

[27] J. Armfield, R. Graves, D. Beshears, M. Cates, T. V. Smith, and S. W. Allison. Phosphor thermometry for internal combustion engines. *SAE Technical Paper 971642*, 1997.

[28] W. Kern and K. K. Schuegraf. *1 - Deposition technologies and applications: introduction and overview*, pages 11–43. William Andrew Publishing, Norwich, NY, 2001.

[29] J. Brübach, C. Pflitsch, A. Dreizler, and B. Atakan. On surface temperature measurements with thermographic phosphors: a review. *Progress in Energy and Combustion Science*, 39:37–60, 2013.

[30] A. C. Pierre. *Introduction to sol–gel processing*. Kluver Academic Publishers, Boston, 1998.

[31] A. Nebatti, C. Pflitsch, C. Eckert, and B. Atakan. Sol–gel-deposition of thin TiO_2:Eu^{3+} thermographic phosphor films. *Progress in Organic Coatings*, 67(3):356 – 360, 2010.

[32] C. Pflitsch, R. A. Siddiqui, C. Eckert, and B. Atakan. Sol–gel deposition of chromium doped aluminium oxide films (ruby) for surface temperature sensor application. *Chemistry of Materials*, 20(8):2773–2778, 2008.

[33] C. Pflitsch, D. Viefhaus, and B. Atakan. CVD of thin ruby films on Si(100) and stainless steel for surface temperature sensor applications. *Chemical Vapor Deposition*, 13(8):420–426, 2007.

[34] C. Eckert, C. Pflitsch, and B. Atakan. Dy^{3+}:Al_2O_3 and (Dy^{3+}, Cr^{3+}): Al_2O_3 films for temperature sensor applications derived by thermal cvd and sol-gel techniques. *ECS Transactions*, 25(8):1293–1300, 2009.

[35] K. L. Choy, J. P. Fesit, A. L. Heyes, and B. Su. Eu-doped Y_2O_3 phosphor films produced by electrostatic-assisted chemical vapor deposition. *Journal of Materials Research*, 14:3111–3114, 1999.

[36] M. M. Gentleman, J. I. Eldridge, D. M. Zhu, K. S. Murphy, and D. R. Clarke. Non-contact sensing of TBC/BC interface temperature in a thermal gradient. *Surface and Coatings Technology*, 201(7):3937–3941, 2006.

[37] R. J. L. Steenbakker, R. G. Wellman, J. R. Nicholls, and J. P. Feist. Sensor TBCs: remote in-situ condition monitoring of EB-PVD coatings at elevated temperatures. *ASME Conference Proceedings*, 2008(43116):269–278, 2008.

[38] U. Gibson and M. Chernuschenko. Ruby films as surface temperature and pressure sensors. *Opt. Express*, 4(11):443–448, 1999.

[39] X. Chen, Z. Mutasim, J. Price, J. P. Feist, A. L. Heyes, and S. Seefeldt. Industrial sensor TBCs: studies on temperature detection and durability. *International Journal of Applied Ceramic Technology*, 2(5):414–421, 2005.

[40] S. Rossnagel and K. Seshan. *8 - Sputtering and sputter deposition*, pages 319–348. William Andrew Publishing, Norwich, NY, 2001.

[41] T. Minami, T. Nakatani, T. Miyata, and T. Shirai. (Y_2O_3–GeO_2) phosphor thin-film electroluminescent emitting layers prepared by magnetron sputtering. *Surface and Coatings Technology*, 146–147(0):508–512, 2001.

[42] S. M. Chung, S. H. Han, and Y. J. Kim. Characterization of compositional variation and luminescence of $ZnGa_2O_4$:Mn thin film phosphor. *Materials Letters*, 59(7):786–789, 2005.

[43] T. K. Tran, W. Park, J. W. Tomm, B. K. Wagner, S. M. Jacobsen, C. J. Summers, P. N. Yocom, and S. K. McClelland. Photoluminescence properties of $ZnGa_2O_4$:Mn powder phosphors. *Journal of Applied Physics*, 78(9):5691–5695, 1995.

[44] H. Song and Y. J. Kim. Characterization of luminescent properties of ZnO:Er thin films prepared by rf magnetron sputtering. *Journal of the European Ceramic Society*, 27(13–15):3745–3748, 2007.

[45] T. Miyata, J. Ishino, K. Sahara, and T. Minami. Color control of emissions from rare earth-co-doped La_2O_3:Bi phosphor thin films prepared by magnetron sputtering. *Thin Solid Films*, 519(22):8095–8099, 2011.

[46] J. P. Chu, I. J. Hsieh, J. T. Chen, and M. S. Feng. Growth of $MgWO_4$ phosphor by rf magnetron sputtering. *Materials Chemistry and Physics*, 53(2):172–178, 1998.

[47] J. Kim and K. Yoon. Influence of post-deposition annealing on the microstructure and properties of Ga_2O_3:Mn thin films deposited by rf planar magnetron sputtering. *Journal of Materials Science: Materials in Electronics*, 20(9):879–884, 2009.

[48] D. Kim, S. Choi, C. Park, and B. O. Luminescence characteristics of ZnS:Cu thin film electroluminescent devices fabricated by sputtering. *Journal of Materials Science: Materials in Electronics*, 9(1):31–34, 1998.

[49] C. Chartier, C. Barthou, P. Benalloul, S. Chenot, and J. M. Frigerio. Structural and luminescent properties of green emitting $SrGa_2S_4$:Eu thin films prepared by rf-sputtering. *Journal of Crystal Growth*, 256(3–4):305–316, 2003.

[50] E. J. Bosze, G. A. Hirata, and J. McKittrick. An analysis of Y_2O_3:Eu^{3+} thin films for thermographic phosphor applications. *Journal of Luminescence*, 131(1):41–48, 2011.

[51] L. Sarakha, T. Bégou, A. Goullet, J. Cellier, A. Bousquet, E. Tomasella, T. Sauvage, P. Boutinaud, and R. Mahiou. Influence of synthesis conditions on optical and electrical properties of $CaTiO_3$:Pr^{3+} thin films deposited by radiofrequency sputtering for electroluminescent device. *Surface and Coatings Technology*, 205, Supplement 2(0):S250–S253, 2011.

[52] S. M. Chung, S. H. Han, K. H. Song, E. S. Kim, and Y. J. Kim. Luminescent properties of $CaTiO_3$:Pr thin-film phosphor deposited on ZnO/ITO/glass substrate. *Journal of Luminescence*, 114(3–4):227–233, 9 2005.

[53] L. Sarakha, A. Bousquet, E. Tomasella, P. Boutinaud, and R. Mahiou. Investigation of $CaTiO_3$:Pr^{3+} thin films deposited by radiofrequency reactive magnetron sputtering for electroluminescence application. *Materials Science and Engineering Conference Series*, 12(1):012008, 2010.

[54] E. Pinel, P. Boutinaud, and R. Mahiou. What makes the luminescence of Pr^{3+} different in $CaTiO_3$ and $CaZrO_3$? *Journal of Alloys and Compounds*, 380(1–2):225–229, 2004.

[55] S. Fukaya, K. Adachi, M. Obara, and H. Kumagai. The growth of Cr^{4+}:YAG and Cr^{4+}:GGG thin films by pulsed laser deposition. *Optics Communications*, 187(4–6):373–377, 2001.

[56] M. S. B. Darby, T. C. May-Smith, R. W. Eason, T. Donnelly, J. G. Lunney, and K. D. Rogers. A comparative study of gadolinium gallium garnet growth by femtosecond and nanosecond pulsed laser deposition. *Applied Surface Science*, 254(11):3364–3369, 2008.

[57] X. Xu, Z. Xu, Y. Hou, X. Wang, X. Chen, and X. Xu. A novel blue thin film electroluminescent phosphor $Gd_3Ga_5O_{12}$:Ag. *Chinese Physics Letters*, 16(5):387, 1999.

[58] X. Xu, Z. Xu, Y. Hou, Y. Wang, and X. Xu. Influence of Ag concentration and post-deposition annealing on $Gd_3Ga_5O_{12}$:Ag thin film electroluminescence. *Displays*, 22(3):97–100, 2001.

[59] C. Gheorghies, P. Boutinaud, M. Loic, and V.O. Atanasiu. Results on nanosized $CaTiO_3$:Pr^{3+} phosphor. *Journal of optoelectronics and advanced materials*, 11(5):583–589, 2009.

[60] P. Boutinaud, E. Pinel, M. Dubois, A. P. Vink, and R. Mahiou. UV-to-red relaxation pathways in $CaTiO_3$:Pr^{3+}. *Journal of Luminescence*, 111(1–2):69–80, 2005.

[61] R. Martín-Rodríguez. *Synthesis, structural characterization and spectroscopic study of nanocrystalline and microcrystralline materials*. PhD thesis, Universidad de Cantabria, 2010.

[62] U. Hömmerich and K. L. Bray. High-pressure laser spectroscopy of Cr^{3+}:$Gd_3Sc_2Ga_5O_{12}$ and Cr^{3+}:$Gd_3Ga_5O_{12}$. *Physical Review B*, 51(18):12133–12141, 1995.

[63] B. Chapman. *Glow discharge processes: sputtering and plasma etching*. John Wiley & Sons, Inc., New York, 1980.

[64] STOE and Cie GmbH. STOE Version 1.1, 2002. `http://www.stoe.com`.

[65] Omicron NanoTechnology GmbH. Multiprobe surface science systems user's guide. Project 094603, September, 2010.

[66] J. F. Moulder, W. F. Stickle, P. E. Sobol, and K. D. Bomben. *Handbook of X-ray photoelectron spectroscopy*. Physical Electronics, Inc., Minnesota, 1995.

[67] N. Fuhrmann, J. Brübach, and A. Dreizler. Phosphor thermometry: a comparison of the luminescence lifetime and the intensity ratio approach. *Proceedings of the Combustion Institute*, 2012. http://dx.doi.org/10.1016/j.proci.2012.06.084.

[68] M. A. Everest and D. B. Atkinson. Discrete sums for the rapid determination of exponential decay constants. *Review of Scientific Instruments*, 79(2):023108–9, 2008.

[69] H. F. Kay and P. C. Bailey. Structure and properties of $CaTiO_3$. *Acta Crystallographica*, 10(3):219–226, 1957.

[70] E.L. Dukhovskaya, Y.G. Saksonov, and A.G Titova. *Neorganicheskie Materialy*, 9:809–813, 1973.

[71] R. Martín-Rodríguez, R. Valiente, F. Rodríguez, and M. Bettinelli. Temperature and pressure dependence of the optical properties of Cr^{3+}-doped $Gd_3Ga_5O_{12}$ nanoparticles. *Nanotechnology*, 22(26):265707, 2011.

[72] W. H. Chao, R. J. Wu, and T. B. Wu. Structural and luminescent properties of YAG:Ce thin film phosphor. *Journal of Alloys and Compounds*, 506(1):98–102, 2010.

[73] G. J. Fischer, Z. Wang, and S. Karato. Elasticity of $CaTiO_3$, $SrTiO_3$ and $BaTiO_3$ perovskites up to 3.0 GPa: the effect of crystallographic structure. *Physics and Chemistry of Minerals*, 20(2):97–103, 1993.

[74] Z. Wang, S. Karato, and K. Fujino. High temperature creep of single crystal gadolinium gallium garnet. *Physics and Chemistry of Minerals*, 23(2):73–80, 1996.

[75] Casa Software Ltd. Manual of basic quantification of XPS spectra, 2011. http://www.casaxps.com/help_manual/manual_updates/xps_spectra.pdf.

[76] Casa Software Ltd. CasaXPS Version 2.3.16, 1999-2011. http://www.casaxps.com.

[77] J. Brübach, T. Kissel, M. Frotscher, M. Euler, B. Albert, and A. Dreizler. A survey of phosphors novel for thermography. *Journal of Luminescence*, 131(4):559–564, 2011.

[78] C. Greskovich and S. Duclos. Ceramic scintillators. *Annual Review of Materials Science*, 27(1):69–88, 1997.